The Graduate University for Advanced Studies (SOKENDAI)

Doctoral Thesis

Research of Copper Thermal Spray Coating for Mitigating Electron Cloud Effect

School: High Energy Accelerator Science

Department: Accelerator Science

Name: YAO, MU-LEE

Advisor: SHIBATA, Kyo

15th March 2023

Abstract

The electron cloud effect (ECE) has posed serious challenges in recent high-intensity proton and positron rings. One possible solution is to prepare a surface with a low secondary electron yield (SEY) on the inner wall of the beam pipes. In this study, we used a commercial method called “thermal spraying,” (by which copper powder is melted and sprayed onto an aluminum substrate) to create a rough surface and investigated—for the first time in the literature—its suitability for producing a low SEY surface. After an electron exposure of ≈ 1 $\times 10^{-1}$ C/mm^2 at an energy of 350 eV, the lowest δ_{max} (the maximum SEY within the scanning range) of the copper thermal spray (T.S.) coating reached ~0.7.

The E_{max} (i.e., the incident electron energy corresponding to δ_{max}) of the T.S. coating was found to be inversely related to the surface temperature during spraying. The roughness parameters and surface composition were measured, to clarify the key factors affecting SEY. In addition, to verify its applicability in accelerators, we measured the outgassing rate, adhesive strength, impedance, and dust generation rate of the T.S coating, to serve as a reference for future studies.

Finally, an aluminum beam pipe with a T.S. coating was produced and installed in the positron ring of SuperKEKB, to measure the electron density around the beam. The measured electron densities were compared against those obtained from other beam pipes with different inner surfaces. Finally, we investigated the coatings via simulations.

The results show that the outgassing rate and adhesive strength of the T.S. coating were acceptable. However, the levels of dust and impedance were considerable. The measured electron densities of the T.S.-coated beam pipe were comparable with those of the TiN-coated beam pipe, even when an uncoated aluminum screen was used. Thus, the T.S. coating can be considered a candidate technology for reducing ECE, though room for improvement remains. This study provides new and useful information for researchers interested in developing low-SEY coatings for beam pipes.

SOKENDAI

Acknowledgement

First, I would like to acknowledge the support given by KEK and SOKENDAI, as well as the time and guidance given to me by all members of the SuperKEKB vacuum group.

My advisor, Dr. Kyo Shibata, was very patient with teaching and often let me take charge of the research direction. He visited the site with me during several important sample-production and measurement steps, to understand the process in detail. This not only expanded my knowledge but also cultivated my independent research abilities.

Dr. Yusuke Suetsugu advised me for my Master's project; however, he also remained deeply involved in my doctoral research. His rich research experience provided me with a unique method for interpreting the data and helped solve many key issues. He also helped me a lot with the electron cloud simulations.

My subadvisors Dr. Takuya Ishibashi and Mr. Shinji Terui worked in the same office as me. Hence, when I had any questions, they offered me initial guidance or directed me to experts across various fields.

Mr. Hiromi Hisamatsu provided me the important apparatus required for SEY measurement and also taught me numerous experimental skills. Mr. Mitsuru Shirai helped me produce several experimental items and performed the baking and installation steps for the thermal-spray-coated beam pipe. Dr. Ken-ichi Kanazawa also gave me useful suggestions regarding my research and presentation slides, to make my research more complete.

I am also grateful to the teachers from other groups in KEK. Dr. Tetsuo Abe taught me how to measure the Q value, Dr. Ryuichi Ueki taught me how to measure the magnetic field in the beam pipe, and Dr. Michinaka Sugano taught me how to use the muffle furnace.

Regarding the production of thermal spray coatings, I would like to thank Mr. Toshiro Nishidono and Mr. Hiroyuki Chiba from Komiyama Electron Corp. for their efforts. Besides, I would like to thank Editage (www.editage.com) for English language editing.

SOKENDAI

As an international student, I must thank my friends for their company over the past five years. Without these happy memories, my study abroad experience would have been nothing but research, which would have been too professional and isolating.

I must thank my parents for providing my study abroad living expenses, so that I could concentrate on my research without any financial worries. I am especially grateful that they came to Japan to help take care of my young daughter during the busiest part of my thesis preparation. This thesis would not have been completed without their help.

Lastly, I want to express my love to my wife Wang, Wei-Chien and daughter Yao, Syu-Li. The love that circulates between us is the meaning of life itself and also provides infinite motivation for life, allowing us to face all difficulties with a peaceful heart.

To God be the Glory

Yao, Mu-Lee

Contents

SOKENDAI

SOKENDAI

SOKENDAI

List of Tables

SOKENDAI

List of Figures

SOKENDAI

SOKENDAI

SOKENDAI

SOKENDAI

Chapter 1

Introduction

1.1 Background and Motivation

1.1.1 SuperKEKB

SuperKEKB is an electron–positron collider with asymmetric energy capabilities; it is an upgrade of the preceding collider, KEKB B-factory. It is affiliated to the High-energy Accelerator Research Organization (KEK), located in Tsukuba City, Japan. Its main purpose is to test new theories beyond the standard model in the B-meson regime. To obtain sufficient measurement accuracy, numerous collisions are required; these produce the high luminosity needed to increase the effective data count. Many B mesons are produced during collisions; hence, SuperKEKB is also called the B-factory [1]. The SuperKEKB consists of several components: an injector, a damping ring for positrons, a main ring (MR), and a Belle II particle detector (as shown in Fig. 1-1). The MR consists of two rings, each with a circumference of ~3016 m. The high-energy ring (HER) circulates electrons with an energy of 7 GeV, and the low-energy ring (LER) circulates positrons with an energy of 4 GeV. Each ring has four arc sections of ~550 m and four straight sections of ~200 m. The straight sections contain a beam injection/abort region, wiggler regions, radio-frequency (RF) accelerating cavity regions, and a beam collision region. The design current is 2.6 A for HER and 3.6 A for LER, with a maximum bunch number of 2500 and a bunch spacing of two RF buckets (one RF bucket corresponds to ~2 ns). The design luminosity is 8×10^{35} cm^{-2} s^{-1}, ~40 times that of KEKB. Other design parameters can be found in Ref. [1].

SOKENDAI

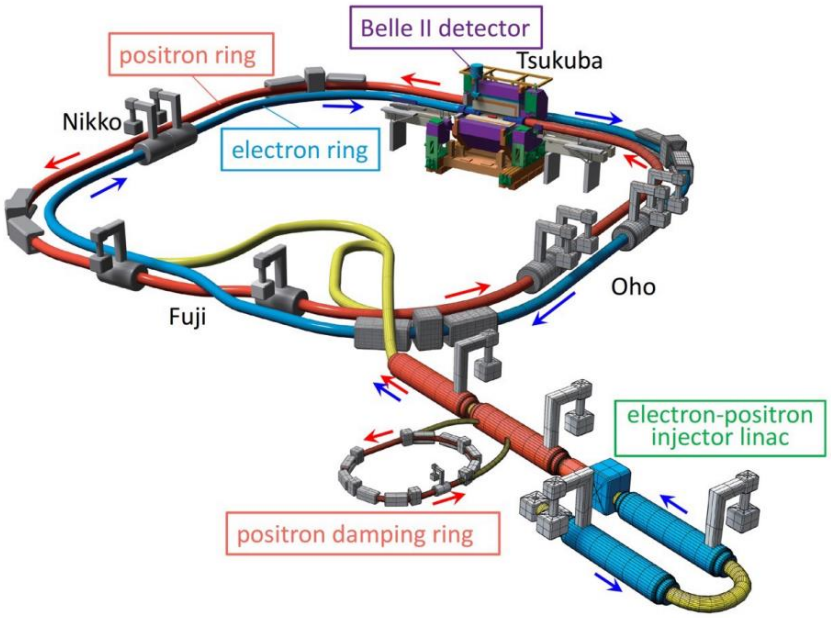

Figure 1-1: Layout of the SuperKEKB [1]

1.1.2 Electron Cloud Effect

The electron cloud (EC) refers to electrons that are attracted to and surround the positively charged beam (e.g., proton, positron, or ions). Its generation mechanism is shown in Fig. 1-2. The initial electrons that serve as seeds are obtained from many sources, including residual gas ionization, desorption from beam losses on the wall, and photo-electrons from synchrotron radiation (SR) [2]. The dominant source depends upon the beam type and parameters and vacuum level as well as the design, roughness, and cleanness of the inner surface of the beam pipe, amongst other factors [2]. In the SuperKEKB, the photo-electrons dominate most of the ring. As these “seeds” approach the positively charged beam, they are accelerated and strike the inner surface of the beam pipe. This can generate secondary electrons, depending on the impact energy and the secondary electron yield (SEY or δ) of the surface. An SEY value larger than 1 can result in a surge in the number of electrons (also known as multi-pacting) and the formation of an EC around the beam. EC accumulation halts at a density roughly equivalent to the neutralization density, where the attractive force from the beam is on average balanced by the space charge repulsion of the EC. The EC increases the pressure via electron bombardment of the surrounding surfaces (which accelerates EC generation), bunch size blow-up (which reduces luminosity), thermal loads in cryogenic vacuum systems (which cause stable phase shifts of the bunch in the RF bucket), and beam losses (which produce beam instabilities). These effects are grouped together under the electron cloud effect (ECE), which represents a

serious problem in recent high-intensity proton and positron rings [3, 4], including the SuperKEKB LER [5].

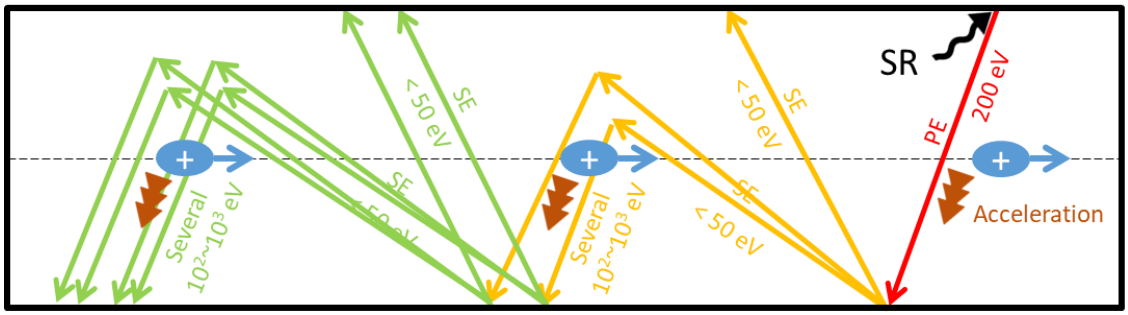

Figure 1-2: Mechanism of EC generation

Table 1-1: Summary of the main observations of ECEs in particle accelerators [2]

Year	Location	Observations
1965	Novosibirsk, Argonne ZGS, BNL AGS	Transverse instabilities
1970s	CERN ISR, Bevatron	Transverse instabilities, vacuum degradation
1988	Los Alamos PSR	Transverse instabilities
1989	KEK PF	Multi-bunch instability for positron bunch trains
1999	CERN SPS and PS, KEKB and PEP-II	Pressure increase, transverse instabilities, effects upon instrumentation, tune shifts along bunch train, emittance degradation
2002	RHIC	Pressure increase, tune shift, transverse instabilities at transition
2003–2009	Tevatron, SNS, DaΦne, ANKA, PETRA III, J-PARC main ring	Vacuum degradation, transverse instabilities, transverse blow-up, heat load on cryogenic devices
2008–present	Cesr-TA	Program to study electron cloud issues conducted
2010–present	LHC	Vacuum degradation, transverse instabilities, beam degradation, heat loads in cryogenic devices
2014	FERMILAB recycler	Transverse instabilities
2016–present	SuperKEKB	Dynamic pressure increase, beam degradation

SOKENDAI

Table 1-1 shows the main observations of ECEs in particle accelerators around the world. Simulations suggest that the threshold electron density $n_{e_{th}}$ at which blow-up of the beam size occurs is ~3×10^{11} m^{-3} in case of SuperKEKB LER [5].

1.1.3 Countermeasures in SuperKEKB

Various countermeasures have been developed. These (and the accelerators that use them) are listed in Figure 1-3 [5, 6-9]. Here, we take SuperKEKB as an example to explain the principles of the countermeasures.

1.1.3.1 Beam pipe with antechamber

One source of ECs is the photo-electrons generated by SR. The antechamber is a flank space extending horizontally from either side of the chamber. The structure of the antechamber in the arc section is shown in Fig. 1-4(a); it includes water-cooling channels and spaces for non-evaporable getter strips (NEGSs). SR is emitted along the tangential direction of the beam orbit; hence, this radiation hits the inner surface of the outside antechamber. Because this inner surface is far from the beam channel, and the electric field of the beam is small, the emitted photo-electrons are almost unable to escape from the antechamber region [10]. As a result, the number of photo-electrons in the beam channel is considerably reduced. In addition, the surfaces exposed to SR can be roughened by glass bead blasting to prevent scattered SR entering the beam channel [10].

For arc sections, the SR only hits the outside of the ring; hence, the antechamber located on the inside of the ring can be effectively used as a pump channel. The NEGSs are isolated from the main beam channel by a screen containing multiple round holes; this can mitigate the influence of the electromagnetic field induced by the beam, whilst also helping to maintain the pumping speed [10].

SOKENDAI

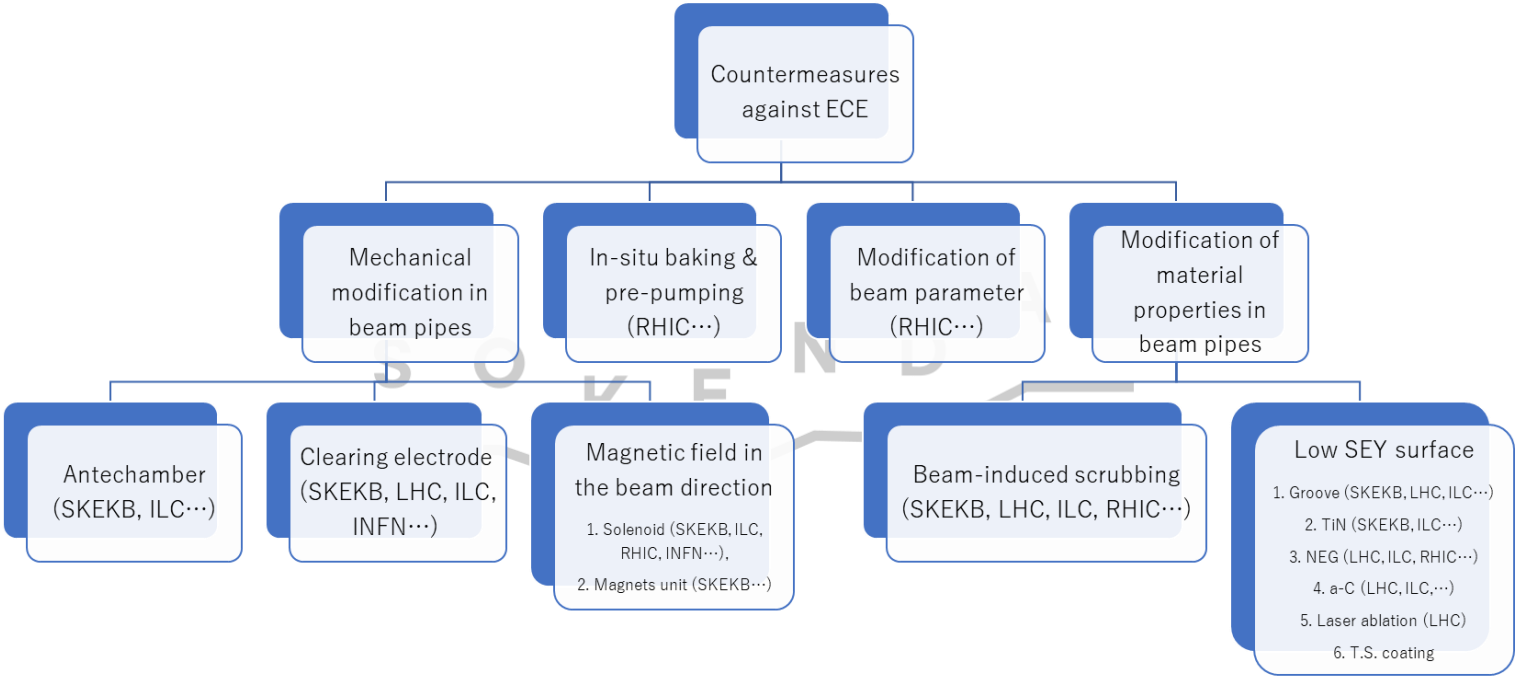

Figure 1-3: Map of the existing countermeasures used to eliminate ECEs in accelerators

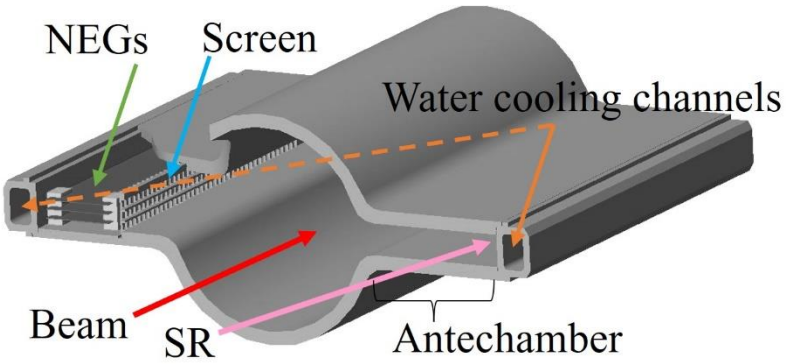

Figure 1-4: Antechamber in the SuperKEKB [5]

1.1.3.2 Clearing electrodes

The clearing electrode is thin and attached to the inner wall of the beam pipe; it is positively biased, to provide an electrostatic field for electron absorption [11]. Its efficacy at reducing the electron density exceeds that of other methods. However, relatively large beam impedances present a problem. A thin electrode was developed in KEK and installed at the wiggler sections [5], as shown in Fig. 1-5.

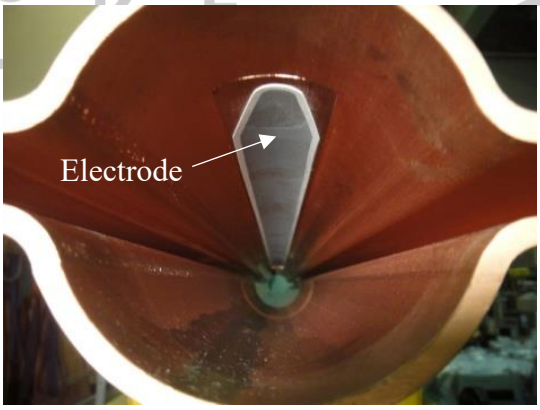

Figure 1-5: Clearing electrode in the SuperKEKB

1.1.3.3 Magnetic field in the beam direction

Moving electrons are affected by the magnetic field and rotate around the magnetic field line (i.e., cycloid motions). If a magnetic field is applied in the beam direction (B_z), the emitted electrons near the inner surface of the beam pipe (both photo-electrons and secondary electrons) will return to the surface. Thus, the "effective" photo-electron yield (the number of photo-electrons produced per incident photon) or SEY is considerably reduced. In principle, B_z has little effect on the beam. B_z can be applied via solenoid

winding around—or by a permanent magnet unit placed upon—the beam pipe [4, 12-16]. One problem with this method is that the magnetic field can only be applied to drift spaces in the ring, where no electromagnets are located. Figure 1-6 shows the two types of magnet unit and solenoid winding used to apply B_z. Alternating the direction of B_z can reduce the impact of the magnetic field upon the beam.

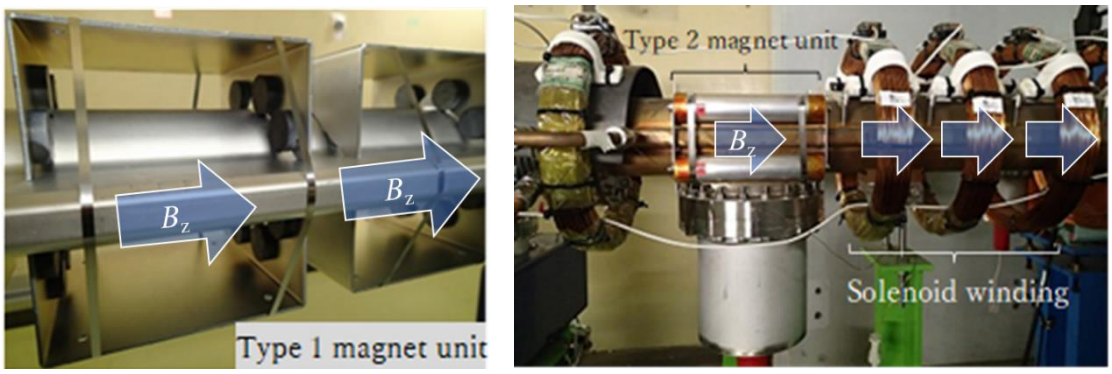

(a) (b)

Figure 1-6: Solenoid winding and magnet units used to produce a magnetic field in the beam direction (B_z) in the SuperKEKB [5]

SOKENDAI

1.1.3.4 Beam-induced scrubbing

Spontaneous decreases in SEY have been observed during accelerator operations [17]. "Scrubbing" (or conditioning) refers to continuous operation with the beam at its maximum possible intensity and duty cycle. During scrubbing, the residual gas adsorbed on the inner wall is bombarded with massive electrons and then extracted by the vacuum system [18-21]. As a result, the outgassing rate of the inner wall is reduced, and the overall pressure becomes lower. Other methods of reducing pressure (e.g., in-situ baking and pre pumping) in the cold section have been applied in the heavy-ion and proton rings of the Relativistic Heavy Ion Collider [8]. Meanwhile, the carbon molecules on the inner wall are converted into an inert graphite layer, which exhibits a low SEY [21]. Beam-induced scrubbing is not strictly an active countermeasure but rather the acceleration of a natural phenomenon beneficial to accelerators.

1.1.3.5 Surfaces with low SEYs

The SEY is an important factor in EC generation. Compared to other countermeasures, a low SEY surface can (in principle) be applied anywhere, including the beam pipe in the electromagnet. Therefore, it offers considerable potential to further enhance the accelerator performance.

Methods of reducing the SEY can be roughly classified into two categories: those based on material properties and those based on roughness. Various materials with low SEYs have been investigated so far, including titanium nitride (TiN) [22], graphite [23], diamond-like carbon [24], and non-evaporable getter (NEG) materials [25]. In SuperKEKB, TiN has been applied to more than 90% of the ring [5].

On the other hand, the SEY can be reduced by increasing the surface roughness. For example, Fig. 1-7 shows the triangular grooved surface produced by extrusion in SuperKEKB. Figure 1-8 presents a schematic of the grooved surface mechanism used to reduce SEY. When electrons are normally incident on a grooved surface, the angle of incidence is not exactly zero, as shown in Fig. 1-8. In theory, increasing the angle of incidence for the primary electrons will increase the SEY because the penetration depth becomes shallower and the secondary electrons generated within the material are more likely to escape from the surface. However, the grooved structure gives these secondary electrons a high probability of hitting the inner wall again within the structure. In an impact event, most of the secondary electrons have energies of less than 50 eV, and their corresponding SEY is low; thus, they have a high probability of being adsorbed, which reduces the net SEY.

SOKENDAI

In SuperKEKB, the beam pipes with triangular grooved surfaces are combined with a TiN coating in the bending magnet section (where electrons mostly impact the upper and lower sides of the beam pipe); thus, the grooved surface is only applied to the upper and lower sides. To reduce impedance, the groove is oriented in the same direction as the beam [26].

Fig. 1-7: Al-alloy groove surface without coating in the SuperKEKB

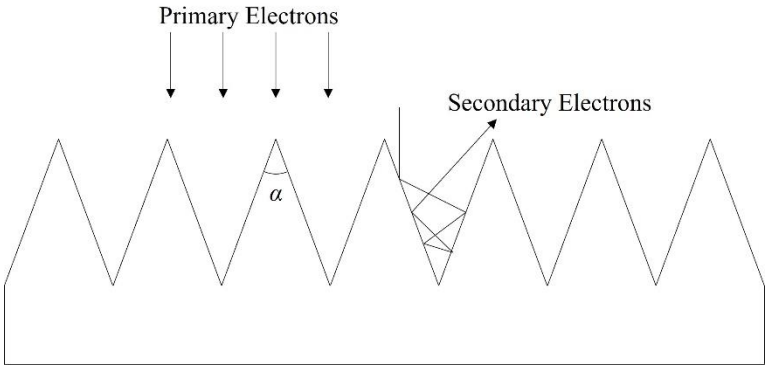

Figure 1-8: Schematic of the mechanism of the grooved surface reducing SEY

In addition to a rough surface featuring relatively large protrusions (e.g., grooved surfaces), rough surfaces (on the level of micrometers) are also a viable option; their mechanism of SEY suppression is generally the same as that of the grooved surface (e.g., chemical reaction [21, 27] or laser ablation surface engineering (LASE) [28-29]). The thermal spray coating used in this study represents one of these approaches.

1.1.3.6 Modification of beam parameter

Adjusting the beam parameters represents another option for reducing the electron density without affecting the luminosity. Typically, this means lowering the bunch current or increasing the interval between bunches. In the Relativistic Heavy-Ion Collider, optimized bunch patterns and longer bunches have successfully reduced the electron density during operations [8].

To summarize, antechambers can effectively reduce the number of photoelectrons entering the beam channel. Clearing electrodes are quite effective but difficult to apply in bent beam pipes. In addition, the clearing electrode requires a power source, which is another disadvantage. The solenoid winding and permanent magnet unit are effective but can be applied only to drift spaces in the ring, where no electromagnets are located. Scrubbing runs are beneficial for reducing the ECE. However, the surface conditioning is believed to be partially reset each time the vacuum sector is vented to air (in particular, when new components are installed). Therefore, an unproductive and expensive beam conditioning period is required after each intervention. This implies a reduction in the integrated luminosity delivered to the high-energy physics program.

Low SEY surfaces are the most widely applicable countermeasures; however, in reality, every surface has its own limitations. The groove surface is more effective if a

perpendicular magnetic field is present; hence, it was adopted in the bending magnets. However, this risks increasing the impedance at the junction with the normal beam pipe. The advantage of NEGs is their additional pumping function; however, they must be heated to 180 ℃ for 24 h to be activated. Therefore, they may suffer from heating temperature limitations in certain sections. The most famous coating, TiN, has been applied in many accelerators around the world; it works well under the effects of *in-situ* electron and photon conditioning. Amorphous carbon (a-C) could offer low SEYs without baking; however, the SEY under this method has only been reduced to near 1. At present, the LASE copper surface seems to offer the best overall performance: it produces a SEY lower than 1 without baking and has little effect on impedance. Unfortunately, the required technological threshold is high.

1.2 Purpose of this Study

As described above, the suppression of ECE represents a key issue for the SuperKEKB LER, and various countermeasures have been applied. According to current estimations, after applying these countermeasures, the electron density in the LER should theoretically be suppressed below the threshold at the designed beam current. Indeed, no clear evidence of ECEs has been observed thus far. However, the beam currents remain much lower than their designed values. Investigations of a surface with an even lower SEY are, therefore, still important, considering the proposed beam current increases. One promising method is to construct a rough surface to suppress the SEY and thereby suppress the ECE. Here, adopting these considerations, we focus on the thermal spray method.

Thermal spraying is a popular coating processes in which melted or heated materials are sprayed onto a surface. The thermal spray powders are heated by electrical (plasma or arc) or chemical (combustion flame) methods. Thermal spray coating is typically used to provide a protective layer (e.g., crankshaft reconditioning and corrosion protection [30]). Figure 1-9 presents a schematic of the process of thermal spraying upon a substrate.

SOKENDAI

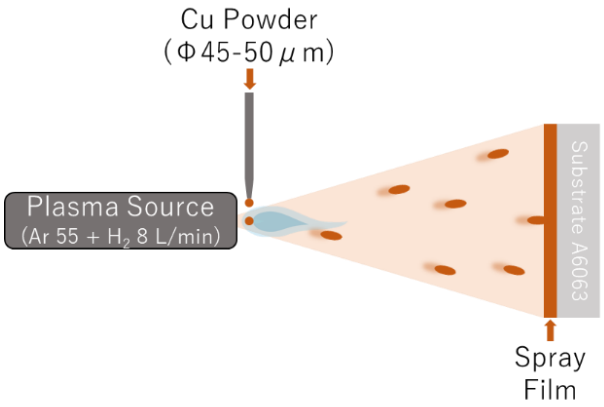

Figure 1-9: Schematic of the process of copper thermal spraying on an aluminum substrate

As will be described later, thermal spraying can produce a very rough surface on various materials. Therefore, it is expected that the thermal spray coating will achieve a low SEY. Furthermore, the thermal spray only needs to be applied in the atmosphere and is convenient for large-area applications. Compared with grooved structures, the protrusions on thermally sprayed coatings are smaller and therefore have less impact on the continuity of the existing beam pipe section; moreover, the application area of thermal spray coating is larger. Compared with laser-ablated surfaces, the technological threshold required by thermal spraying is lower; furthermore, after process optimization, it can reduce the EC to a similar extent at lower cost. This thesis is the first systematic study made of this thermal spray surface from the perspective of ECE suppression in accelerators.

In my Master's report, thermal spray coatings for different materials and spray conditions were produced for the first time, to test whether they could reduce the SEY of the surface [31]. Among these, the copper thermal spray coating (hereinafter referred to as T.S. coating) had a low SEY, and its δ_{max} (the maximum SEY within scanning) reached ~0.7.

In this doctoral thesis, I extend this study to consider the various characteristics of T.S. coating and also apply it to the beam pipe of SuperKEKB LER, to verify its EC suppression effect; finally, I summarize the abovementioned results, to indicate their applicability to actual accelerators.

1.3 Contents of the Thesis

This study can be roughly divided into two major parts. The first part is a small sample test of T.S. coatings in the laboratory. Its aim is to determine the spray conditions that can stably produce a low SEY for large-area spraying (e.g., adjusting the spray angle or surface temperature during spraying, etc). Meanwhile, we observe the surface structure and measure the roughness parameters and surface composition, to clarify the key factors affecting the SEY.

In the second part, we follow up the results of the first part and fabricate a beam pipe with a T.S. coating; this is installed in the SuperKEKB LER, to test its EC reduction effects. The problems encountered during beam pipe production, as well as the most important electron density results and corresponding analyses, are reported here. In addition, we measure the outgassing rate, adhesive strength, impedance, and dust generation rate of the T.S. coating, to evaluate its suitability for accelerators.

The measurement items and discussion topics included in this study are extremely diverse; hence, to help readers quickly grasp the main points, we divided the results into two chapters. Chapter 5 “Results and Discussion” presents the most important contributions of this study, including the measured characteristics of the T.S. coating, the dependence of SEY properties upon spraying temperature, and the ability of T.S.-coated beam pipes to suppress ECs. Chapter 6 “Advanced Discussion” gathers together several interesting but unsubstantiated discussions, including the dependence of SEY properties on the surface structure, the impact of resistive-wall impedances, and the use of simulations to explain the observed electron densities.

SOKENDAI

Chapter 2

Properties of SEYs

There are several models of secondary electron emission [32-34]. The Computer Simulation Technology (CST) software used for the SEY simulations in later chapters was based on the model proposed by Furman and Pivi in 2002 [35]. The formulae for this model are described below, and a brief review of the relationship between roughness and SEY, as presented in the abovementioned Master's report, is given.

2.1 Composition of Secondary Electrons

SOKENDAI

The following explanations have been adapted or reinterpreted from Ref. [35]. When a steady electron current I_0 impinges on a surface, a certain portion I_e is backscattered elastically whilst the rest penetrates into the material. Some of these electrons are scattered by one or more atoms inside the material and reflected back out. These are the so-called "re-diffused" electrons. We call the corresponding current I_r. The rest of the electrons interact in a more complicated way with the material and produce the so-called "true secondary electrons," the current of which we refer to as I_{ts}. The yields for each type of electron are defined as $\delta_e = I_e/I_0$, $\delta_r = I_r/I_0$, and $\delta_{ts} = I_{ts}/I_0$; thus, the SEY (δ) is

$$\delta = \frac{I_e + I_r + I_{ts}}{I_0}, \quad \text{(Eq. 2-1a)}$$

$$= \delta_e + \delta_r + \delta_{ts}, \quad \text{(Eq. 2-1b)}$$

$$= P_1 + 2P_2 + 3P_3 \ldots \quad \text{(Eq. 2-1c)}$$

The P_x in Eq. (2-1c) denotes the probability of generating x secondary electrons in an impact event (P_0 represents the probability of being absorbed); the expectation value for the number of secondary electrons is δ.

A sketch of the electron currents used is presented in Fig. 2-1. Notably, the elastically backscattered and re-diffused electrons are still the original incident electrons but with a

different direction or energy; meanwhile, the true secondary electrons are the low-energy electrons released by the material after the material has absorbed the incident ones.

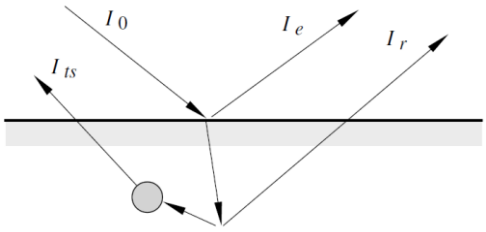

Figure 2-1: Sketch of different components of secondary electrons [35]

There is no fundamental distinction between the backscattering and re-diffusion mechanisms; however, it is convenient to separate them into two components for phenomenological fitting. At the quantum level, the distinction between the three types of electrons is non-physical. Nevertheless, in practice, a conventional criterion applies to the separate measurements of δ_e, δ_r, and δ_{ts} (based on the three main regions) in secondary energy E, expressed as $d\delta/dE$.

As an example, Fig. 2-2 shows the three components' contributions in the case of an incident electron beam of energy E_0 = 300 eV impinging normally upon a stainless-steel surface. The three components of the secondary yield are given by the values of "area [E_1, E_2]," each of which expresses the integrated spectrum between E_1 and E_2. Thus, in this case, δ_{ts} = 1.17, δ_r = 0.75, and δ_e = 0.12, for a total SEY of δ = 2.04. The upper energy cutoff for the true secondary electrons is—somewhat arbitrarily but conventionally—chosen as 50 eV.

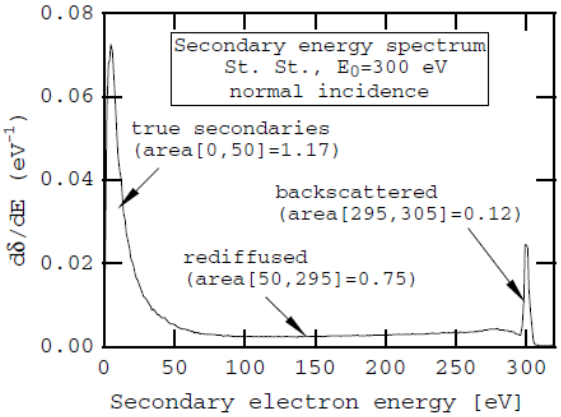

Figure 2-2: Example of the measured energy spectrum $d\delta/dE$ for an unconditioned stainless steel sample at E_0 = 300 eV under normal incidence [35]

2.2 Emission Angles of Secondary Electrons

The emission energy is uncorrelated with the emission angle. Experimentally, it is known [36-37] that the true secondary electrons have a ~cosθ angle distribution, which is fairly independent of the primary incident angle θ_0 and incident energy E_0. This is not exactly true of the elastically reflected and re-diffused electrons, which feature a more complicated angular distribution. Nevertheless, following the principle of simplicity, we assumed the same emission-angle distribution for all electrons, regardless of their physical generation mechanism.

2.3 Formulae for SEY and Secondary Electron Energy

Before introducing the formulae and the three related components of the secondary electron energy, we should first establish the assumptions behind these formulae. The elastically backscattered and re-diffused electrons are only produced in single-electron events (n = 1); meanwhile, the true secondary electrons are produced in events with any number of secondary electrons ($n \geq 1$). This is consistent with the secondary electron emission mechanism described earlier.

SOKENDAI

For the detailed derivation, please refer to Ref. [35]. The following only lists the formulae and explains the parameter meanings. First, the measured and fitted values in the formulae for stainless steel are shown in Fig. 2-3. The colored curves represent the contributions of each component in the overall SEY curve.

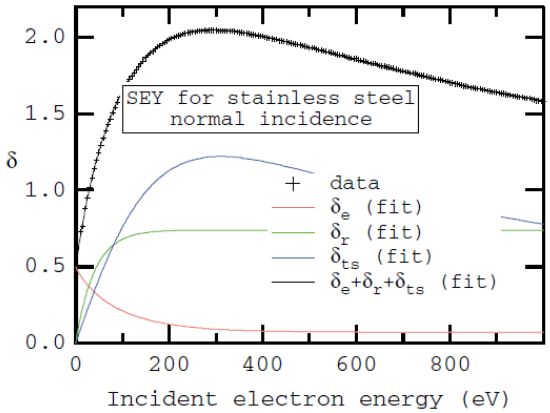

Figure 2-3: SEY profile for stainless steel (SLAC standard 304 rolled sheet, chemically etched and passivated but not conditioned [35]). The fitting parameters are listed in Table 2-1.

2.3.1 Model for Elastically Backscattered Electron

The formula for δ_e under normal incidence ($\theta_0 = 0$) can be expressed as

$$\delta_e(E_0, 0) = P_{1,e}(\infty) + \left[\hat{P}_{1,e} - P_{1,e}(\infty)\right] e^{-(|E_0 - \hat{E}_e|/W)^p/p}, \qquad \text{(Eq. 2-2)}$$

where E_0 is the incident electron energy, $P_{1,e}(E_0)$ is the probability of an event emitting one elastically backscattered electron, $P_{1,e}(\infty)$ is the constant value that $P_{1,e}(E_0)$ tends to when the incident energy is infinite, $\hat{P}_{1,e}$ is the maximum value of $P_{1,e}(E_0)$ when the incident energy is $\hat{E}_e$, and W and P are adjustable constants. The curve is shown by the red line in Fig. 2-3. When the incident energy E_0 is 0, δ_e is its maximum value, $\hat{P}_{1,e} = 0.5$; as E_0 increases, δ_e decreases exponentially and gradually approaches $P_{1,e}(\infty) = 0.07$.

The energy probability function $f_{1,e}$ is

$$f_{1,e} = \theta(E)\theta(E_0 - E)\delta_e(E_0, \theta_0) \frac{2e^{-\frac{(E-E_0)^2}{2\sigma_e{}^2}}}{\sqrt{2\pi}\sigma_e \operatorname{erf}\left(\frac{E_0}{\sqrt{2}\sigma_e}\right)}. \qquad \text{(Eq. 2-3)}$$

Here, E is the secondary electron energy, $\theta(E_0 - E)$ ensures that the energy of each secondary electron does not exceed the incident energy, and $\delta_e(E_0, \theta_0)$ is a function that is similar to Eq. (2-2) but incorporates the incident angle (introduced later). As described in Section 2.1, the integral of the secondary electron energy probability function generated by a fixed incident energy E_0 over E is equal to $\delta_e(E_0)$:

$$\int_0^{E_0} f_{1,e}(E)dE = \delta_e(E_0). \qquad \text{(Eq. 2-4)}$$

2.3.2 Model for Re-diffused Electron

The δ_r under normal incidence ($\theta_0 = 0$) is modeled as follows:

$$\delta_r(E_0, 0) = P_{1,r}(\infty)\left[1 - \exp\left(-\left(\frac{E_0}{E_r}\right)^r\right)\right]. \qquad \text{(Eq. 2-5)}$$

In Fig. 2-3, we see that the green line representing $\delta_r(E_0, 0)$ starts a short and rapid climb from zero before finally remaining close to $P_{1,r}(\infty) = 0.74$. The δ_r act similar to the offset of $P(\infty)$ in the δ profile.

The energy probability function $f_{1,r}$ is

$$f_{1,r} = \theta(E)\theta(E_0 - E)\delta_r(E_0, \theta_0) \frac{(q+1)E^q}{{E_0}^{q+1}}, \qquad \text{(Eq. 2-6)}$$

which also satisfies the normalization condition:

$$\int_0^{E_0} f_{1,r}(E)dE = \delta_r(E_0). \qquad \text{(Eq. 2-7)}$$

2.3.3 Model for True secondary Electron

The δ_{ts} is given by

$$\delta_{ts}(E_0,\theta_0) = \hat{\delta}_{ts}(\theta_0)\frac{s\frac{E_0}{\hat{E}_{ts}(\theta_0)}}{s-1+\left(\frac{E_0}{\hat{E}_{ts}(\theta_0)}\right)^s}, \qquad \text{(Eq. 2-8)}$$

where $\hat{\delta}_{ts}(\theta_0)$ is the peak value of $\delta_{ts}(E_0,\theta_0)$, and the corresponding incident energy is $\hat{E}_{ts}(\theta_0)$. s is an adjustable parameter that must exceed 1. Typically, when E_0 < ~40 eV, δ_e exceeds δ_r; when E_0 > ~40 eV, δ_{ts} exceeds δ_r. In actual situations involving the EC effect, the incident energies of electrons are several hundreds of eV [2]; hence, δ_{ts} is more important than δ_e, especially for a flat (smooth) surface. For rough or grooved surfaces, the secondary electrons tend to hit the adjacent surfaces with a low energy of ~ 10 eV; thus, δ_e can become an important factor.

In terms of the energy spectrum function, we assume that

$$f_{n,ts} = \theta(E)F_n E^{p_n-1}e^{-E/\epsilon_n}, \qquad \text{(Eq. 2-9)}$$

where p_n and ϵ_n are phenomenological parameters [however, the finiteness of $\delta(E_0,\theta_0)$ demands that p_n > 0]. The calculation of F_n is more complicated (see Ref. [35]). Equations (2-3), (2-6), and (2-9), which describe the secondary electron energy used to fit the data in Fig. 2-2, are shown in Fig 2-4.

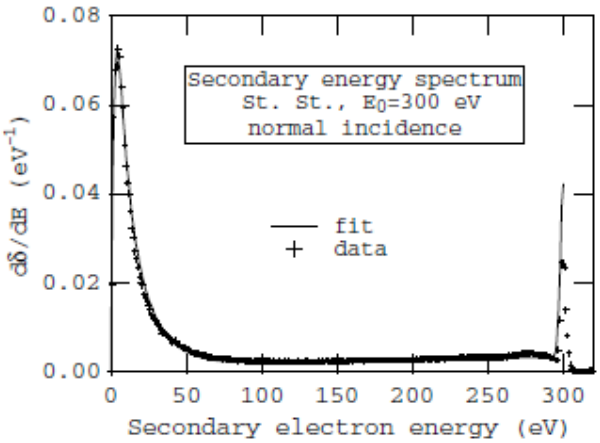

Figure 2-4: Equations (2-3), (2-6), and (2-9) fitting the data in Fig. 2-2 [35]

2.3.4 Incident-angle Dependence of SEY

The incident-angle dependence of the total SEY is found to be well fitted by a multiplicative factor of the form $1 + a_1(1 - \cos^{a_2}\theta_0)$ for incident angles in the range $0 \leq \theta_0 \lesssim 84^\circ$ [35]. The same form is assumed for all three components of the SEY; thus,

$$\delta_e(E_0, \theta_0) = \delta_e(E_0, 0)[1 + e_1(1 - \cos^{e_2}\theta_0)], \quad \text{(Eq. 2-10a)}$$

$$\delta_r(E_0, \theta_0) = \delta_r(E_0, 0)[1 + r_1(1 - \cos^{r_2}\theta_0)], \quad \text{(Eq. 2-10b)}$$

$$\hat{\delta}_{ts}(\theta_0) = \hat{\delta}_{ts}(0)[1 + t_1(1 - \cos^{t_2}\theta_0)], \quad \text{(Eq. 2-10c)}$$

$$\hat{E}_{ts}(\theta_0) = \hat{E}_{ts}(0)[1 + t_3(1 - \cos^{t_4}\theta_0)]. \quad \text{(Eq. 2-10d)}$$

Table 2-1 lists the parameters used to fit the stainless steel (see Fig. 2-3) and the machined copper surface considered in this study. Figure 2-5 shows the three components of the SEY fitted using the formulae and measured values.

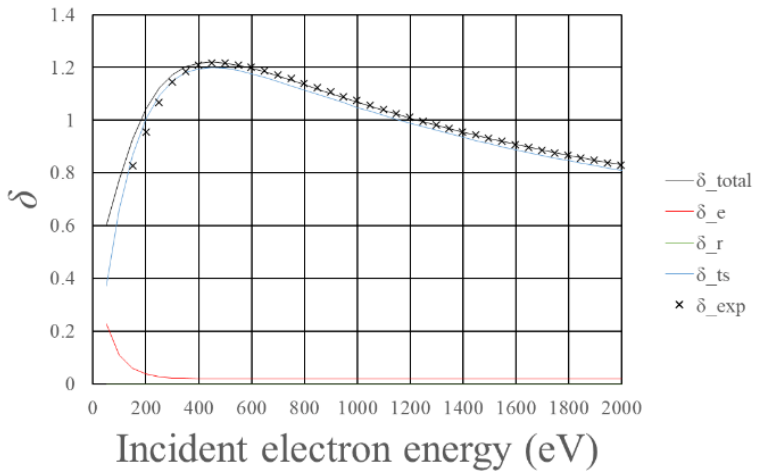

Figure 2-5: SEY profile for machined copper surface. The fitting parameters are listed in Table 2-1

2.4 Influence of Surface Structure on SEY

The SEY of a surface can vary in response to many factors, including the apparatus used to measure the SEY and the surface's cleanliness, history, composition, and structure. In the Master's report [31], we used a program written by Visual Basic for Applications (VBA) to discuss the relationship between the SEY and roughness parameters (a quantification of surface structure). Surfaces of different sizes and patterns (triangular and trapezoidal grooves/protrusions) were inputted to the simulation. Their design drawings and parameters are shown in Fig. 2-6.

Table 2-1: Parameters used in the SEY formulae to fit the measured data for stainless steel [35] and copper

	Stainless steel [35]	Copper
	Backscattered electrons	
$P_{1,e}(\infty)$	0.07	0.02
$\hat{P}_{1,e}$	0.5	0.496
$\hat{E}_e$ (eV)	0	0
W (eV)	100	60.86
p	0.9	1
σ_e (eV)	1.9	2
e_1	0.26	0.26
e_2	2	2
	Re-diffused electrons	
$P_{1,r}(\infty)$	0.74	0
E_r (eV)	40	0.041
r	1	0.104
q	0.4	0.5
r_1	0.26	0.26
r_2	2	2
	True secondary electrons	
$\hat{\delta}_{ts}$	1.22	1.2
$\hat{E}_{ts}$ (eV)	310	450
s	1.813	1.5
t_1	0.66	0.66
t_2	0.8	0.8
t_3	0.7	0.7
t_4	1	1
	Total SEY	
$\hat{E}_t$ (eV)	292	450
$\hat{\delta}_t$	2.05	1.22

SOKENDAI

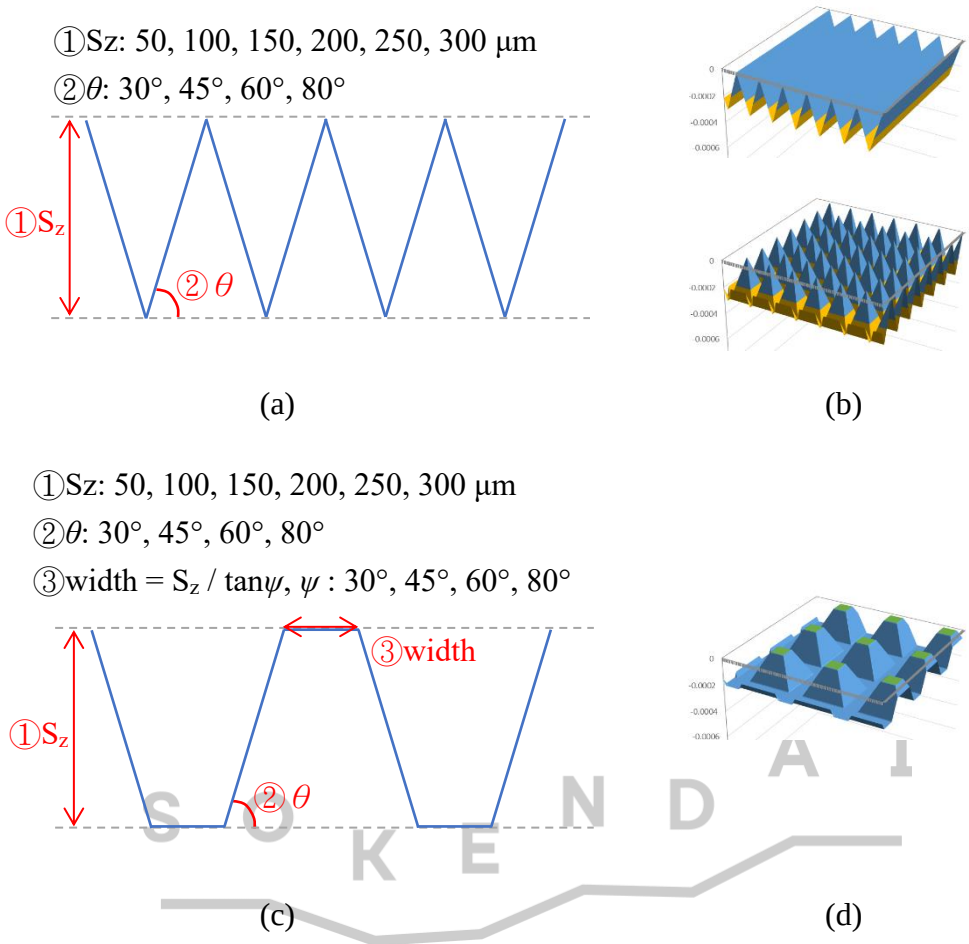

Figure 2-6: (a) Parameters and (b) models of the triangular grooves and protrusions; (c) parameters of the trapezoidal protrusions; and (d) model of the trapezoidal protrusions

The simulation findings are as follows:

1. Grooves have the same SEY profile (δ vs. incident electron energy) as protrusions, with the same patterns (e.g., triangular and trapezoidal protrusions have different patterns) and size parameters (*Sz*, θ, width, etc.).
2. The SEY does not vary with the scale of the surface structure.
3. δ_{max} is inversely proportional to *Sdr* (the developed area ratio), and the proportional coefficient differs under different patterns.

Sdr (described in detail in the next chapter) refers to the surface area increase. The larger the *Sdr*, the rougher and sharper the surface structure is, and the easier it is to trap secondary electrons. Figure 2-7(a) shows the simulation results given in the Master's report, from which evidence for the above conclusions can be obtained.

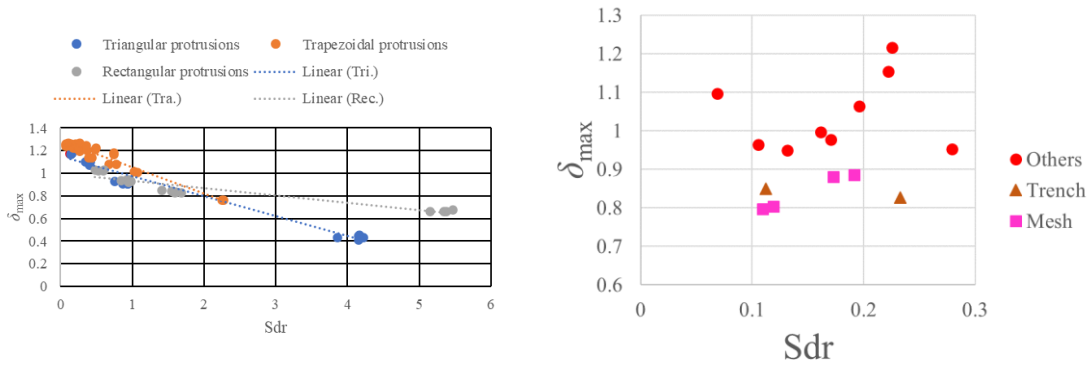

(a) (b)

Figure 2-7: (a) Simulated δ_{max} as a function of *Sdr* for triangular, trapezoidal, and rectangular protrusions [31]; (b) Measured δ_{max} as a function of *Sdr* for thermal spray surfaces [31]

However, in the Master's report, the relationship between δ_{max} and *Sdr* for the thermal spray surfaces did not show a clear correlation, as indicated in Fig. 2-7(b). There were two possible reasons for this:

1. The surface pattern of each thermal spray sample differed, so their results deviated.
2. The roughness measurements were insufficiently accurate.

In this study, we used another program called CST to perform simulations, applied a more precise microscope to measure the roughness parameters, and made several groove samples, to verify the differences between the simulated and experimental results.

SOKENDAI

Chapter 3

Experiments

3.1 SEY Properties of T.S. Coatings in Laboratory

In the first part of the experiment, in addition to measuring the SEY of the T.S. coating, we sought to determine what factors would affect the SEY. Therefore, we collected scanning electron microscopy (SEM) images as well as the roughness parameters and surface compositions for the T.S. coatings. The details of each measurement are described below.

3.1.1 SEY

SOKENDAI

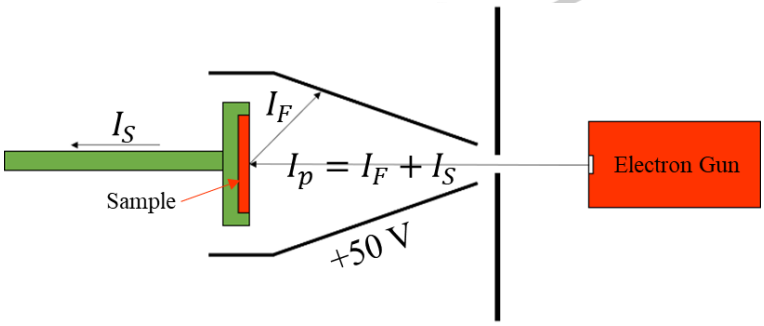

Figure 3-1: Schematic of the SEY measurement apparatus

Figure 3-1 shows a schematic of the SEY measurement apparatus. The electron beam (energy range: 150–2000 eV) was generated via an electron gun (EG3000, LK Technologies, Inc). The measuring area on the sample was a circle with a diameter of ~1–2 mm. The secondary electrons were collected using a Faraday cup. The currents through the sample and the Faraday cup were recorded to calculate the SEY. The total SEY (or δ) was obtained from

$$\delta = \frac{I_F}{I_P} = \frac{I_F}{I_F + I_S}, \qquad \text{(Eq. 3-1)}$$

where I_S is the current measured at the sample, I_F is the current on the Faraday cup, and I_P is the primary electron beam current. The sample was at ground potential level, and the Faraday cup was biased at +50 V to attract secondary electrons. Each current was measured using a current amplifier (Keithley 486 and Keithley 2400). The electron beam entered the sample at right angles to the surface.

Experimental procedure

1. Install the sample and start pumping.
2. Bake the apparatus containing the sample at 160 ℃ for 20 h. We set the working pressure to 10^{-7} Pa.
3. Measure the SEY within 150–2000 eV of the primary electron energy (E_p), with a step of 50 eV. We set the beam current to 10^{-9} A during the measurement.
4. Perform conditioning (i.e., electron-beam bombardment). The conditioning area on the sample was a circle with a diameter of ~5 mm. The E_p during conditioning was 350 eV, near the E_{max} of flat aluminum and copper surfaces. The beam current was ~7 μA. After 72 h conditioning, the total electron dose reached ≈ 1 $\times 10^{-1}$ C/mm^2.
5. Measure the SEY again after conditioning periods of 2, 7, 24, 48, and 72 hours.

SOKENDAI

3.1.2 SEM Imaging

The topography of the surface of each sample was observed via SEM (VE-8800, Keyence Corp.), as shown in Fig. 3-2. The typical magnifications used in this study were 100× and 500×.

Figure 3-2: VE-8800 scanning electron microscope

3.1.3 Roughness Parameters

The roughness parameters were obtained using the 3D laser scanning confocal microscope (VK-X1100, Keyence Corp.) at Tohoku University (shown in Fig. 3-3). The magnifications we used were 20×, 50×, and 150×. The vertical accuracy was less than 0.2 + L/100 μm (L = measuring length) and the lateral accuracy was within 2% of the measured value [38]. The measured roughness parameters in this study included *Sa* (arithmetical mean height), *Sz* (maximum height), *Sq* (root mean square height), *Spd* (Density of peaks), and *Sdr* (developed interfacial area ratio).

Figure 3-3: VK-1100 laser microscope

SOKENDAI

3.1.3.1 *Sa* (arithmetical mean height)

Sa is the extension of *Ra* (arithmetical mean height of a line) to surfaces. It expresses, as an absolute value, the difference in height [Z(x,y)] for each point with respect to the arithmetical mean of the surface, as shown in Fig. 3-4 [39], where *A* denotes the observed area. This parameter is generally used to evaluate surface roughness. *Sa* is expressed as

$$S_a = \frac{1}{A}\iint_A |Z(x,y)|dxdy. \qquad \text{(Eq. 3-2)}$$

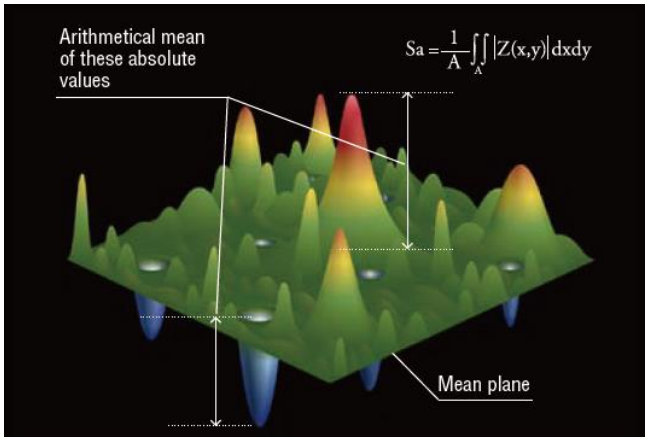

Figure 3-4: Schematic of *Sa* [39]

3.1.3.2 *Sz* (maximum height)

Sz is defined as the sum of the largest peak height value (S_p) and largest valley depth value (S_v) within the defined area:

$$S_z = S_p + S_v. \quad \text{(Eq. 3-3)}$$

3.1.3.3 *Sq* (root mean square height)

Sq denotes the root mean square value of ordinate values within the definition area. It is equivalent to the standard deviation of heights:

$$S_q = \sqrt{\frac{1}{A}\iint_A Z^2(x,y)dxdy}. \quad \text{(Eq. 3-4)}$$

3.1.3.4 *Spd* (density of peaks)

Spd (density of peaks) denotes the number of peaks per unit area. Figure 3-5 shows the case in which *Spd* is equal to 8 /mm^2.

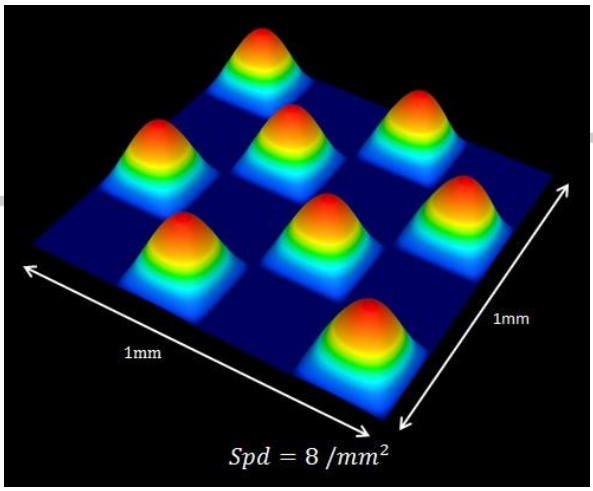

Figure 3-5: Schematic of *Spd* [39]

3.1.3.5 *Sdr* (developed interfacial area ratio)

This parameter is expressed as the percentage of the defined area's additional surface area contributed by texture, as compared to the planar definition area:

$$Sdr = \frac{1}{A}\iint_A \left(\sqrt{1 + \left(\frac{\partial Z(x.y)}{\partial x}\right)^2 + \left(\frac{\partial Z(x.y)}{\partial y}\right)^2} - 1\right) dxdy. \quad \text{(Eq. 3-5)}$$

The *Sdr* of a completely flat surface is zero. When a surface has a slope, its *Sdr* value becomes larger. For example. the surface on the right in Fig. 3-6 is a plane with gradient components of 45°; for it, $Sdr = \sqrt{2} - 1 = 0.414$ [39].

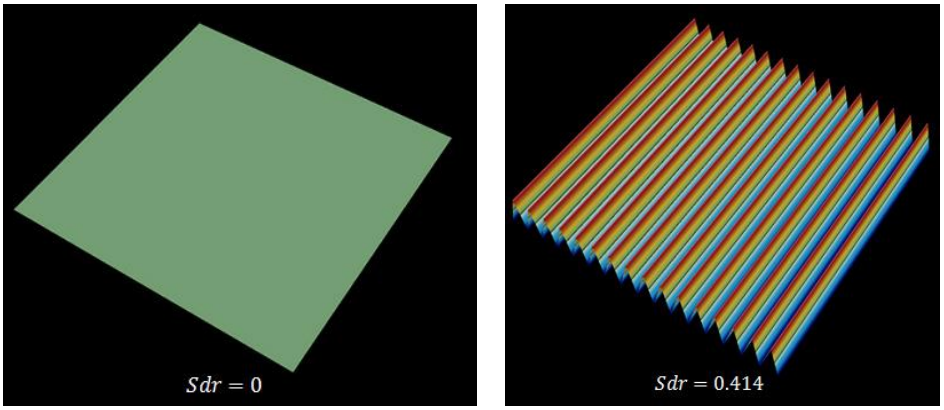

Figure 3-6: Schematic of *Sdr* [39]

3.1.4 Surface Composition

The surface compositions were investigated using ex-situ X-ray photoelectron spectroscopy (XPS) at the Industrial Technology Innovation Center of Ibaraki Prefecture and Industrial Technology Center of Yamanashi Prefecture. The XPS systems were the Theta Probe (Thermo Fisher Scientific Inc.) and JPS-9010TR (JEOL, Ltd), respectively. The measured signal was taken only a few nanometers deep from the surface.

SOKENDAI

The surface composition was measured before and after conditioning. It should be noted that the XPS measurement in this study was a qualitative measurement. The requirements for quantitative measurement with XPS are strict, and the rough surface affects the position and width of the peak; this makes it difficult to accurately quantify each component [40]. The XPS peak fitting in this study was performed using the XPSPEAK41 software.

Alongside general surface composition measurements, we commissioned the Industrial Technology Innovation Center of Ibaraki Prefecture to perform depth profiling for one of the T.S. samples. The ion gun was EX05 (Thermo Fisher Scientific Inc.), which can generate a 3 keV argon ion beam. The sputter rate was 0.18 nm/s for copper at an ion current density of 100 μA/cm^2. The ion current used in this study was 2 μA, and the irradiation area was a dot with a diameter of 800 μm; thus, the sputter rate was ~4 × 0.18 nm/s. The total irradiation time was 30572 seconds; hence, the etching depth was ~22 μm. It should be noted that the sputter rate differs according to the tested element or compound; however, the oxide layer on the T.S. coating was thin, so the sputter rate for copper was used to roughly estimate the etching depth.

3.2 Feasibility of T.S. Coatings in Accelerators

In the second part of the experiment, we sought to examine the effects of the T.S.-coated beam pipe on EC reduction. In addition, certain measurements were also required (e.g., outgassing rate, surface resistance, dust generation, and adhesive strength) to investigate whether T.S. coating is suitable for accelerators.

3.2.1 Measurement of Electron Density in a Beam Pipe

After the abovementioned small sample tests, a beam pipe with a T.S. coating was fabricated and installed into the SuperKEKB LER, to test its EC reduction effect; this was measured using a retarding field analyzer (RFA) type detector, as shown in Fig. 3-7. The details of this detector can be found in Ref. [41].

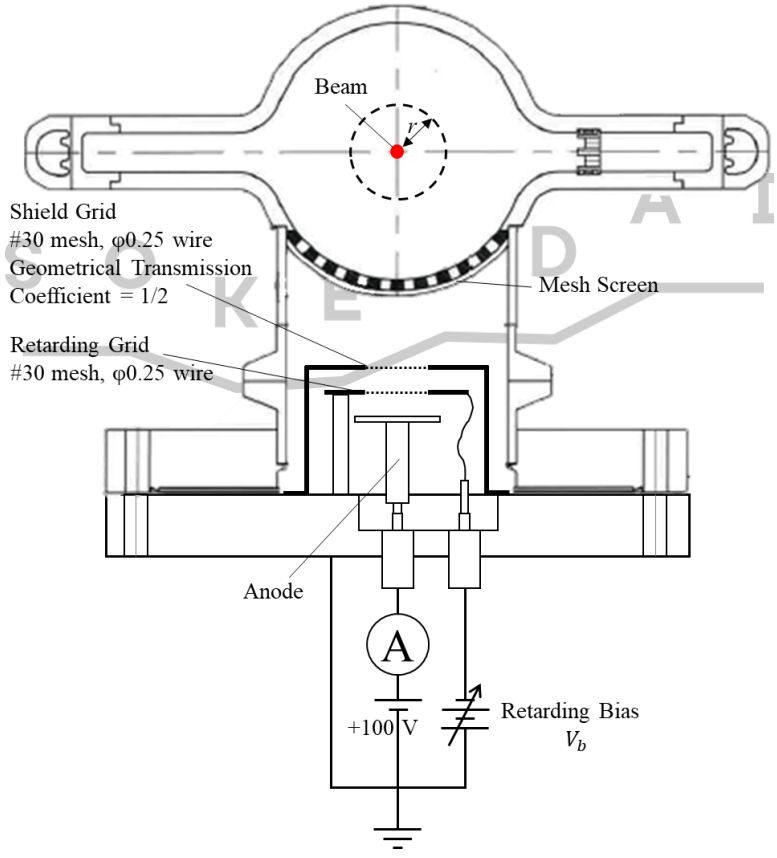

Figure 3-7: Schematic of an RFA at the port of a SuperKEKB LER beam pipe

3.2.1.1 Measuring principle

The beam was assumed to be axisymmetric, located in the center of the beam pipe, and to have a volume. The beam pipe section was a circle with a radius of 45 mm, including antechambers.

In cylindrical coordinates, let the beam direction be +z. As the speed of a positron bunch containing charge Q approaches the speed of light, the direction of the electric field it generates will gradually be squeezed exclusively into the r direction, as shown in Fig. 3-8.

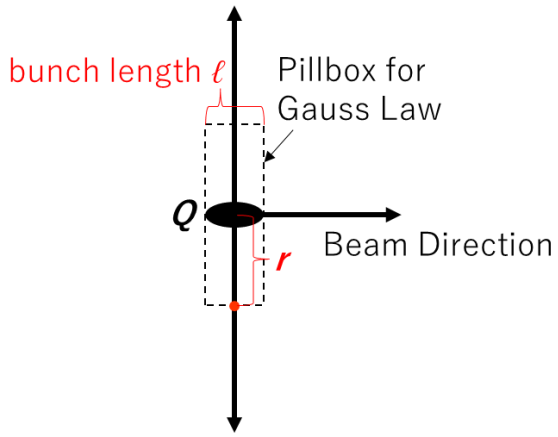

Figure 3-8: Direction of the electric field generated by charged particles moving at the speed of light

SOKENDAI

Let the bunch length be ℓ. Taking a pillbox Gaussian surface with a radius of r and a length of ℓ, the magnitude of the electric field as observed at a lateral distance r from the bunch can be obtained as

$$E_r = \frac{Q}{2\pi\epsilon_0 rl} = \frac{e \cdot N_b}{2\pi\epsilon_0 rl}, \qquad \text{(Eq. 3-6)}$$

where e is the charge of a positron, N_b is the number of positrons in a bunch, and ϵ_0 is the vacuum permittivity. When an electron is placed at a lateral distance of r, the lateral momentum it receives from the passing bunch is

$$\Delta p = F \cdot \Delta t = eE_r \cdot \Delta t = \frac{e^2 \cdot N_b}{2\pi\epsilon_0 rl}\frac{l}{c} = \frac{e^2 \cdot N_b}{2\pi\epsilon_0 rc}, \qquad \text{(Eq. 3-7)}$$

where c is the speed of light. We introduce the classical radius of the electron r_e,

$$r_e = \frac{e^2}{4\pi\epsilon_0 m_e c^2}, \qquad \text{(Eq. 3-8)}$$

where m_e is the electron mass. Combining Eqs. (3-8) and (3-7) gives an alternative form of the lateral momentum changes:

$$\Delta p = \frac{2r_e}{r} N_b m_e c. \qquad \text{(Eq. 3-9)}$$

This expression matches that in [41]. Most electrons have low initial energies; hence, if r is small enough, Δp is almost the final momentum of the electron (i.e., the space charge

of the cloud near the beam is negligible).

When a retarding bias V_b is applied, the kinetic energy of the electrons that can be received by the anode must overcome this potential energy, which can be written as

$$e \cdot V_b \leq \frac{(\Delta p)^2}{2m_e} = 2 \cdot \frac{r_e^2}{r^2} N_b^2 m_e c^2, \qquad \text{(Eq. 3-10)}$$

$$r^2 \leq 2 \cdot \frac{r_e^2}{e \cdot V_b} N_b^2 m_e c^2. \qquad \text{(Eq. 3-11)}$$

In other words, the detected electrons come only from a cylindrical region in the center of the beam pipe of radius *r*. However, considering the structure on the path of the electrons to the anode, the volume of this cylindrical region is expressed as

$$V_{obs}(V_b) = Ar^2 = 2 \cdot A \frac{r_e^2}{e \cdot V_b} N_b^2 m_e c^2, \qquad \text{(Eq. 3-12)}$$

where *A* can be regarded as the acceptance of the detector. Using the structure of the beam pipe, we estimated *A* as 0.0003 m; this is multiplied by the geometrical transmission coefficient of the shield grid and retarding grid to give $A = 0.0003 \times 1/4$ m.

From the received DC current value $I_{obs}(V_b)$, the number of electrons that are accelerated by a bunch and capable of reaching the electron monitor $\mu(V_b)$ can be evaluated as

$$\mu(V_b) = \frac{I_{obs}(V_b)}{e \cdot n_b \cdot f_{rev}}, \qquad \text{(Eq. 3-13)}$$

where n_b is the number of bunches, and f_{rev} is the revolution frequency of the stored beam.

Finally, the average electron density *D* within distance *r* from the beam is given by

$$D = \frac{\mu(V_b)}{V_{obs}(V_b)} = \frac{I_{obs} \cdot V_b \cdot n_b}{2A} \left(\frac{1}{I_{beam}}\right)^2 \frac{f_{rev} \cdot e^2}{r_e^2 \cdot m_e c^2}, \qquad \text{(Eq. 3-14)}$$

where I_{beam} is the total current of the beam. The value of the last fraction term is ~3.922 $\times$ 10^9 for the SuperKEKB. It should be noted that this density represents a time average of the density at a special timing (i.e., just before the arrival of a bunch). This is important when comparing the measurement against simulations, which indicates that the density of the e-cloud near the beam varies rapidly [42].

3.2.1.2 Limitations of the method

To neglect the initial kinetic energy of the electrons, a higher V_b is better; however, this also means that *r* will be smaller. When *r* become comparable to the beam size, the above formulas cannot be used. This sets an upper limit on V_b.

Another requirement for V_b is that the electrons must enter the detector before the next bunch, to clarify the relationship between the single kick of a bunch and the observed current. This condition can be written as

$$\frac{r_c}{v_{min}} < \frac{s_b}{c} \Rightarrow v_{min} > \frac{r_c}{s_b} c, \qquad \text{(Eq. 3-15)}$$

where r_c is the radius of the beam pipe, s_b is the bunch space, and v_{min} is the lowest velocity of the electron (determined by the retarding bias V_b). Converting v_{min} to an expression containing V_b gives the lower limit of V_b:

$$e \cdot V_b = \frac{m_e (v_{min})^2}{2} > \frac{m_e c^2}{2} \left(\frac{r_c}{s_b}\right)^2. \qquad \text{(Eq. 3-16)}$$

The following are the required constant values and parameters of SuperKEKB:

$e = 1.602 \times 10^{-19}$ [C] $\qquad m_e = 9.11 \times 10^{-31}$ [kg]

$c = 3 \times 10^{-8}$ [m/s] $\qquad r_c = 0.045$ [m]

$s_b = \begin{cases} 1.13\ [m], when\ n_b = 2500 \\ 3.63\ [m], when\ n_b = 783 \end{cases} \qquad f_{rev} = \frac{c}{3016}.$

Thus, $V_b > 40$–406 V can be obtained. In this study, V_b was 500 V for most measurements. The corresponding radius of the observed region was given [from Eq. (3-11)] as

$$r = r_e N_b \sqrt{\frac{2m_e c^2}{e \cdot V_b}} = r_e \frac{I_{beam}}{e \cdot n_b \cdot f_{rev}} \sqrt{\frac{2m_e c^2}{e \cdot V_b}} = \frac{r_e \cdot I_{bunch}}{e \cdot f_{rev}} \sqrt{\frac{2m_e c^2}{e \cdot V_b}}, \qquad \text{(Eq. 3-17)}$$

where I_{bunch} is the average current carried by a bunch, typically referred to as the bunch current. If V_b is fixed as a constant (e.g., 500), then *r* is only related to I_{bunch}, as shown in Fig. 3-9. For a low bunch current, *r* is close to the beam size. The electron density estimated for bunch currents below 0.2 mA is unreliable.

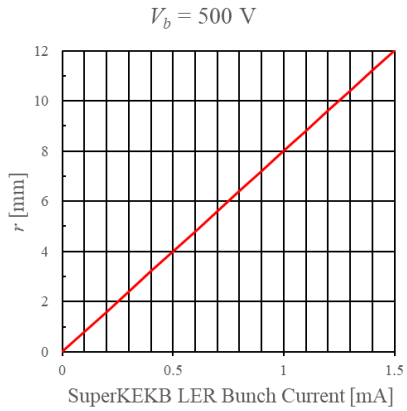

Figure 3-9: Radius of the observed volume as a function of bunch current in SuperKEKB LER

It is important to note that the observed volume depends on two parameters: retarding bias and bunch current (Eq. 3-12). If the retarding bias is kept constant, the volume differs for a different bunch current. If the retarding bias is changed with the bunch current to maintain a constant volume, data at a low bunch current become less reliable.

SOKENDAI

3.2.1.3 Measurement with a vertical magnetic field B_y

A previous study [43] using the same detector found that the electron density obtained from the beam pipe with a groove and TiN coating did not significantly differ from that of the beam pipe with only a TiN coating, although the former had a lower δ_{max} in the laboratory measurements. This may be because the electron densities of both were very low (of the order of 10^{11} [m^{-3}]); hence, the photoelectrons made up more of the e-cloud than the secondary electrons. Moreover, when the detected current is too small, individual differences between electron monitors or their locations may show up. Hence, an adjustable weak vertical magnetic field B_y was applied around the monitor. On the one hand, the direction of motion of the received electrons could be selected as either up or down; that is, the received electrons mainly originated from the grooved part. On the other hand, this magnetic field could prevent photoelectrons from escaping from the antechambers; that is, it reduced the proportion of photoelectrons amongst the received electrons. Thus, when B_y increased (i.e., the source of the received electrons was gradually concentrated into the area with grooves) and the influence of photo-electrons was reduced, the SEY properties of the grooves were made visible. However, because of the influence of the magnetic field, the formula used to calculate the electron density was no longer applicable.

For example, Fig. 3-10 [43] showed the received current ratios obtained by different beam pipes (i.e., TiN and TiN groove beam pipes) as a function of B_y. These current ratios were normalized by the value at B_y = 0 to reduce the influence of individual differences between electron monitors. The received current under higher values of B_y was considered to contain a higher SE component; hence, the downward trend of the received current ratio indicated that the SEY corresponding to the numerator (i.e., the TiN groove or Al groove) was lower than the SEY corresponding to the denominator (i.e., the flat TiN or Al surface).

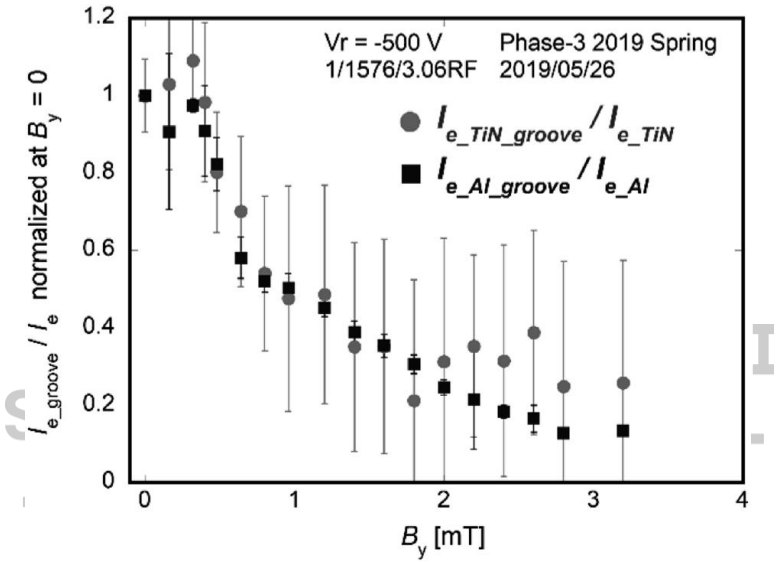

Figure 3-10: Normalized current ratios $I_{e\_TiN\_groove}/I_{e\_TiN}$ and $I_{e\_Al\_groove}/I_{e\_Al}$ as a function of B_y [43]

In this study, the electron density obtained in the T.S.-coated beam pip was also of the order of 10^{11} [m^{-3}]; hence, the same experimental method was used. The solenoid coils (to apply a weak magnetic field in the y-direction) were installed around all four electron monitors, as shown in Fig. 3-11. A coil current of 2.5 A was used to provide ~20 Gauss of magnetic flux density. The scanning current range was 0–3 A.

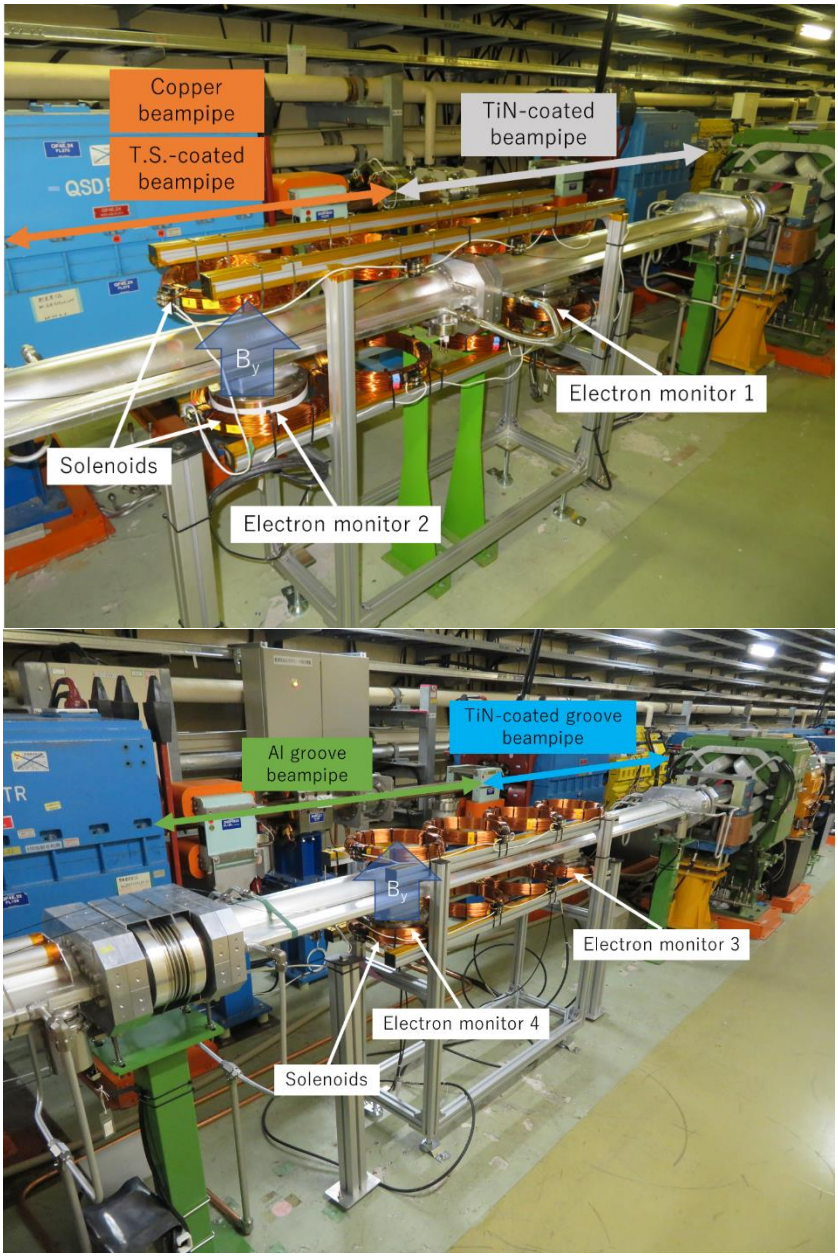

Figure 3-11: Photos of the solenoid coils set around all electron monitors

3.2.2 Other Measurement Items

3.2.2.1 Outgassing rate

The apparatus used to measure the outgassing rate is shown in Fig. 3-12. The extractor gauge model was IE 514 (Leybold Inficon). The measurement was based upon the conductance modulation method (CM method) [44]; this is expressed as

$$P = \frac{Q}{S}, \qquad \text{(Eq. 3-18)}$$

where P is pressure [Pa], Q is the gas load [Pa·m^3/s], and S is the pumping speed [m^3/s]. Because the pumping speed from Chamber 1 to Chamber 2 was restricted by an orifice of conductance C, the pressures in Chamber 1 for open (P_o) and closed (P_c) orifices can be obtained using

$$(orifice\ open)\ P_o - P_2 = \frac{a+b}{C_o}, \quad \text{(Eq. 3-19)}$$

$$(orifice\ closed)\ P_c - P_2 = \frac{a+b}{C_c}, \quad \text{(Eq. 3-20)}$$

where a [Pa·m^3/s] is the outgassing per second from the inner wall of Chamber 1, b [Pa·m^3/s] is that from the sample, P_2 is the pressure in Chamber 2, and C_o and C_c denote the conductance with the orifice open and closed, respectively.

Next, the total outgassing per second in Chamber 1 can be obtained by subtracting Eq. (3-19) from Eq. (3-20), as

$$P_c - P_o = \frac{a+b}{C_c} - \frac{a+b}{C_o}, \quad \text{(Eq. 3-21)}$$

$$a+b = \frac{C_o C_c (P_c - P_o)}{C_o - C_c}. \quad \text{(Eq. 3-22)}$$

SOKENDAI

For the apparatus in this study, assuming that the average molecular weight of air is 28.96 and the temperature is 20 ℃, we found that C_o = 0.226 [m^3/s], C_c = 0.043 [m^3/s], and $\frac{C_o C_c}{C_o - C_c}$ = 0.053 [m^3/s]. The inner surface area of the apparatus was 3.52 × 10^5 mm^2.

The value of a can be obtained first by measuring without the sample; the value of b can be obtained by measuring with the sample. It is conventional to divide b by the total area of the sample to obtain the "outgassing rate" in units of Pa·m/s. In this study, the outgassing rate was measured for ~100 h after baking at 160 ℃ for 24 h. Before measuring any sample, the background value was measured once using the same experimental procedure. When the chamber was opened, dry nitrogen gas was introduced into the chamber to avoid changes in the background value.

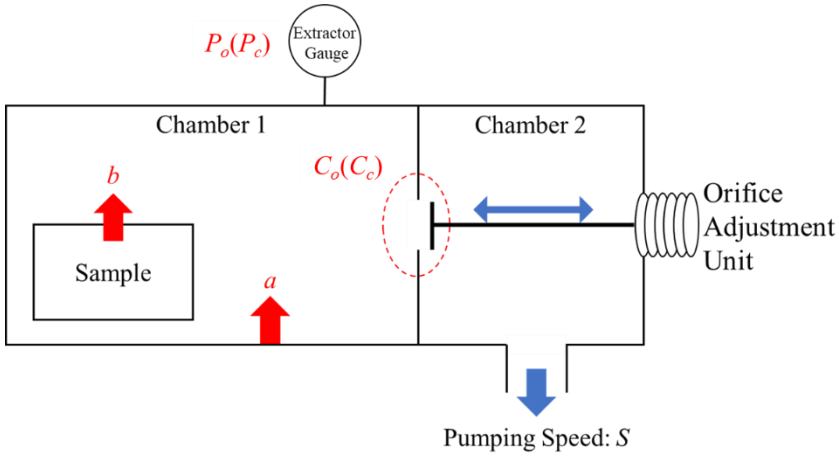

Figure 3-12: Sketch of the apparatus for outgassing rate measurements

3.2.2.2 Surface resistance

To estimate the conductivity (σ) of the sample surfaces in the microwave regime, the quality factor (Q factor) was measured via a cavity-resonator method [45] with the setup shown in Fig. 3-13(a). A cylindrical cavity was connected by two signal wires to the network analyzer (N5230C, Agilent Technologies, Inc). An internally polished copper bucket with a circumferential "belt," as shown in Fig. 3-13(b), was combined with the disk-shaped sample to form a closed cavity. The size of the sample was 120 mm in diameter and 15 mm in thickness. The surface to be measured was a circle with a center diameter of 96 mm; the remaining outer ring component needed to be polished to a roughness *Ra* of less than 1 μm, to ensure close contact with the copper bucket.

The TE011 mode was selected to measure the Q value. The magnetic field distribution for this mode, as shown in Fig. 3-13(c), includes r and z components; meanwhile, the electric field distribution included only the φ direction component. Most importantly, the current on the sidewall and the surface at either end was only in the φ direction; hence, current did not pass through the contact surface between the sample and copper bucket; this increases the accuracy of the Q value measurement.

However, for a perfectly cylindrical cavity, the resonant frequency of the TE011 mode matches that of the TM111, which is undesirable. Therefore, a "belt" structure was added in the center of the cylinder, to distinguish between the resonant frequencies of TE011 and TM111. The resonant frequencies for this cavity under TE011 and TM111 were ~5.044 and 5.068 GHz, respectively.

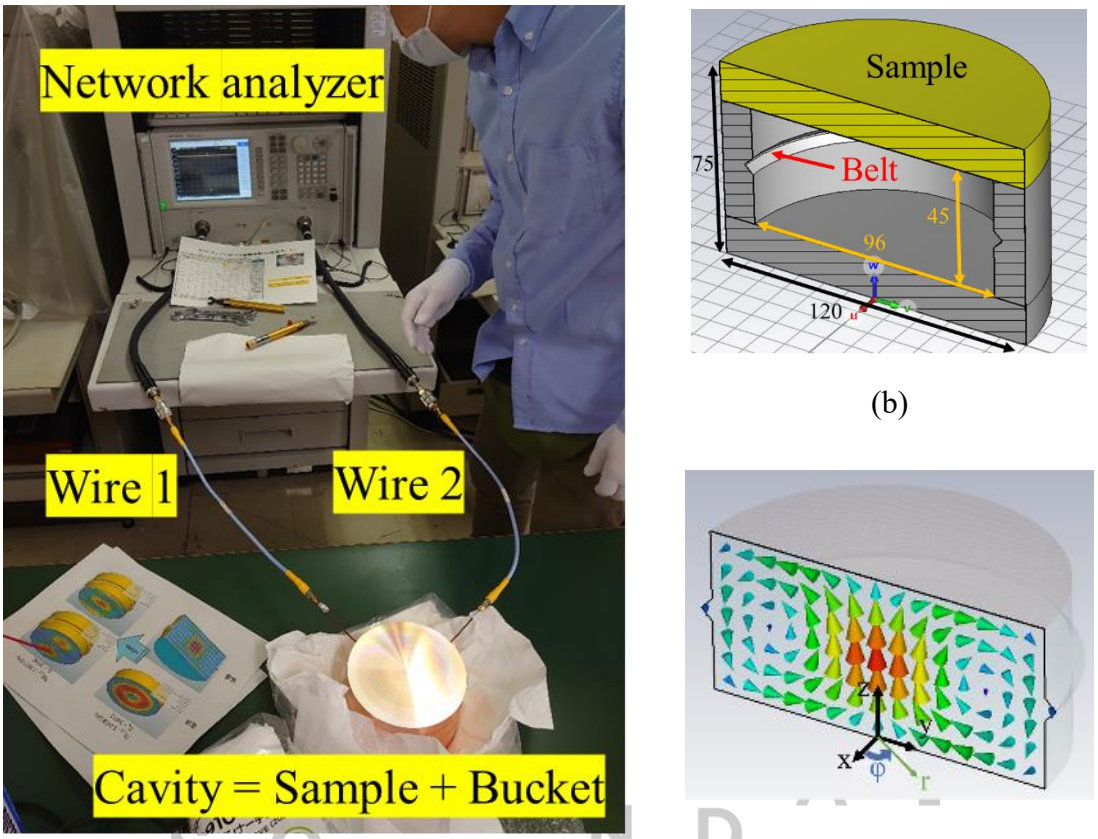

Figure 3-13: (a) Setup of cavity resonator method; (b) half-section view of the internally mirror-polished copper bucket with a circumferential "belt" (shallow groove) at the center of the cylindrical component; and (c) direction of the magnetic field under the TE011 mode in the CST simulation

First, by measuring the scattering parameter S_{21}, the loaded Q factor Q_L was obtained as

$$Q_L = \frac{f_0}{\Delta f(3dB)}, \qquad \text{(Eq. 3-23)}$$

where $f_0 = 5.044$ GHz, and $\Delta f(3\,dB)$ is the half-power bandwidth of the peak. To obtain the unloaded Q factor Q_0, we used

$$\frac{1}{Q_L} = \frac{1}{Q_0} + \frac{1}{Q_{c1}} + \frac{1}{Q_{c2}}, \qquad \text{(Eq. 3-24)}$$

where Q_{c1} and Q_{c2} are the coupling Q factors for Wires 1 and 2, respectively. The coupling coefficient β between the network analyzer and test cavity was defined as

$$\beta \equiv \frac{Q_0}{Q_c}, Q_0 = \beta Q_c. \qquad \text{(Eq. 3-25)}$$

Combining these two equations yields

$$Q_0 = Q_L(1 + \beta_1 + \beta_2). \quad \text{(Eq. 3-26)}$$

Under coupling conditions (i.e., $0 \leq \beta < 1$), we have

$$\beta = \frac{1 - |S_{11}|}{1 + |S_{11}|}, \quad \text{(Eq. 3-27)}$$

where parameter S_{11} (or Γ) is the reflection coefficient. After measuring S_{11} for Wires 1 and 2, the corresponding β is obtained and Q_0 can be calculated. For accurate measurement, β should be as small as possible, ideally between 0.001 and 0.01 (i.e., S_{11} should be as close to 1 as possible); this can be controlled by adjusting the insertion length of the signal wire.

In addition, we need to correct for the effects of temperature. From Ref. [46], Q_0 can be expressed as the ratio between the geometrical factor G (with dimensions of resistance) and the surface resistance R_S; thus,

$$Q_0 = \frac{G}{R_S} = (\text{if } f \text{ is fixed}) \frac{G\prime}{R}. \quad \text{(Eq. 3-28)}$$

In the case of a fixed frequency, the difference between R_S and the resistance R is only a constant multiple, so R_S can also be replaced by R. Next, from Ref. [47], we introduce the the temperature coefficient of resistance (TCR) to represent the resistance change factor per degree of temperature change:

$$TCR = \frac{dR}{dT}/R. \quad \text{(Eq. 3-29)}$$

The values of TRC are 3.93×10^{-3} [K^{-1}] for copper and 3.90×10^{-3} [K^{-1}] for aluminum, respectively [47-48]. Combining Eqs. (3-28) and (3-29), we can express the "temperature coefficient of Q_0" as

$$\frac{\frac{dQ_0}{dT}}{Q_0} = \frac{\frac{dRdQ_0}{dT\ dR}}{\frac{G\prime}{R}} = TCR \cdot \frac{R^2}{G\prime} \cdot \frac{dQ_0}{dR} = -TCR. \quad \text{(Eq. 3-30)}$$

Therefore, the measured Q_0 can be converted to a standard value at 20 °C:

$$Q_0(20°C) = Q_0[1 - (Temp.[°C] - 20)(TCR)]. \quad \text{(Eq. 3-31)}$$

An identical experiment was set up in the CST studio [49]. All the parameters of pure copper were known; hence, the conductivity (σ) of the sample surface could be adjusted until the Q_0 of the cavity matched the measured value; for this, we obtained the σ value of the sample surface at 5.044 GHz.

Finally, the intrinsic surface resistance R_S of a perfectly smooth metal surface under AC stimulation in the GHz regime can be calculated via [50]

$$R_S = \sqrt{\frac{\pi \mu_0 f}{\sigma}}, \quad \text{(Eq. 3-32)}$$

where μ_0 and f are the vacuum permeability and AC frequency, respectively. Although the surface of the T.S. coating was not smooth, its structure was considered under the material properties in the rough evaluation.

3.2.2.3 Dust

The dust generation rate was measured by Moresco Corp., Japan. The samples were first placed in 200 ml of isopropenyl acetate (IPA) to be ultrasonically cleaned for 5 minutes. Then, a HIAC 8011+ liquid particle counter was used to measure the number and sizes of particles in the solvent; the measurement principle of this device was derived from the light obscuration technique.

The number of particles with sizes of 4–100 μm was counted. The results were obtained (in units of particles /100 ml) and finally normalized by the coating area of the sample. The sample was ultrasonically cleaned once per measurement; hence, the same sample was measured five times, to observe the effects of cleaning upon dust reduction. In addition, the dust in the solvent was also collected using filter paper, and the components of the dust were measured via SEM with energy dispersive X-ray analysis (SEM-EDX).

SOKENDAI

3.2.2.4 Adhesive strength

We commissioned ICS Corp. to perform adhesive strength measurements. The adhesive strength measurement was in accordance with the *JIS H 8402: Test Methods of Tensile Adhesive Strength for Thermal-sprayed Coatings* regulations [51]. There were two substrates (Blocks A and B) per set of samples; these were cylinders with a diameter of 25 mm and a length of 51 mm. One end of Block A was coated, and one end of Block B was glass-bead-blasting (GBB) treated; the two sides were glued together with FM1000 glue, as shown in Fig 3-14(a).

The samples were installed on a tensile testing machine and the force was gradually increased until Blocks A and B became separated. The force at breaking point is referred to as the tensile breaking load P [N]. Figure 3-14(b) shows the tensile testing machine, and Fig. 3-14(c) shows the sample installation. The definition of tensile adhesive strength T [N/mm^2] was

$$T = \frac{P}{A}, \quad \text{(Eq. 3-33)}$$

where A is the coating area [mm^2]. According to *JIS H 8402*, the same sample must be measured at least three times. If the coating is still completely attached to Block A upon separation, it indicates that the adhesive strength of the coating exceeds that of the glue, which renders the measurement invalid.

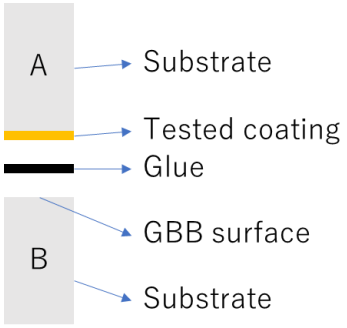

(a)

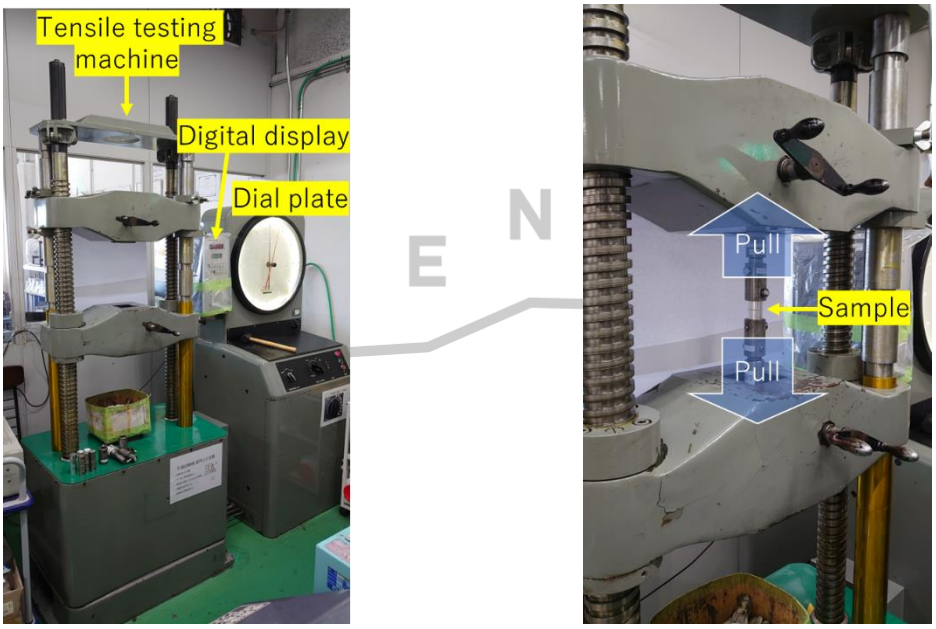

(b) (c)

Figure 3-14: (a) Schematic of the sample for adhesive strength measurement; (b) tensile testing machine; and (c) installation of sample on the machine

Chapter 4

Samples

4.1 Samples for SEY Property Studies

4.1.1 T.S.-coated Samples and their Spray Conditions

Before introducing the T.S.-coated samples, a brief introduction to the spray equipment is provided here. As shown in Fig. 4-1(a), thermal spraying was performed in a thermal spray room under an atmospheric environment. The main components of the process were a power supply, plasma-forming gas module, powder feeder, robotic arm control module, and spray gun (controlled by the robotic arm). The gas used to form the plasma contained 55 L/min of argon mixed with 8 L/min of hydrogen. The target thickness of the coating was 100 μm (≈ 10 rounds of spraying) because it has been found that a thickness exceeding 70 μm can ensure that the substrate surface is completely covered. A micrometer calliper was used to measure the differences in sample thickness before and after spraying, to obtain the coating thickness. Figure 4-1(b-c) shows the locations of the several air guns used to provide air cooling, including those positioned on the front and back sides and one mounted on the spray gun.

Table 4-1 shows the spray conditions and SEY properties of the T.S. coatings tested in the Master's report [31]. The substrate material was copper. Two sizes of copper powder were used to make the T.S. coating: Φ125–170 μm (denoted as “B”) and Φ45–50 μm (denoted as “S”). The SEY measurements showed that the value of δ_{max} for the surfaces produced by the smaller particles were generally lower. Furthermore, we tried to remove the H_2 from the plasma source, to reduce the plasma temperature (marked “LT”) and thereby maintain the bead shape of the copper powder. However, the δ_{max} of the LT-series samples did not reduce. Generally, before thermal spraying, the substrate should be roughened via GBB, to increase the adhesion between the coating and substrate. Certain T.S.-coated samples were produced via GBB pre-treatment (marked “GBB”) to test the effect of GBB

upon SEY properties. The results showed that the GBB had no clear effect on the SEYs of T.S. coatings.

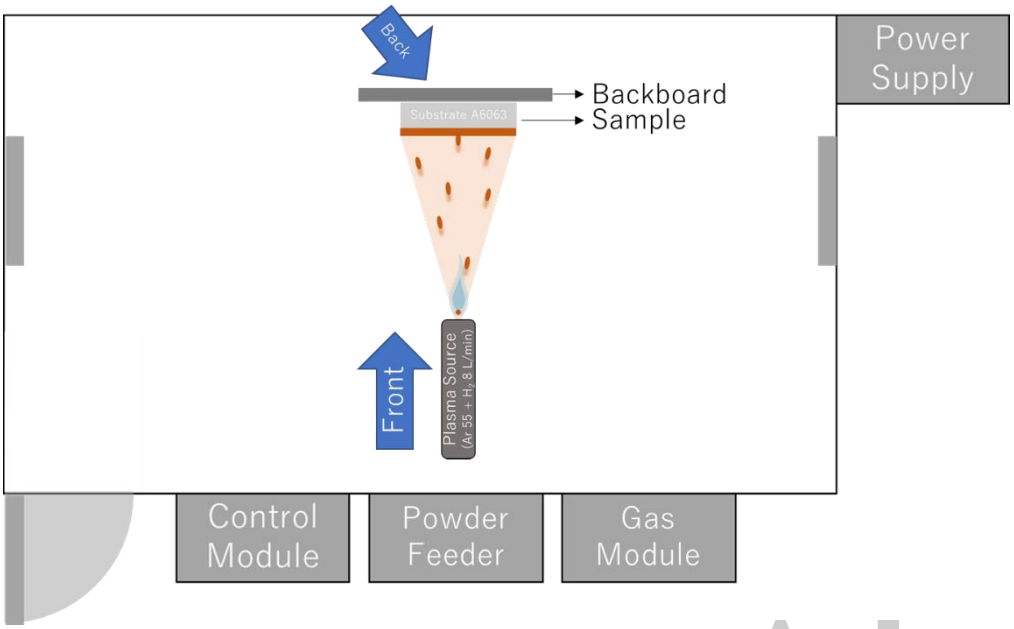

(a)

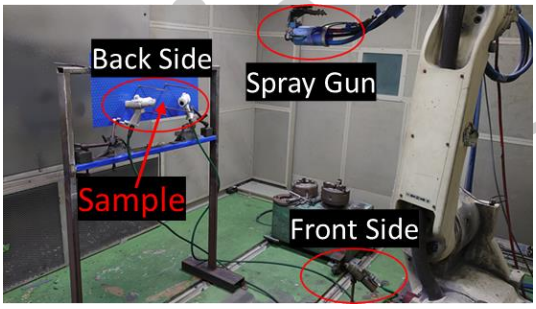

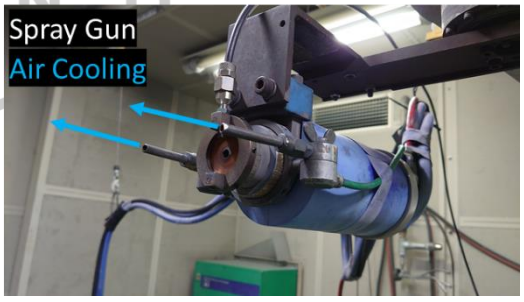

(b) (c)

Figure 4-1: (a) Schematic of the thermal spray room and equipment; (b) air guns located on front side, back side, and spray gun; and (c) close-up of the spray gun

Using the results from the Master's report [31], the samples in this study were improved from Sample S_STD (where "STD" denotes "standard"), which achieved the lowest δ_{max} in Table 4-1. The particle size of the 99.9% pure copper powder was chosen as Φ45–50 μm. Besides this, the material of the beam pipe in SuperKEKB LER was mostly aluminum; hence, in place of the copper considered in the previous report [31], we applied an aluminum (A6063) substrate and used GBB for pretreatment, to improve the adhesivity between dissimilar materials.

Table 4-1: Spray conditions and SEY properties of the T.S. coatings tested in the Master's report [31]

Sample	Substrate pre-treatment	Powder size (μm)	Coating thickness (μm)	Plasma-forming gas	δ_{max}	E_{max} (eV)
B_STD	Machined	Big	494	Ar + H_2	0.95	550
B_LT	Machined	(diameter:	26	Ar	1.10	450
B_GBB_LT	GBB	125–170)	20	Ar	1.15	600
S_STD	Machined	Small	494	Ar + H_2	0.96	650
S_LT	Machined	(diameter:	122	Ar	0.98	550
S_GBB_LT	GBB	45–50)	109	Ar	1.06	600

All T.S.-coated samples used in this study are listed in Table 4-2. The process of fabricating these samples can be divided into three major stages:

4.1.1.1 Stage 1

In the first stage, three test samples were fabricated under different conditions. The substrates had a diameter and thickness of 8 and 3 mm, respectively. The spray conditions of these three samples are listed in Table 4-2. The first sample A1_STD was fabricated under conditions similar to those of S_STD in the previous report [31]; however, a GBB aluminium substrate was used instead of the machined copper one. Sample Al_LT1 matched the previous spray condition of S_GBB_LT [31].

For Sample Al_LT2, we reduced the electric arc current relative to that of Al_LT1; thus, the power from the plasma should be further reduced. We maintained the bead shape to increase the complexity of the surface and try to further reduce the SEY. These substrates were sprayed onto the stainless steel (SS) plate with double-sided tape (DST). The samples at this stage were cooled by the back-side- and spray-gun-mounted air guns.

SCKENDAI

Table 4-2: Thermal spray conditions of all T.S.-coated samples

	Sample	Substrate	Backboard	Fixing Method	Coating thickness (μm)	Air-cooling	Maximum temperature (°C)	Note
	S_STD [31]	Machined Cu	SS plate	DST	208	Not recorded		
	S_GBB_LT [31]	GBB Cu	SS plate	DST		Not recorded		Cut H_2
Stage 1	Al_STD	GBB Al	SS plate	DST	84	Gun + back		Electric arc current: 500 A
	Al_LT1	GBB Al	SS plate	DST	108	Gun + back		Cut H_2, electric arc current: 500A
	Al_LT2	GBB Al	SS plate	DST	22	Gun + back		Cut H_2, electric arc current: 300A
Stage 2	OBP_H1–5	GBB Al	Al pipe	DST	47/94/164/171/101	Front + back		Horizontal spray
	OBP_S1–5	GBB Al	Al pipe	DST	77,92,101,97,77	Front + back		Sectorial spray
Stage 3	AC1_1–5	GBB Al	Al pipe	Screw	70,77,91,85,70	Front + back	72/107/86/-/-	
	AC2_1–5	GBB Al	Al pipe	Screw	59,73,92,84,69	Back	100/107/106/-/-	
	AC3_1–3	GBB Al	Al pipe	Screw	84,85,76	None	220/-/-	
	AC4_1	GBB Al	SS plate	DST	94	Gun + back	289	Same condition as Al-1
	AC4_2	GBB Al	SS plate	DST + screw	132	Gun	293	Spray gun round-trip distance: 370 mm
	AC5	GBB Al	SS plate	DST + screw	123	Gun + back	312	300 mm
	AC6	GBB Al	SS plate	DST + screw	146	Gun	371	300 mm
	BP-1–4	GBB Al			80–120	Front + back		Cut from beampipe

DST: double-sided tape

GBB: glass-bead blasting

SOKENDAI

4.1.1.2 Stage 2

Next, to consider the practical application of thermal spraying to an actual beam pipe, we establish here the method used to form a uniform coating along a curved inner wall.

To determine the proper method, ten aluminum substrates of the same size as Stage 1 were attached evenly via DST along the inner walls of two half-cut beam pipes used in SuperKEKB, as shown in Fig. 4-2(a) The thermal spraying was applied using two candidate methods, as shown in Fig. 4-2(b–c). Here, the spray condition matched that of the previous sample A1_STD, because its δ_{max} was lowest, as reported later. In Method 1, the spray gun sprayed in a fixed direction during scanning (called "horizontal spraying"), and the corresponding samples were OBP_H1–5 (OBP denotes "on the beam pipe"). For Method 2, the spray direction remained perpendicular to the inner wall ("sectorial spray"), and the corresponding samples were OBP_S1–5. The backboards of this batch of samples had curved surfaces; hence, to prevent air cooling from the spray gun affecting the direction of the copper droplets, the spray-gun-mounted air gun was turned off and replaced by the front-side air gun.

Method 2 should ideally produce an evenly distributed coating thickness. However, for Method 1, the coating thickness on either side should be thinner than that in the middle.

Therefore, in Method 1, we first coated the central sample (OBP_H3) to a thickness of 100 μm (11 rounds); then, we removed Samples OBP_H 1–2 and coated the sample on the side (OBP_H5) to a thickness of 100 μm (20 rounds).

In Method 2, because the coating thickness was more uniform, we only sprayed 10 rounds to coat the central sample (OBP_S3) to a thickness of 100 μm.

4.1.1.3 Stage 3

As shown in the Results, the SEY profiles of Samples S_STD [31], Al_STD, and the OBP series were measured. These samples had similar spray conditions (i.e., the same copper powder and plasma); however, their δ_{max} and E_{max} values were observed to differ, because of the different substrates and backboards. This difference was suspected to be attributable to the difference in surface temperatures during spraying.

To confirm the surface temperature during spraying, we designed an aluminum substrate that could be connected to a thermocouple. The substrates had diameters and thicknesses

of 15 and 3 mm after assembly, respectively. The samples with recorded temperatures in Table 4-2 denote the samples whose temperature could be measured by thermocouples; the other unmarked samples denote ordinary block samples of the same size.

(a)

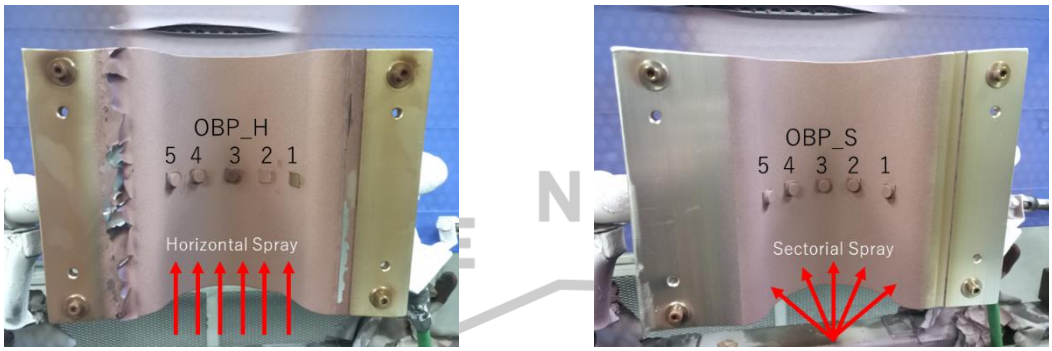

(b) (c)

Figure 4-2: (a) OBP series substrates attached on a half-cut aluminum pipe; (b) sketch of the spray direction for Method 1 (horizontal spray) and OBP_H1–5; and (c) sketch of the spray direction for Method 2 (sectorial spray) and OBP_S1–5

Instead of DST, we used screws to fix the substrates on the beam pipe, to bring the measured temperature closer to the actual value of the beam pipe and prevent the samples falling off at high temperature.

To control the surface temperature during spraying, we set four different air-cooling conditions. The first condition was to turn on the front and back air guns [in fact, this was the same as the OBP_S setting, except that the substrates were fixed with screws and the corresponding samples were AC1_1–5 (AC denotes air cooling)]. The second was to turn on only the back air gun, and the third was to turn off all air guns. The corresponding samples were AC2_1–5 and AC3_1–3, respectively. To reproduce Al_STD, the fourth

condition applied the same conditions as Al_STD, and the corresponding sample was denoted as AC4_1. Then, to obtain a higher temperature than AC4_1, we adjusted the round-trip distance of the spray gun and air cooling, to obtain Samples AC4–2, AC5, and AC6.

AC4_2 was a reproduction of AC4_1. The fixing method was DST + screw; this reduced heat dissipation whilst ensuring that the sample was tightly fixed. In essence, the surface temperature of the sample gradually increased in proportion to the number of air-cooling conditions, and the range was ~70–370 °C. The abovementioned air-cooling conditions and sample installations can be more readily understood by referring to Fig. 4-3.

Finally, the spray conditions of AC1 were taken as the final conditions to produce the real T.S.-coated beam pipe, and the samples cut from the excess part of this beam pipe were labeled BP-1–4.

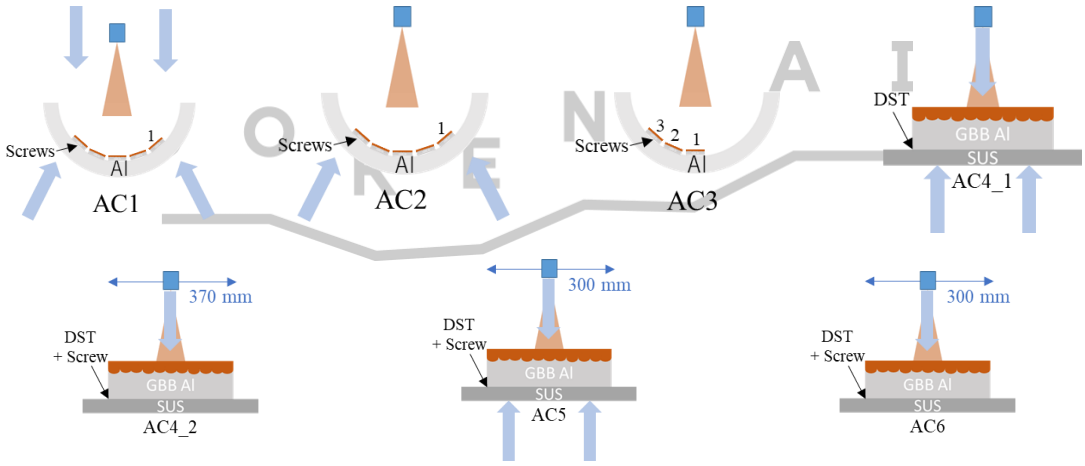

Figure 4-3: Schematic of air-cooling conditions for Samples AC1–6

4.1.2 Samples to Investigate the Relationship between Roughness and SEY

To investigate the relationship between roughness and SEY properties, we fabricated some samples with triangular grooves featuring tip angles α of 20, 30, and 60°. The substrate consisted of disc-shaped oxygen-free copper of diameter 15 mm and thickness 5.5 mm. The depth of the groove was fixed at 1.88 mm. The detailed dimensions of these samples are shown in Fig. 4-4.

Due to machining constraints, the peaks and valleys of the grooves featured arcs of radius 0.05 mm. The diameter of the primary electron beam for SEY measurement is comparable

to the distance between the groove peaks; hence, to avoid errors in the SEY measurement of the groove samples, we fabricated four samples for each angle, with shifts corresponding to 0, 0.3, 0.5, and 0.7 groove periods, respectively (see the table in Fig. 4-4). The SEY results of the four samples were averaged as the final SEY of the groove at that angle.

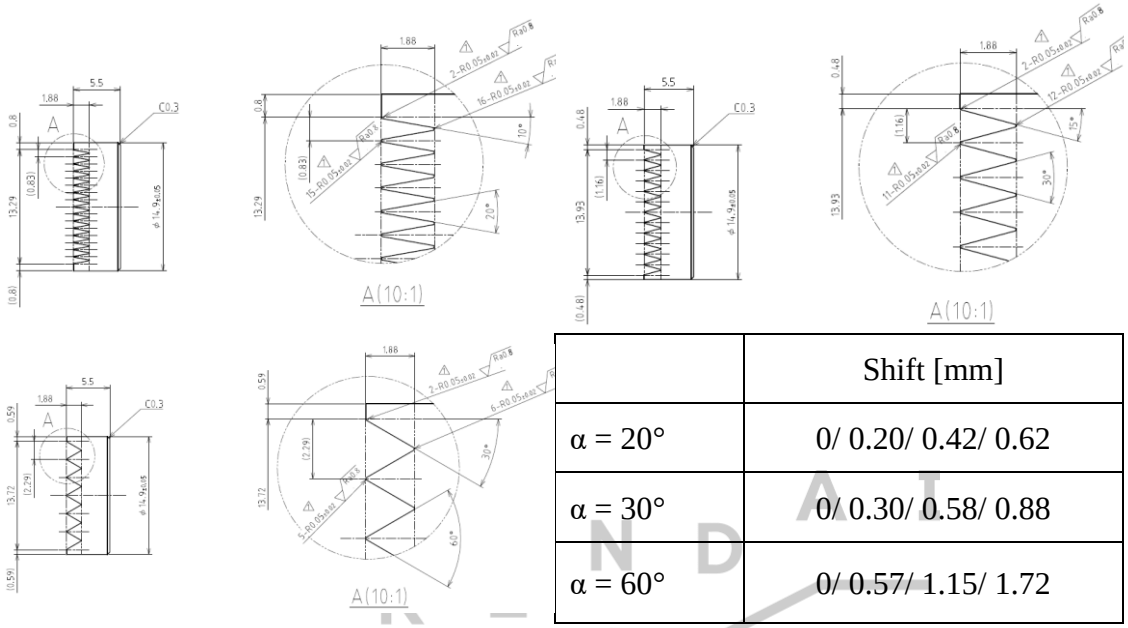

	Shift [mm]
α = 20°	0/ 0.20/ 0.42/ 0.62
α = 30°	0/ 0.30/ 0.58/ 0.88
α = 60°	0/ 0.57/ 1.15/ 1.72

Figure 4-4: Design drawing of triangular groove samples with tip angles α of 20°, 30°, and 60°

4.1.3 Other Samples: Copper Oxides and TiN

In the Master's report [31], it was stated that the main component of the T.S.-coated surface after conditioning was Cu_2O; hence, we tried to make a pure Cu_2O or CuO sample, to obtain more basic data for discussion. According to Ref. [52], the CuO and Cu_2O surfaces can be obtained by heating copper to 400 and 200 °C, respectively, under atmospheric conditions. Thus, we used the muffle furnace to heat three disc-shaped copper samples of diameter 15 mm and thickness 5 mm to 400 °C for periods of 7, 20, and 120 minutes, respectively. In addition, one sample was heated to 200 °C for 2 h using a heating plate. The appearances of these samples are shown in Fig. 4-5. CuO was black and Cu_2O was reddish-brown. It was found that the black CuO formed by heating to 400 °C peeled off easily in flakes. In Fig. 4-5(c), we see that the surface had begun to peel off, and the black oxide layer on the surface of the sample in Fig. 4-5(d) could be easily peeled off to obtain the state in Fig. 4-5(e).

After measuring their surface compositions via XPS, it was determined that only the sample in Fig. 4-5(e) was pure Cu_2O; the rest of the sample surfaces were a mixture of CuO and Cu_2O. In short, we successfully fabricated a sample of the pure Cu_2O surface to be used as basic data for SEY; however, we could not make a flat surface of pure CuO because it was easily peeled off from the sample. SEY measurements were performed for three samples that did not exhibit surface peeling: Cu_2O, Mix_1, and Mix_2 (as shown in Fig. 4-5).

Finally, we obtained a disk-shaped TiN-coated aluminum sample of diameter 15 mm and thickness 5 mm, with a coating thickness of ~200 nm. The production method matched that used for TiN coating in SuperKEKB (see [53] for the detailed production process).The measurement results of SEY vary for different apparatuses; hence, to obtain a good basis for comparison, we measured the SEY of TiN using our own.

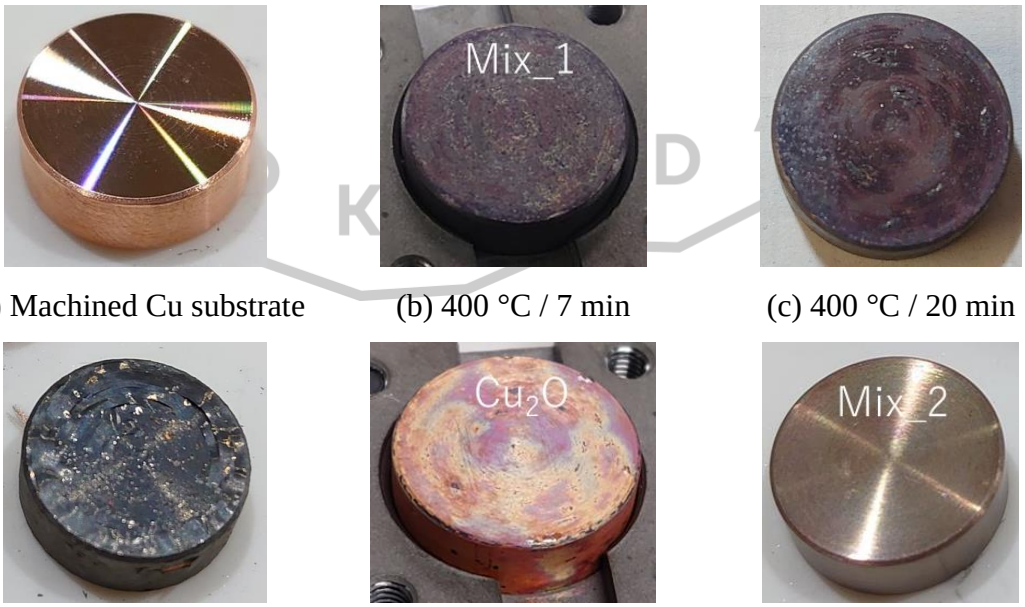

(a) Machined Cu substrate (b) 400 °C / 7 min (c) 400 °C / 20 min

(d) 400 °C / 2 h (e) 400 °C / 2 h / pulled off (f) 200 °C / 2 h

Figure 4-5: Appearance of various copper oxide trial samples

4.2 Samples for SEM Imaging, Roughness Measurements, and XPS Analysis

The samples for SEM imaging, roughness measurements, and XPS analyses were all selected from the SEY measurement samples (see Table 4-2). The measurements for each sample are listed in Table 4-3.

First, amongst the samples for SEY measurement, SEM images were taken for almost all samples, except for some AC series and BP series ones. Samples in the center of AC1–4 and BP-1 were selected for cross-section polishing (CP) or ion milling, to observe the cross-section structure of the coating. The CP method was applied to embed the sample into the resin, cut and grind it mechanically, and smooth the section via argon ions to facilitate observation and mitigate the damage caused by mechanical grinding. The cross-section structures for these samples were observed via SEM (Qualtec Co., Ltd) using a magnification of 500.

The roughness parameters were measured for almost all samples, except for those samples that had been resin-coated using the CP method.

SOKENDAI

In the XPS analysis, we initially only measured the surface composition after conditioning (i.e., after SEY measurements). However, in later stages, we wanted to know the difference in surface composition before and after conditioning. Therefore, AC1–4 and BP series samples were selected for surface composition analysis before conditioning (i.e., as-received). However, experimental scheduling meant that the XPS analyses were performed by two different institutions. The parts marked with an asterisk in Table 4-3 were performed by the Industrial Technology Innovation Center of Ibaraki Prefecture; the remainder were performed by the Industrial Technology Center of Yamanashi Prefecture. Again, because of the experimental scheduling, AC4_1 was selected to measure the depth profile.

Table 4-3: List of measurements taken for each sample

	SEM	CP	Roughness measurement	XPS before conditioning	XPS after conditioning	XPS depth profile
S_STD [31]	✓		✓		✓	
S_GBB_LT [31]	✓		✓		✓	
Al_STD	✓		✓		✓	
Al_LT1	✓		✓		✓	
Al_LT2	✓		✓		✓	
OBP_H1~5	✓		✓		✓	
OBP_S1~5	✓		✓		✓	
AC1_1~5	1, 3	3	1, 2, 4, 5	1*, 3*	1, 3	
AC2_1~5	1, 3	3	1, 2, 4, 5	1*, 3*	1, 3	
AC3_1~3	1, 3	1	2, 3	1*	1	
AC4_1	✓	✓		✓*	✓*	✓*
AC4_2	✓		✓			
AC5	✓		✓			
AC6	✓		✓			
BP-1~4	1, 3	1	2, 3, 4	1*, 3*	1, 3	

CP: cross-section polishing or ion milling

* denotes the XPS measurements performed by the Industrial Technology Innovation Center of Ibaraki Prefecture; all others were performed by the Industrial Technology Center of Yamanashi Prefecture.

SOKENDAI

4.3 Samples for Feasibility Studies in Accelerators

4.3.1 Beam Pipe with T.S. Coating

To measure the effect of the T.S. coatings for reducing ECs in SuperKEKB, it was necessary to fabricate a real beam pipe applying the coating. The structure of the beam pipe was essentially the same as in Fig. 1-3. The design drawing and cross-sectional view are shown in Figs. 4-6 and 4-7, respectively (unit: mm).

The spray conditions were the same as those of AC1 in Table 4-2. The target length of the beam pipe after assembly was 1200 mm. The manufacturing process was as follows. First, because the spray gun could not extend into the beam pipe, a 1200 mm-long extruded pipe was divided into four parts: upper and lower parts and two water-cooling channels (as shown in Fig. 4-7). Second, the upper and lower parts were sprayed (Fig. 4-8). Third, the lengths of these two parts were shortened, to provide some space for the flange (the above-mentioned samples BP-1–4 in Table 4-2 were cut from this part); the parts were then welded together using the cooling water channels cut from another extruded pipe (Fig. 4-9). Finally, a screen was installed to isolate the NEGSs from the beam channel, flanges at either end were welded, a hole was cut out, and a port (for the electron monitor) was welded to the hole (see Section 4.8.3). Notably, the aluminum mesh screen in front of the electron monitor was left uncoated by mistake. The high δ_{max} ($\approx$ 2) [31] for aluminum increased the electron density measured for this beam pipe, which resulted from the coupling between the T.S. coating and aluminum. We discuss these effects in detail in the next chapter.

The current process requires the beam pipe to be cut before spraying; this may not be conducive to mass production. However, the novelty of this study is that it proposes a T.S. coating for reducing ECs. If thermal spraying is considered for large-scale application in the future, we recommend a 90° spray gun with a slender robotic arm to allow it to enter the beam pipe for direct spraying.

The T.S.-coated beam pipe was installed in an arc section of LER in SupereKEKB, in July 2021. The replacement was a pure copper beam pipe of the same structure; it had been tested as a reference. Meanwhile, three other aluminum beam pipes were used (i.e., TiN coating, groove structure, and a combination thereof); these were installed earlier in the ring for reference. Table 4-4 summarizes the beam pipes corresponding to each electron monitor at different time periods.

SOKENDAI

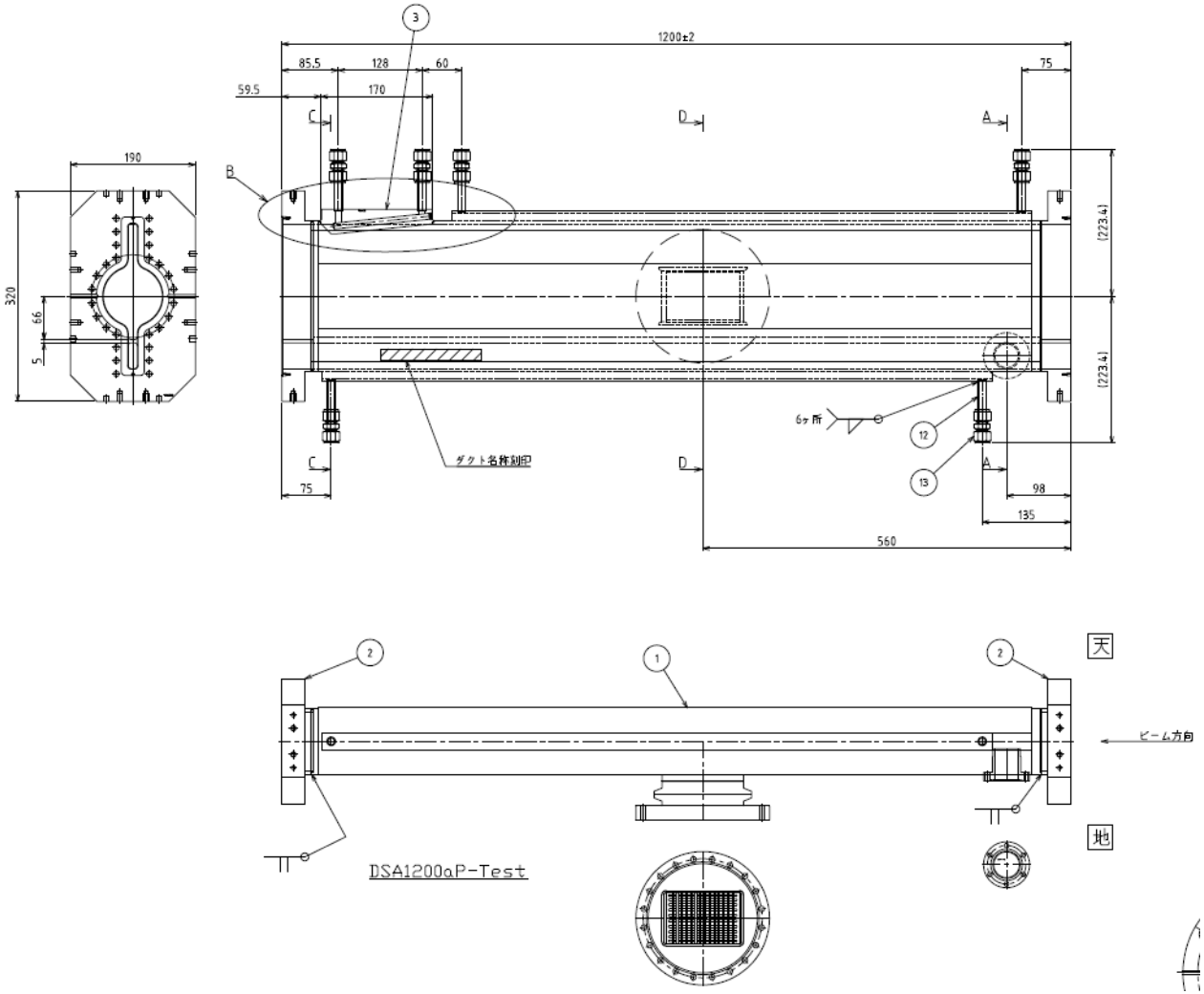

Figure 4-6: Design drawing of T.S.-coated beam pipe

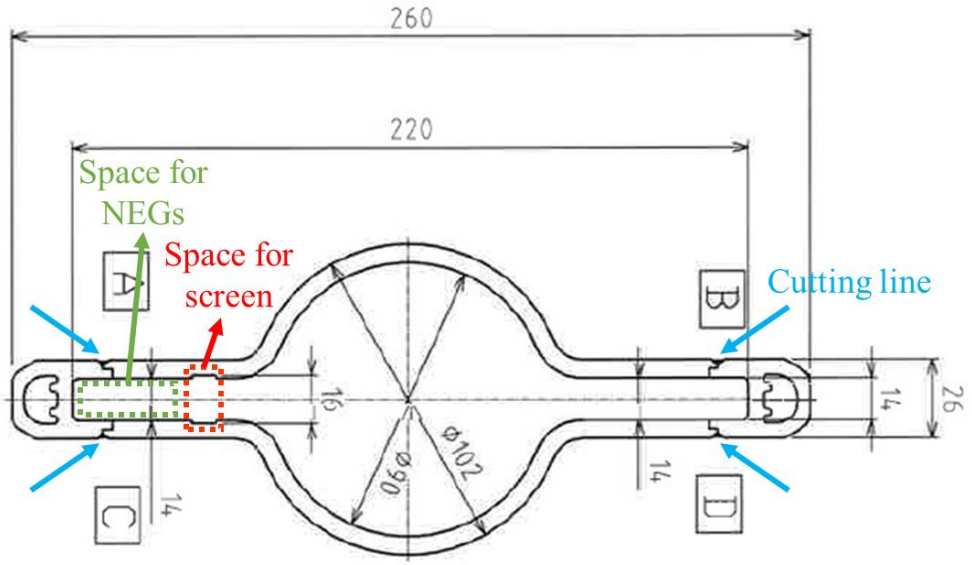

Figure 4-7: Cross-sectional dimensions of the beam pipe and position of the cutting line

Figure 4-8: Half-cut beam pipe after spraying

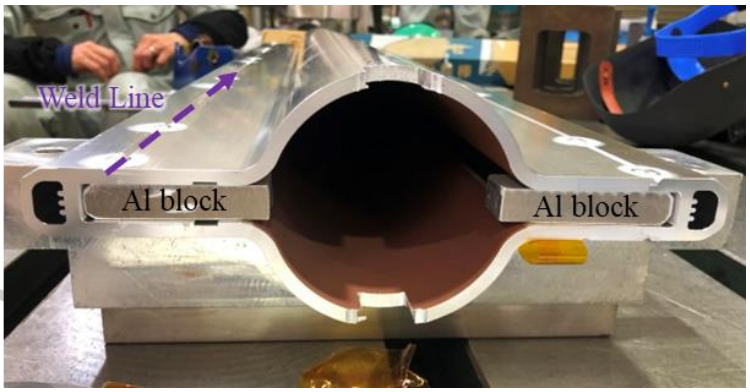

Figure 4-9: Beam pipe during welding. The aluminum blocks were applied to prevent deformation of the beam pipe during welding

Table 4-4: Beam pipes corresponding to each electron monitor at different time periods

	Monitor 1	Monitor 2	Monitor 3	Monitor 4
2020/03–2020/07	TiN	TiN	TiN groove	Al groove
2020/07–2021/07	TiN	Cu	TiN groove	Al groove
2021/07–Now	TiN	T.S. coating	TiN groove	Al groove

4.3.2 Appendix: Details of T.S.-coated Beam Pipe Production

Here follows some observations made whilst fabricating the T.S.-coated beam pipe, to be used for future improvements.

4.3.2.1 Coating edge control

The first attempt to spray directly onto the half-cut beam pipe is shown in Fig. 4-10(a). The coating accumulated on the edge of the fixture was easy to peel off, as shown in Fig. 4-10(b) and (c). Therefore, the coating range was narrowed and some of the clean GBB surface was retained to prevent dust. We added two stainless-steel baffles at the junctions of the fixture and pipe, which made it easier to control the spray range [as shown in Fig. 4-10(d) and (e)]. After this improvement, we obtained a strong coating with clean edges, as shown in Fig. 4-10(f).

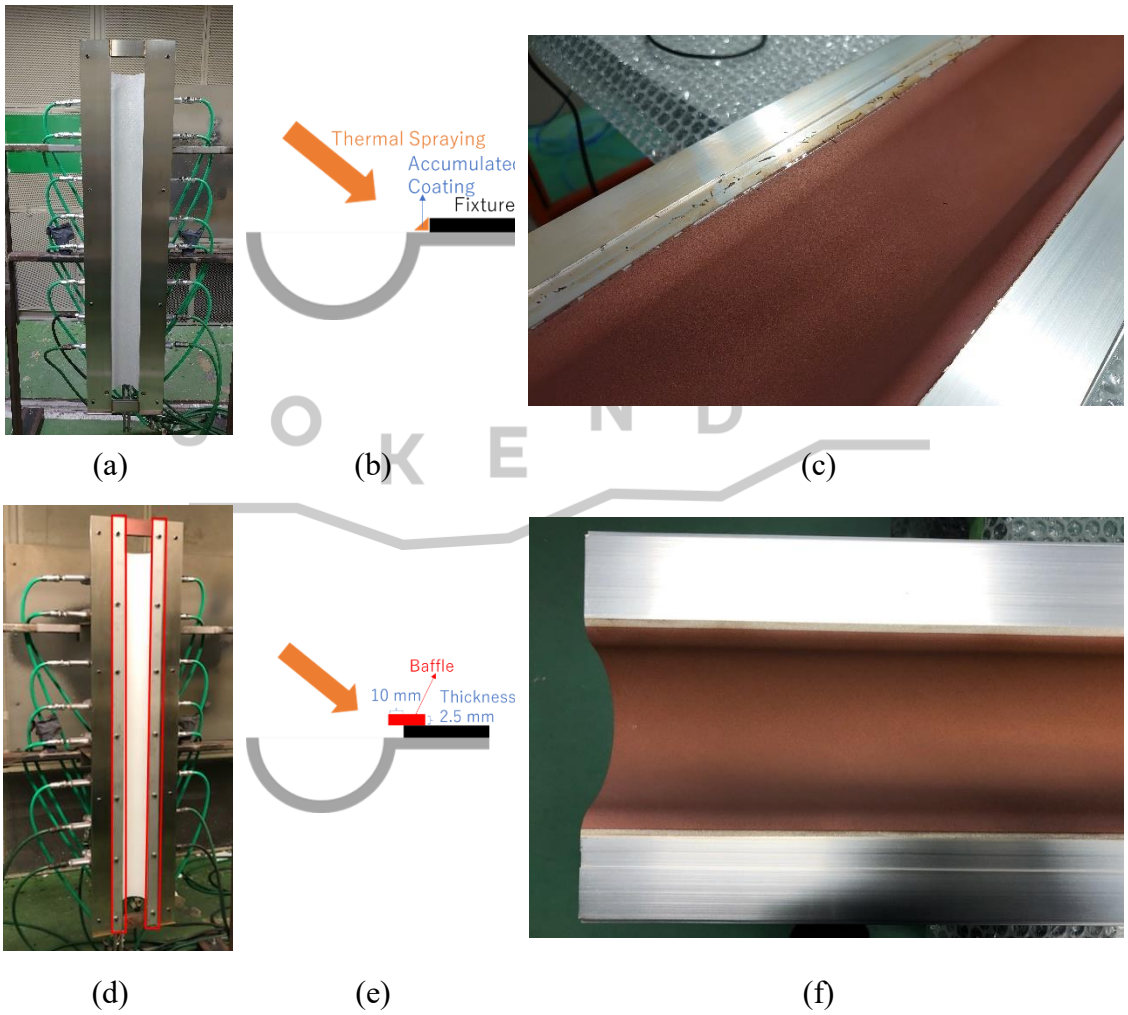

Figure 4-10: (a) Setting of the first thermal spraying on the long half-cut beam pipe; (b) schematic of the accumulated coating between the fixture and pipe; (c) accumulated coating peeling off and forming dust; (d) setting after the installation of two stainless-steel baffles; (e) schematic of the baffles; and (f) coating with well-controlled edges

4.3.2.2 Oxidation of the coating during welding

We found that the high temperature produced by tungsten inert gas welding discolored the surrounding thermal spray coating, as shown in Fig. 4-11. The effects of discolored parts should be evaluated in future.

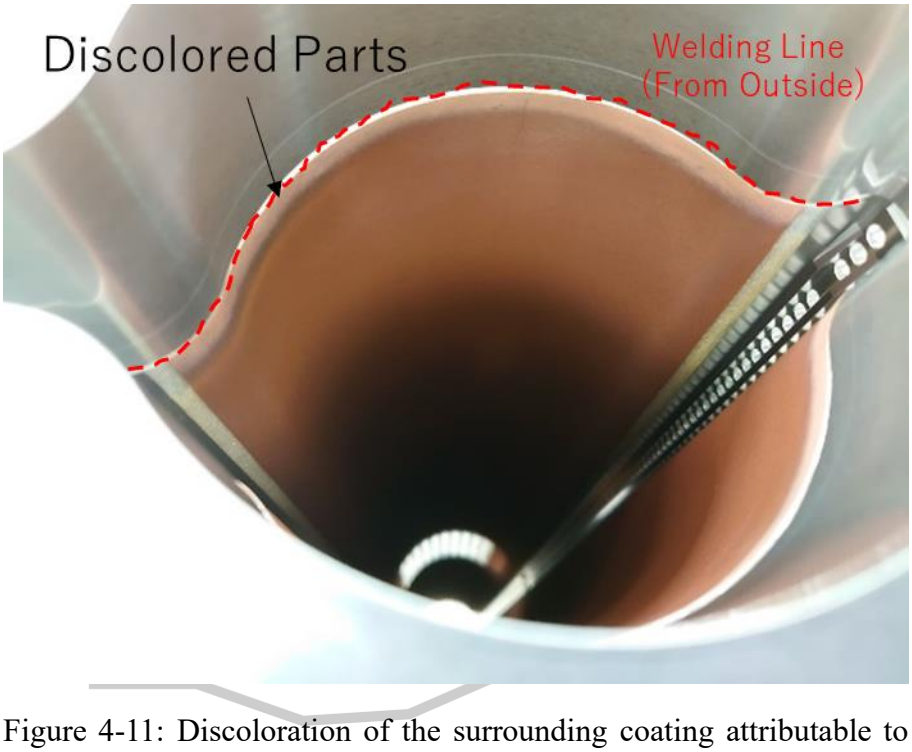

Figure 4-11: Discoloration of the surrounding coating attributable to high temperatures during welding

4.3.2.3 Sequence of cutting and spraying

This time, the pipe was sprayed first, and the hole for the electron monitor was then cut out and the port welded on. If the spray step can be adjusted after cutting and welding, it may be possible to reduce the amount of peeling caused by cutting, as well as the discoloration during welding.

4.3.3 Samples for Outgassing Rate Measurement

Four types of samples were prepared for outgassing rate measurements. The first type was an aluminum sample with a machined surface; the others had a T.S. coating on both sides, obtained under spray conditions matching those of Al_STD, Al_LT1, and Al_LT2 in Table 4-2.

Five pieces of each type of sample were used; these each had a size of 100 × 100 × 3 mm^3

and contained four Φ5 mm holes for fixing during spraying, as indicated in Fig. 4-12. The total surface area and coated surface area of the five pieces were 1.06×10^5 mm^2 and 9.80×10^4 mm^2, respectively.

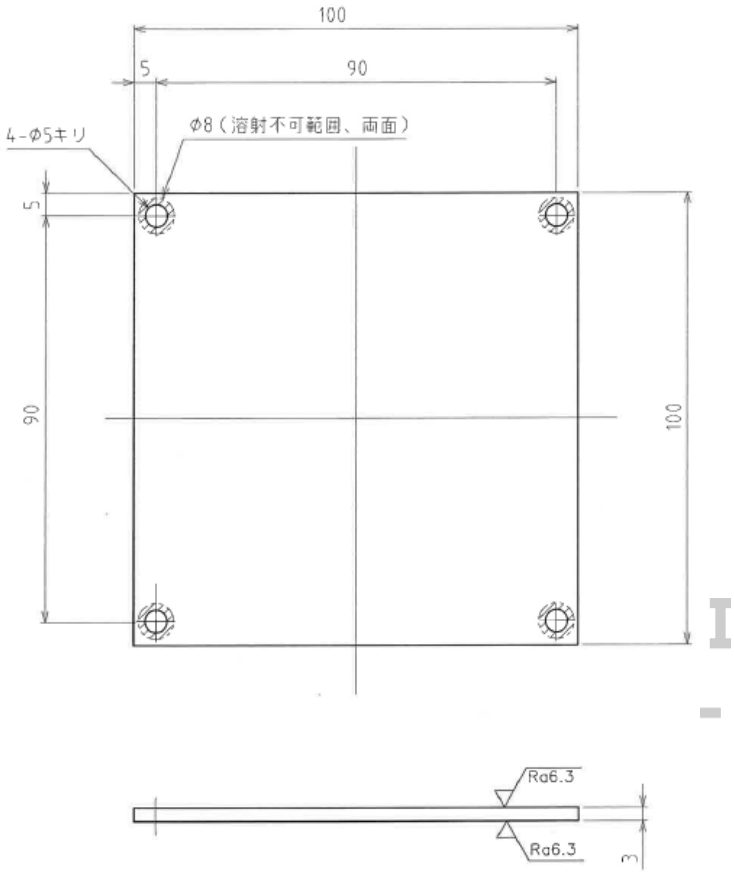

Figure 4-12: Design drawing of the sample used to measure the outgassing rate

4.3.4 Samples for Dust Measurement

The samples used to measure dust generation shared the same substrate as those for the outgassing rate measurements; however, the sprayed area was reduced, to avoid an incomplete coating that was easy to peel off on the sides of the substrate or near the screws, as indicated in Fig. 4-13. The square sprayed surface of one sample was 7225 mm^2.

The spray conditions matched those of Sample AC1_1–5 (see Table 4-2) (i.e., the condition finally adopted to make the real beam pipe). We fabricated two samples, one as-received and the other cleaned with compressed air. We also tested two commercial NEG strips (St 707) installed in the antechamber of SuperKEKB [5] as a reference, with a total coating area of 9720 mm^2. The dust was measured five and three times for the thermal spray samples and NEG strips, respectively.

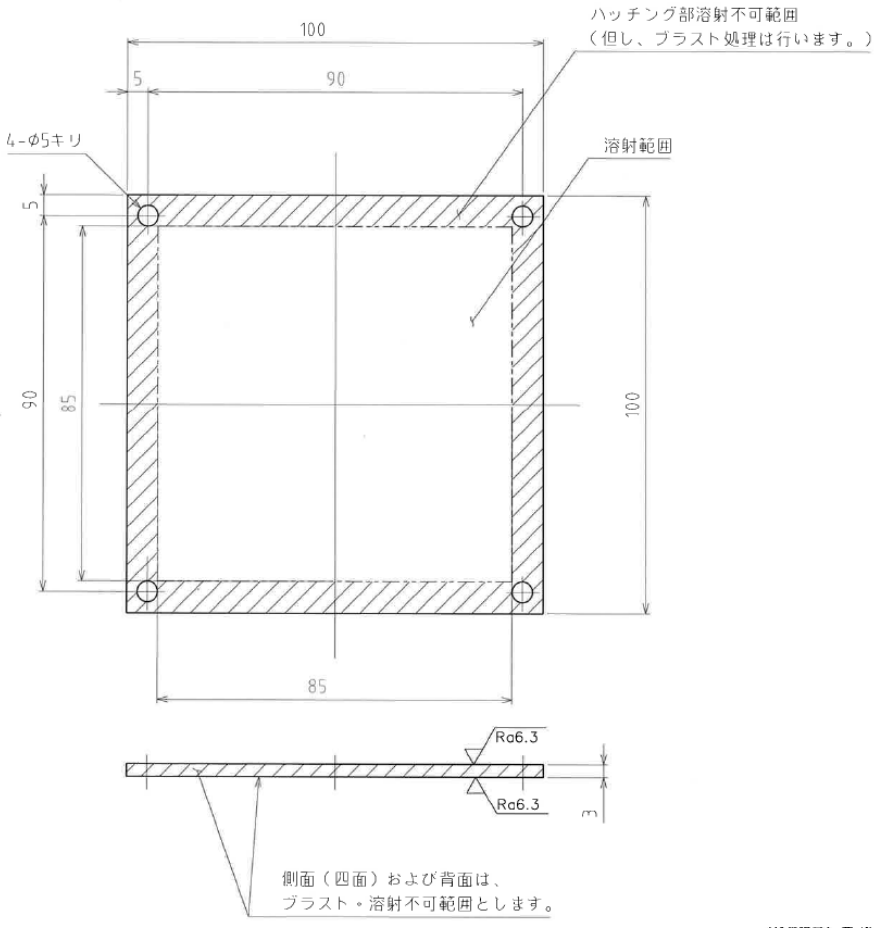

Figure 4-13: Design drawing of the dust measurement sample

4.3.5 Samples for Surface Resistance Measurement

Four surfaces were prepared to measure surface resistance in the microwave regime. The disc-shaped substrate was 120 mm in diameter and 15 mm in thickness. The surface to be measured consisted of a circle of 96 mm center diameter; the remaining outer ring component needed to be ground to a roughness *Ra* of less than 1 μm, to ensure tight contact with the copper cavity.

The first surface was mirror polished (*Ra* = 1.0 μm) on the copper substrate as a standard for comparison, as shown in Fig. 4-14(a). The second and third surfaces were machine-ground and GBB-treated aluminum surfaces, respectively, on the front and back of the same aluminum substrate, as shown in Fig. 4-14(b) and (c). The fourth surface was the T.S. coating, which used the same spray conditions as AC1 in Table 4-2 [as shown in Fig. 4-14(d)].

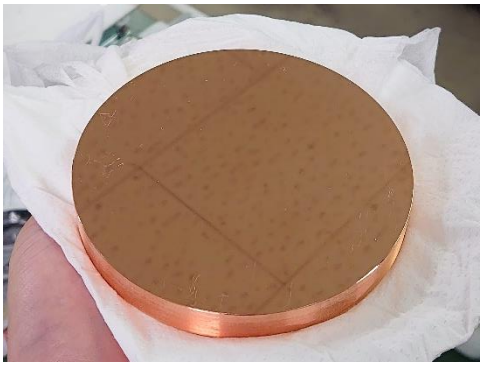

(a) Polished surface on copper substrate

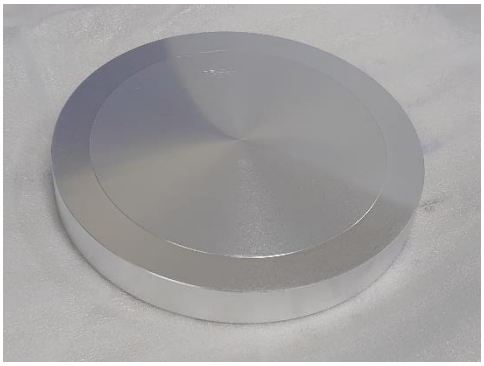

(b) Machine-ground surfaces on aluminum substrate

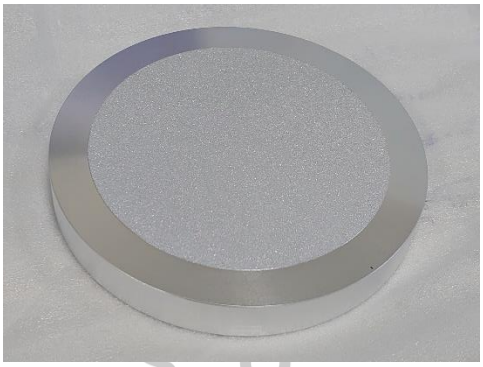

(c) GBB-treated surfaces on aluminum substrate

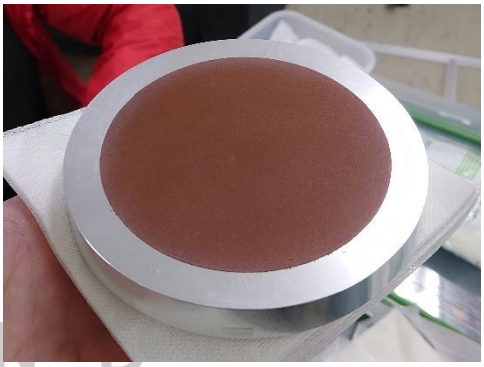

(d) T.S. coating on aluminum substrate

Figure 4-14: Samples for Q-factor measurement

4.3.6 Samples for Adhesive Strength Measurement

We fabricated two kinds of samples to measure the adhesive strength of the T.S. coating. The first was a T.S. coating on aluminum (A6063), and the spray conditions matched those of AC1 (see Table 4-2); the second was copper electroplating on structural steel (SS400), where SS400 was used as a cheap alternative to stainless steel. Different types of coating should adopt different methods when evaluating their coating strengths; however, to provide a reference for the T.S. coating, we used the same method to test the electroplated copper coating. The coating thickness must be at least 300 μm (according to the *JIS H 8402* regulations); hence, the thicknesses of the T.S. and electroplating coatings were ~300 μm and 450 μm, respectively. Three sets of samples were made for each coating, to comply with the minimum number of tests specified in *JIS H 8402*. Figure 4-15 shows the samples used for coating strength measurements, where two pieces were already glued (see Section 3.1.8). The front row contains the copper electroplating samples; the back row shows the thermal spray samples.

Figure 4-15: Samples for adhesive strength measurement

SOKENDAI

Chapter 5

Results and Discussion

5.1 SEY Properties

5.1.1 SEY Properties of T.S.-coated Samples

Figure 5-1 shows the SEY(δ) profiles with respect to the energy of the primary electron (E_p) for all samples described in Section 4.1 after conditioning. Except for the three samples in the Master's report (Cu flat, S_STD, and S_GBB_LT in Table 4-2), whose conditioning time was 48 h (electron dose $\approx 6 \times 10^{-2}$ C/mm^2), the conditioning time of the samples in this study was 72 h (electron dose $\approx 1 \times 10^{-1}$ C/mm^2). The δ_{max} of any T.S.-coated sample was smaller than that of the flat copper surface, and its corresponding E_{max} was also higher.

SOKENDAI

Figure 5-2 shows the δ_{max} of all samples as a function of the electron dose. The δ_{max} of certain thermal spray samples slowly increased with conditioning time. This phenomenon was also noted in the Master's report [31]; however, its mechanism has not been clarified yet. When the backboard for thermal spraying was replaced with the half-cut beam pipe, the δ_{max} was almost below 0.8. It should be noted that only Fig. 5-2 (a) and (i) use different scales on the vertical axis.

However, δ_{max} does not contain all the information regarding the SEY of a surface. The corresponding E_{max} is also important. Therefore, the δ_{max} and E_{max} of each sample are listed in Table 5-1. In Table 4-2, we find that for the samples fabricated using sectorial spraying (i.e., OBP_S and AC1–3), the coating thickness was more uniform than that of horizontal spraying; however, some difference remained in the coating thickness at different positions. This implies that the spray directions at different positions were not completely perpendicular to the surface. In thermal spraying, molten metal droplets impinge on a surface and rapidly solidify. If the spray direction is different, the surface

structure after solidification will differ, resulting in a different SEY profile. From the results for the TS1–3 series samples in Table 5-1, we find that the samples at the edge of the beam pipe are prone to exhibit different E_{max} or δ_{max} between samples in the same group. Room for improvement remains in the robotic arm manipulation.

It is not known from which part of the beam pipe each BP-series sample was cut. However, from the E_{max} results, BP-2 was determined as most likely to be from the edge of the beam pipe. Fortunately, the δ_{max} values for all samples were low enough that the difference in E_{max} became less important.

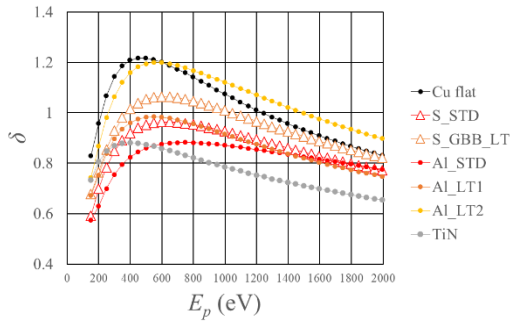

(a)

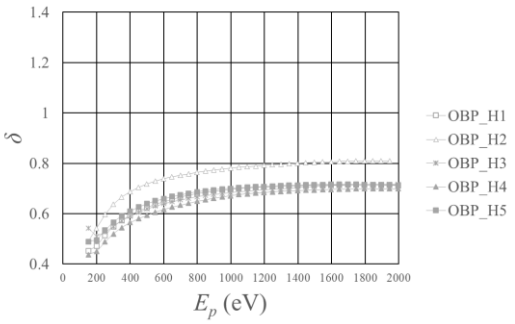

(b)

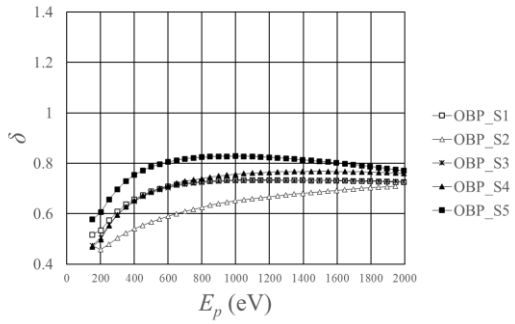

(c)

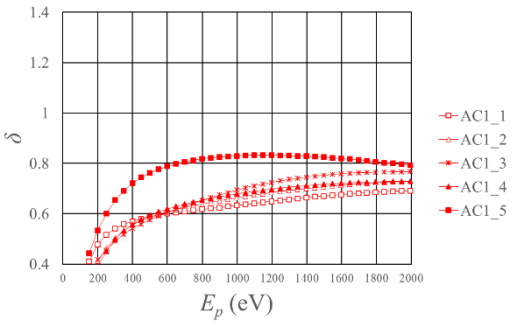

(d)

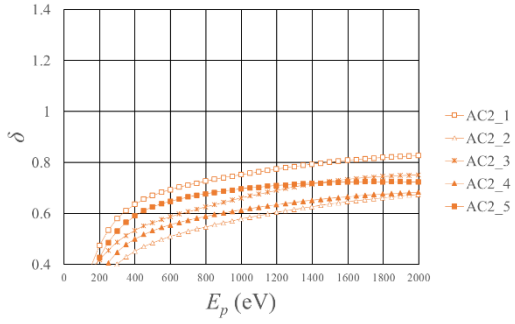

(e)

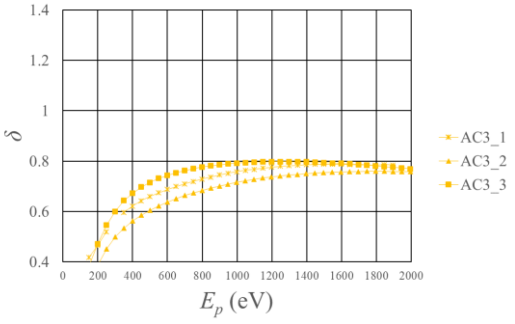

(f)

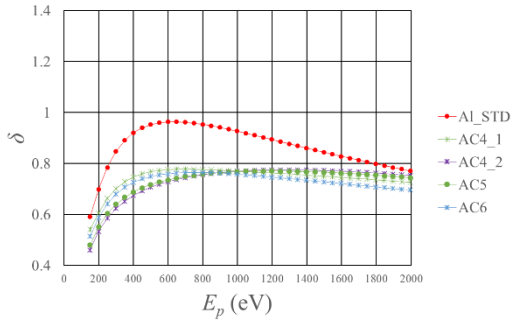

(g)

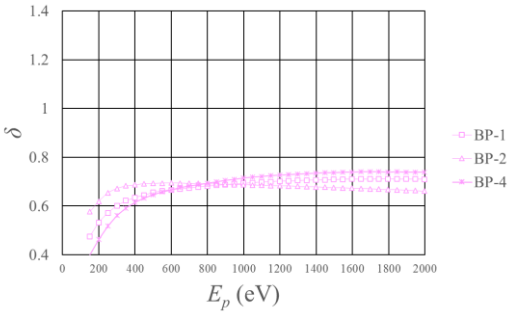

(h)

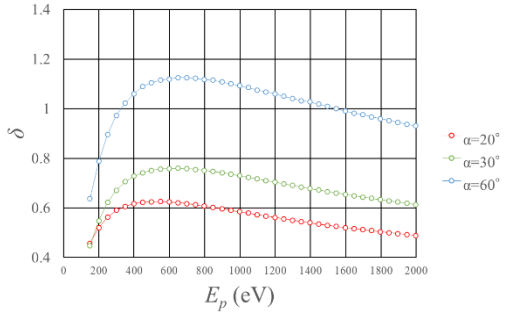

(i)

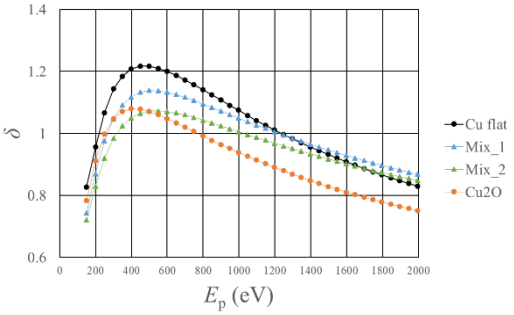

(j)

Figure 5-1: δ profiles with respect to E_p for all samples after conditioning

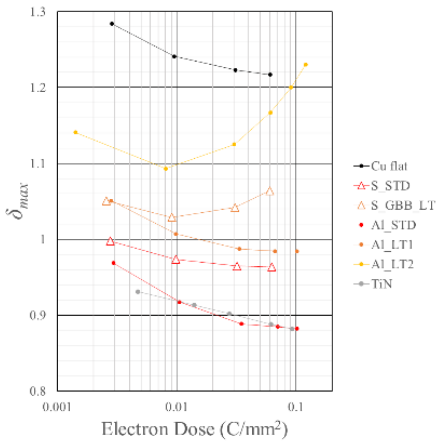

(a)

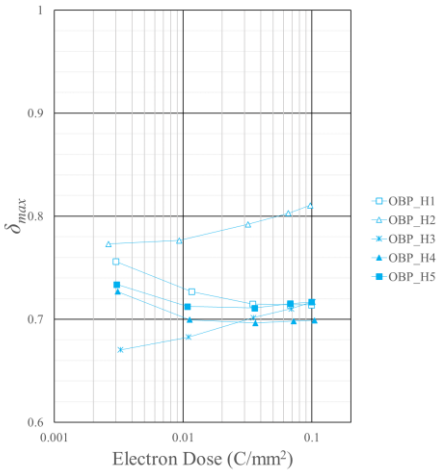

(b)

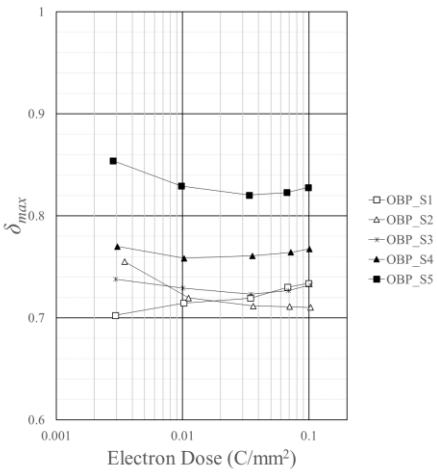
1
0.9
0.8
0.7
0.6
δ_{max}
0.001
0.01
0.1
Electron Dose (C/mm²)
OBP_S1
OBP_S2
OBP_S3
OBP_S4
OBP_S5

(c)

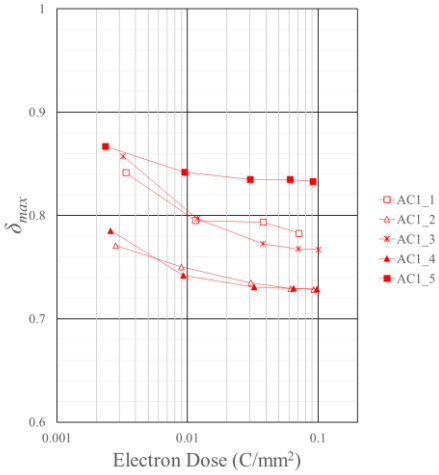
1
0.9
0.8
0.7
0.6
δ_{max}
0.001
0.01
0.1
Electron Dose (C/mm²)
AC1_1
AC1_2
AC1_3
AC1_4
AC1_5

(d)

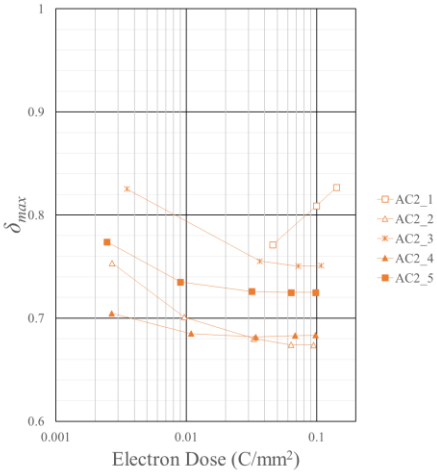
1
0.9
0.8
0.7
0.6
δ_{max}
0.001
0.01
0.1
Electron Dose (C/mm²)
AC2_1
AC2_2
AC2_3
AC2_4
AC2_5

(e)

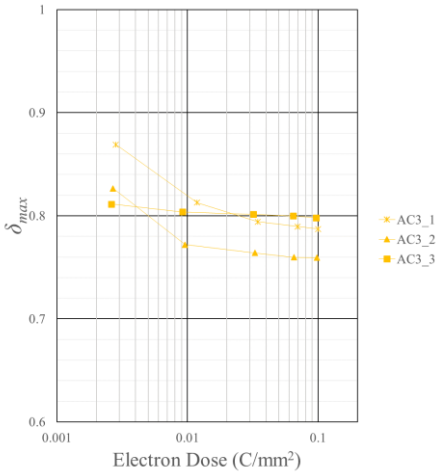
1
0.9
0.8
0.7
0.6
δ_{max}
0.001
0.01
0.1
Electron Dose (C/mm²)
AC3_1
AC3_2
AC3_3

(f)

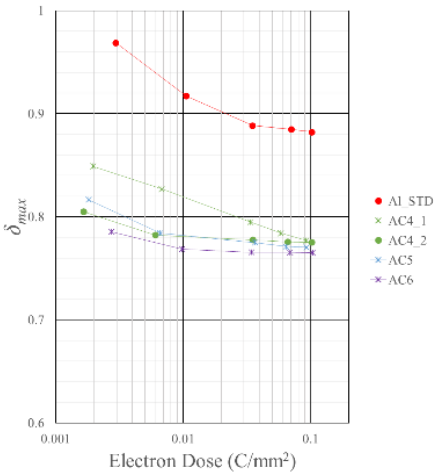
1
0.9
0.8
0.7
0.6
δ_{max}
0.001
0.01
0.1
Electron Dose (C/mm²)
Al_STD
AC4_1
AC4_2
AC5
AC6

(g)

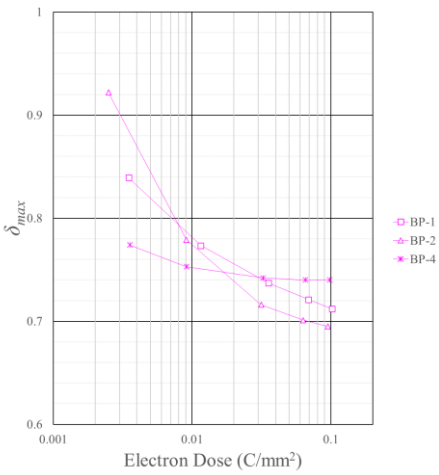
1
0.9
0.8
0.7
0.6
δ_{max}
0.001
0.01
0.1
Electron Dose (C/mm²)
BP-1
BP-2
BP-4

(h)

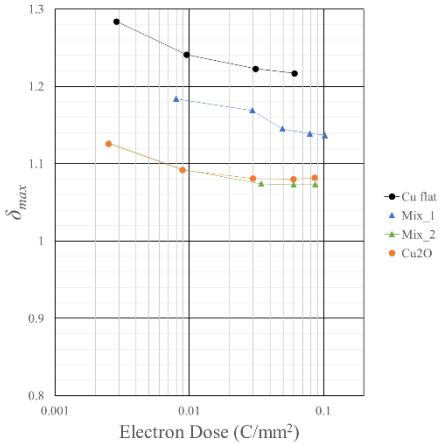

(i)

Figure 5-2: δ_{max} of all samples as a function of the electron dose

Table 5-1: δ_{max} and E_{max} of all samples after conditioning

Sample	δ_{max}	E_{max} (eV)	Sample	δ_{max}	E_{max} (eV)
Cu flat [31]	1.22	450	Cu_2O	1.08	400
S_STD [31]	0.96	650	Mix_1	1.14	500
S_GBB_LT [31]	1.06	600	Mix_2	1.07	550
Al_STD	0.88	750	Groove_20°	0.63	550
Al_LT1	0.98	550	Groove_30°	0.76	650
Al_LT2	1.20	550	Groove_60°	1.125	700
OBP_H1	0.71	1750	AC1_1	0.69	2000
OBP_H2	0.81	1950	AC1_2	0.73	2000
OBP_H3	0.72	2000	AC1_3	0.77	2000
OBP_H4	0.70	1900	AC1_4	0.73	2000
OBP_H5	0.72	1650	AC1_5	0.83	1150
OBP_S1	0.73	1100	AC2_1	0.83	2000
OBP_S2	0.71	2000	AC2_2	0.67	2000
OBP_S3	0.73	1250	AC2_3	0.75	2000
OBP_S4	0.77	1550	AC2_4	0.68	2000
OBP_S5	0.83	1000	AC2_5	0.73	1750
AC3_1	0.79	1500	AC5	0.77	1200
AC3_2	0.76	1800	AC6	0.77	750
AC3_3	0.80	1300	BP-1	0.71	1750
AC4_1	0.78	700	BP-2	0.70	600
AC4_2	0.78	1250	BP-4	0.74	1750
TiN	0.88	400			

SOKENDAI

5.1.2 SEY Properties of Triangular Groove Samples

Figure 5-1(i) and Table 5-1 show the SEY profiles of the triangular groove surfaces at three tip angles. The purpose of these data was to verify the simulation accuracy of CST for the SEY of the rough surface in the next chapter; hence, only the stable δ_{max} after conditioning was needed.

5.1.3 SEY Properties of Copper Oxide and TiN-coated Samples

Figures 5-1(j) and 5-2(i) and Table 5-1 show the SEY profiles of each copper oxide sample. The δ_{max} values of all copper oxide samples were slightly lower than that of pure copper. Among these, the δ_{max} of pure Cu_2O was 1.08, and the corresponding E_{max} was 400 eV. Therefore, the oxidation of the T.S. coating surface is beneficial to reducing SEY; however, the impact of its lower conductivity upon impedance must also be considered.

Figure 5-1(a) and 5-2(a) and Table 5-1 show the SEY profile of the TiN coating applied in SuperKEKB. The δ_{max} value was 0.88, which was slightly higher than that of the T.S. coating and was consistent with Ref. [22].

5.1.4 SEM Images

Figure 5-3 shows the 100× and 500× magnification SEM images for the T.S.-coated samples. The particle size of the copper powder used in this study was ~45 μm. The figures show that the protrusions on the surface were smaller than this particle size (except for S_GBB_LT, Al_LT1, and Al_LT2, where the bead shape was clearly observed). The topography was produced by molten copper powder bombarded and solidified onto the surface.

On OBP_S, AC1, and AC2 series samples, in addition to the protrusions produced by the splashing copper droplets, smaller villi-like structures can be observed. It can be inferred that the villi-like structures were formed by the rapid solidification of copper droplets under low surface temperatures.

SOKENDAI

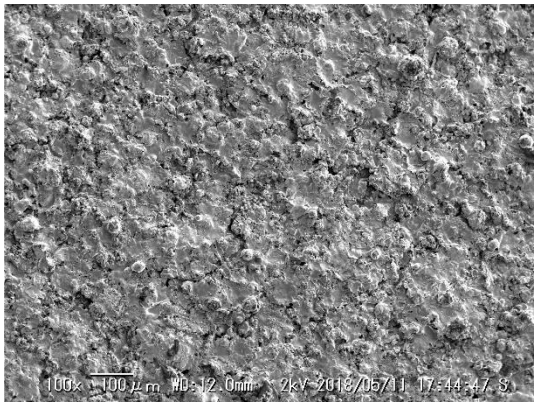

(1) S_STD 100×

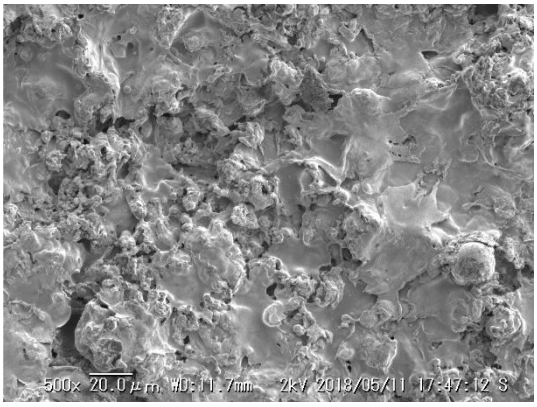

(2) S_STD 500×

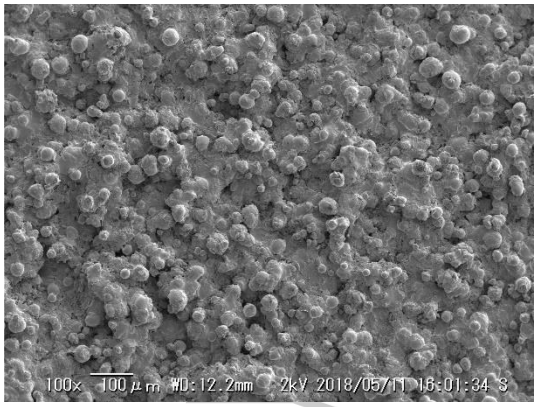

(3) S_GBB_LT 100×

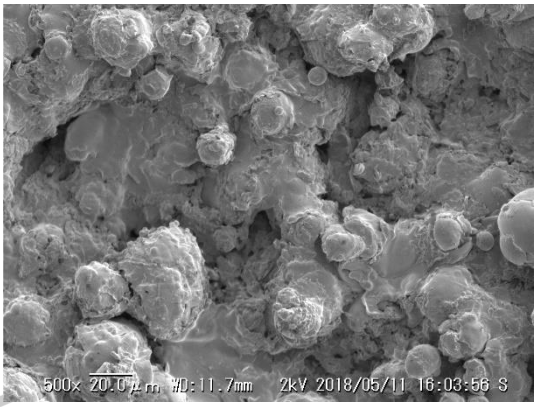

(4) S_GBB_LT 500×

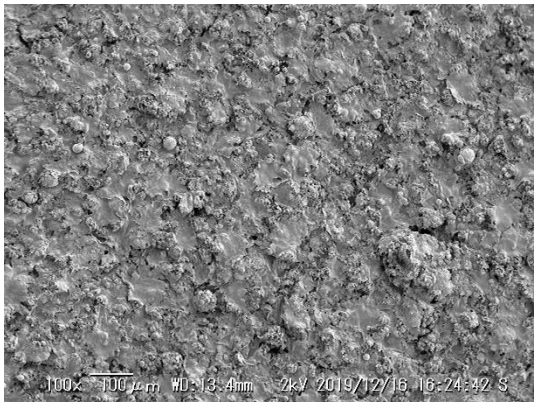

(5) Al_STD 100×

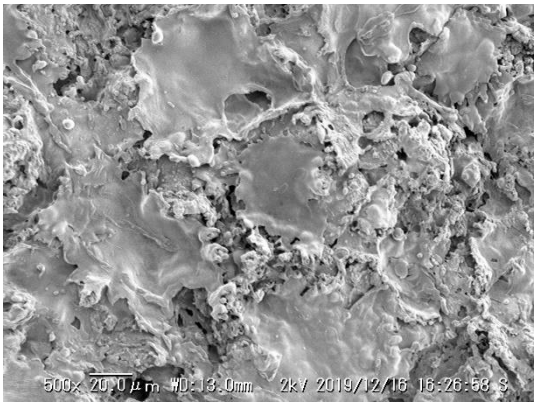

(6) Al_STD 500×

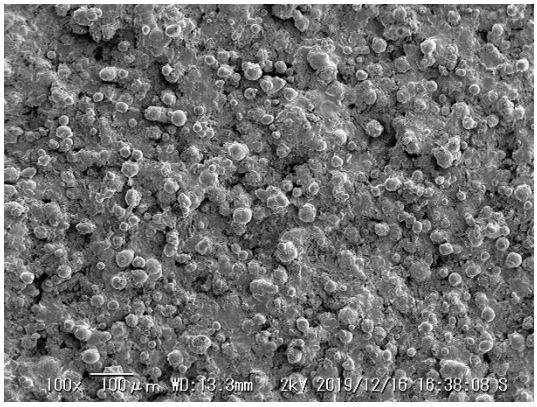

(7) Al_LT1 100×

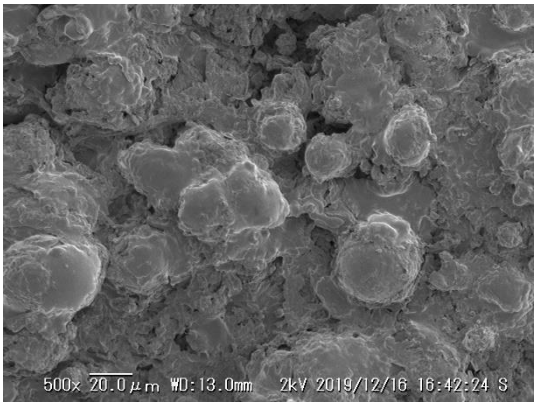

(8) Al_LT1 500×

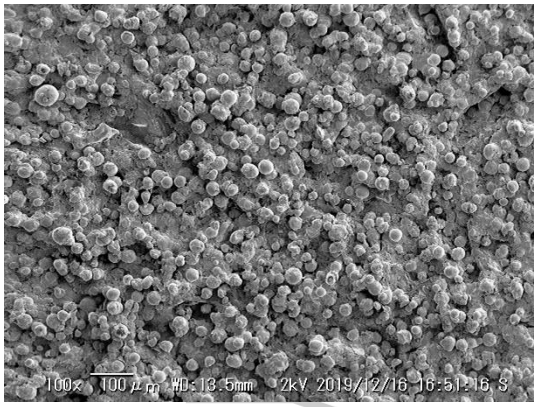

(9) Al_LT2 100×

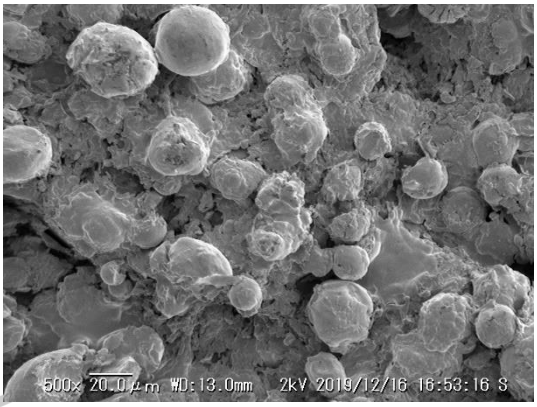

(10) Al_LT2 500×

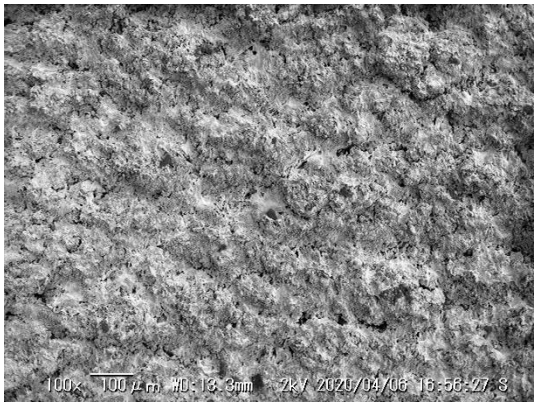

(11) OBP_H1 100×

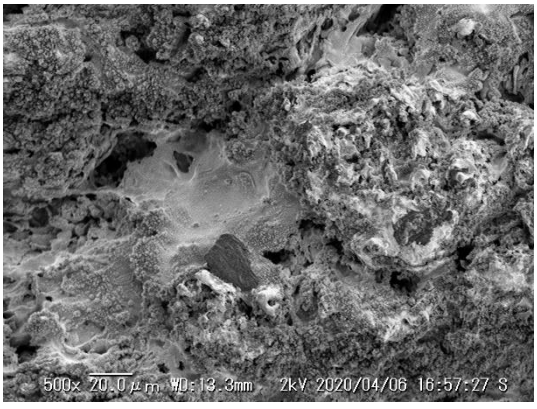

(12) OBP_H1 500×

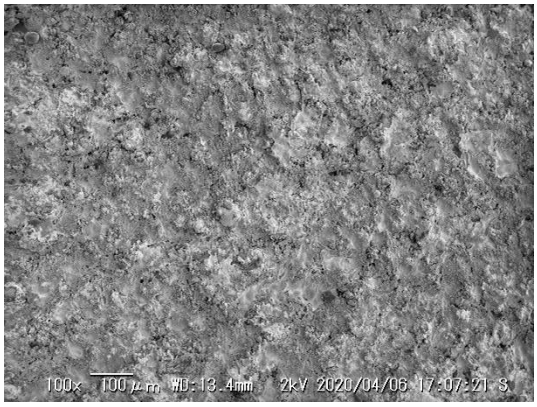

(13) OBP_H2 100×

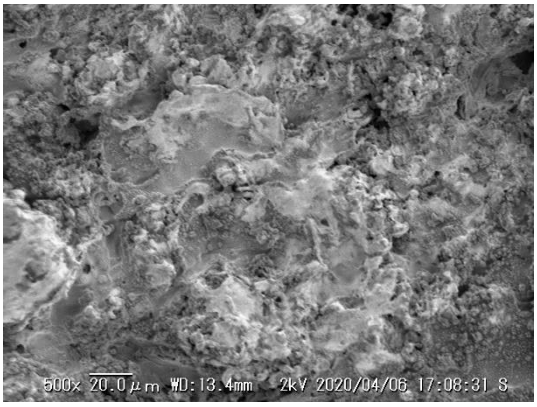

(14) OBP_H2 500×

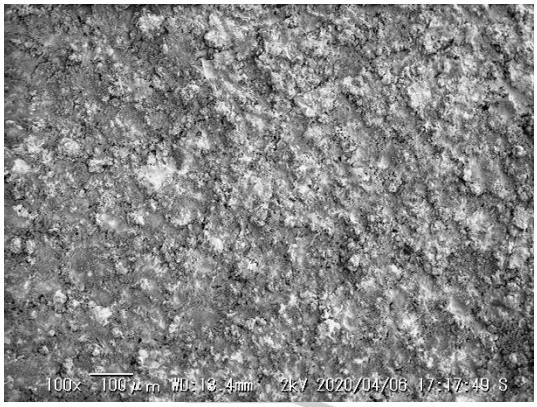

(15) OBP_H3 100×

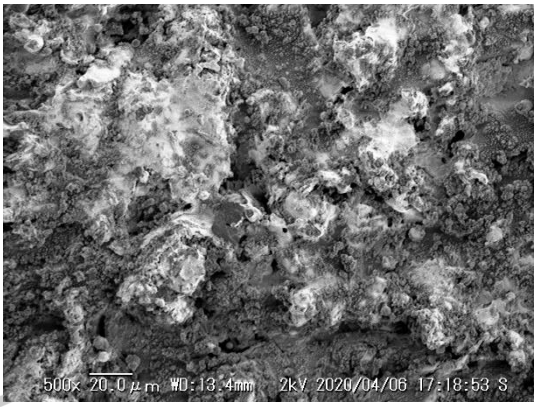

(16) OBP_H3 500×

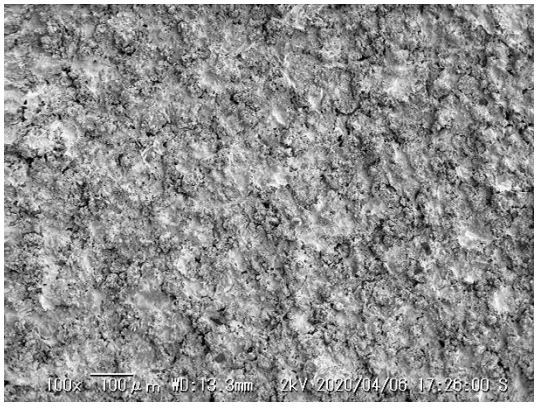

(17) OBP_H4 100×

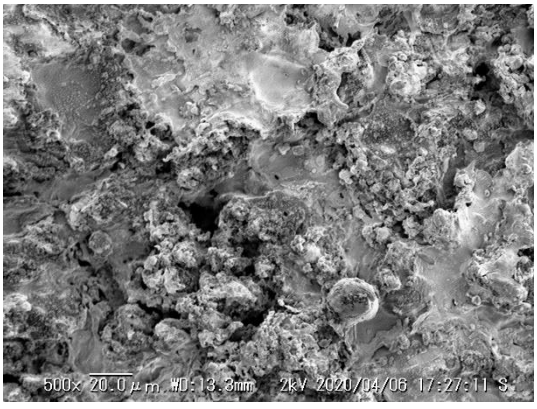

(18) OBP_H4 500×

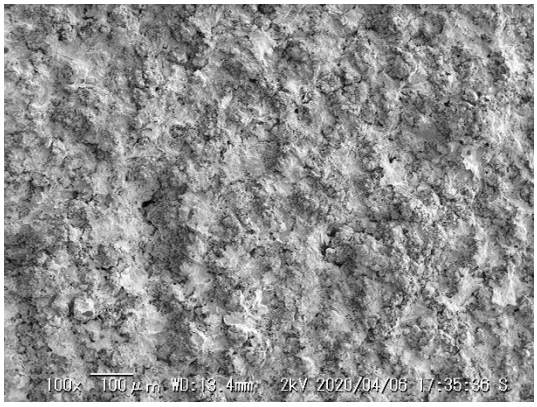

(19) OBP_H5

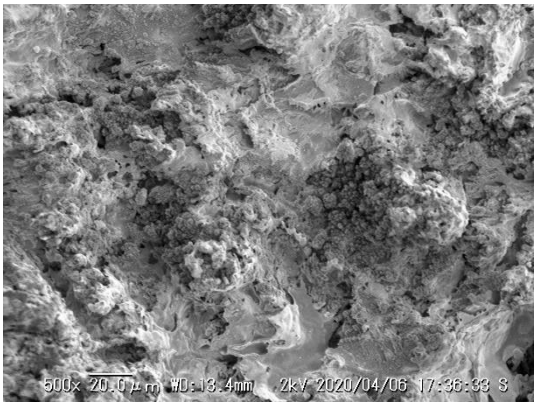

(20) OBP_H5 500×

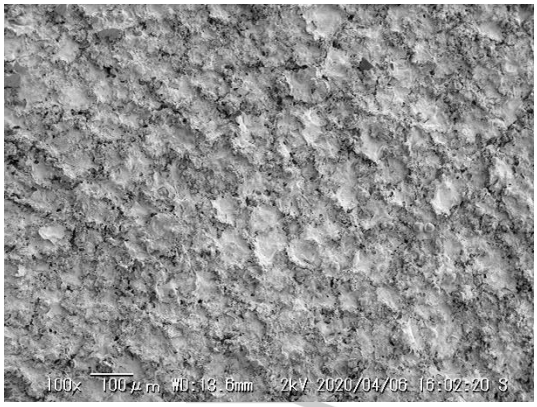

(21) OBP_S1 100×

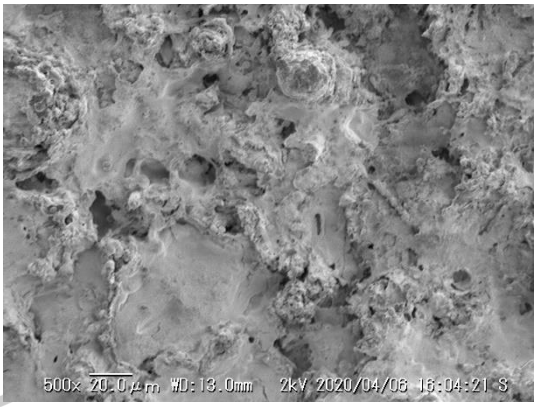

(22) OBP_S1 500×

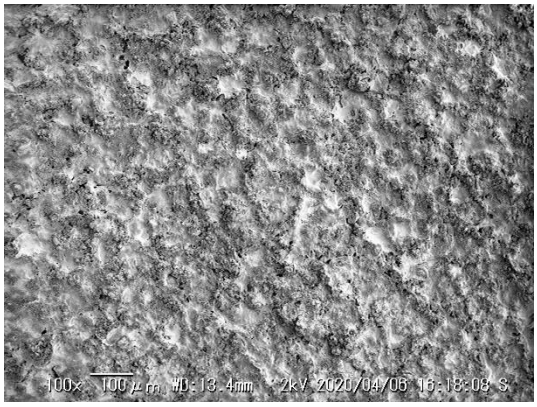

(23) OBP_S2 100×

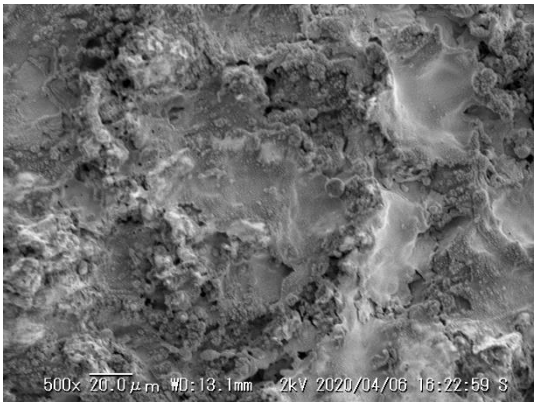

(24) OBP_S2 500×

(25) OBP_S3 100×

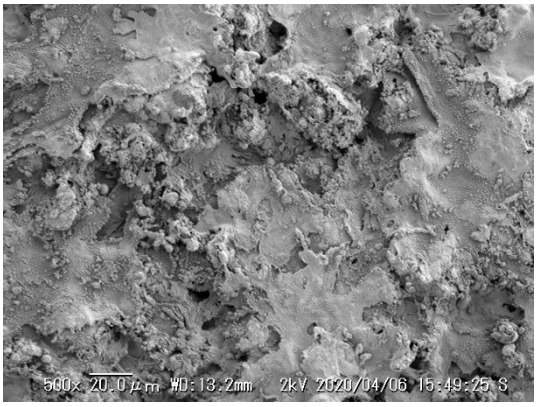

(26) OBP_S3 500×

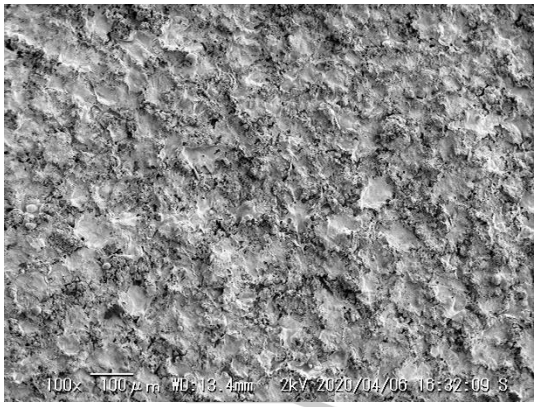

(27) OBP_S4 100×

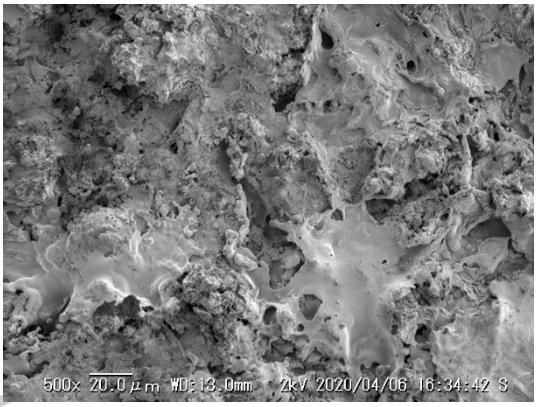

(28) OBP_S4 500×

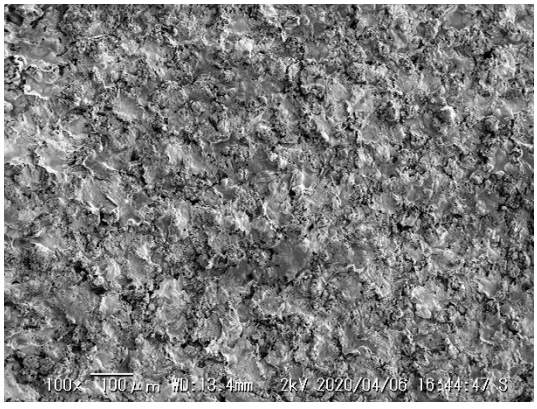

(29) OBP_S5 100×

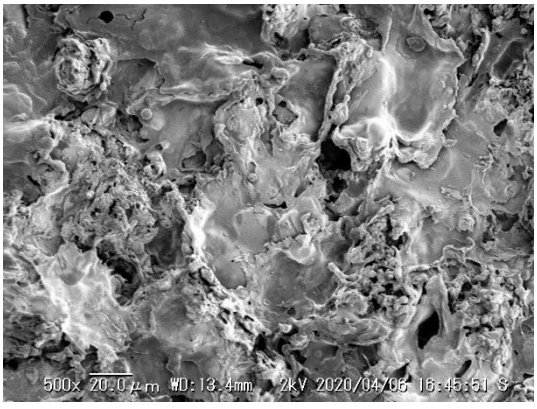

(30) OBP_S5 500×

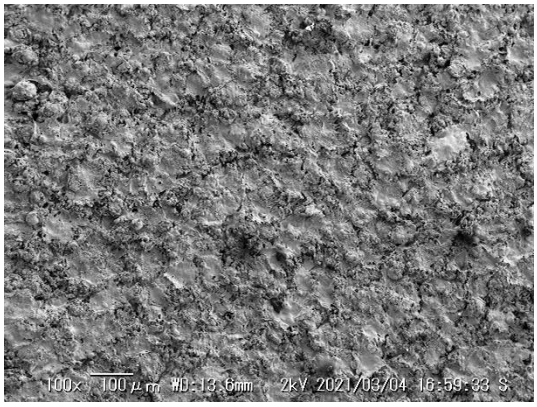

(31) AC1_1 100×

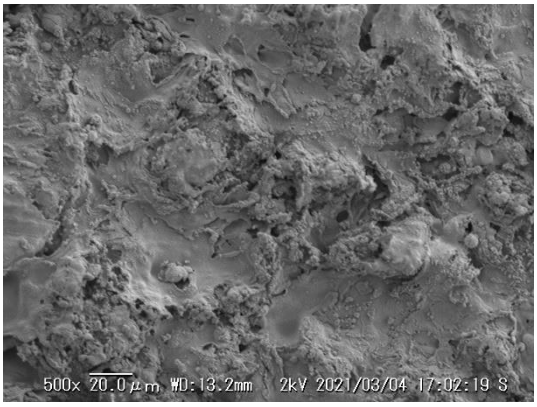

(32) AC1_1 500×

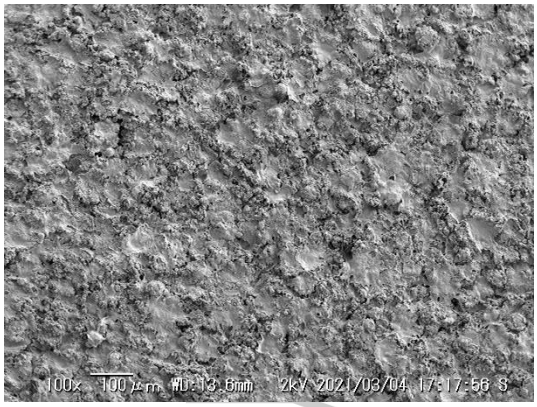

(33) AC1_3 100×

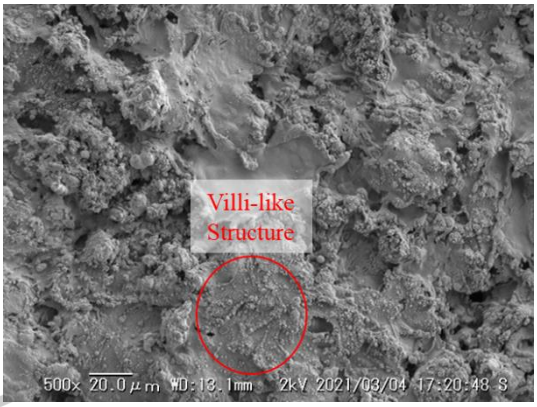

(34) AC1_3 500×

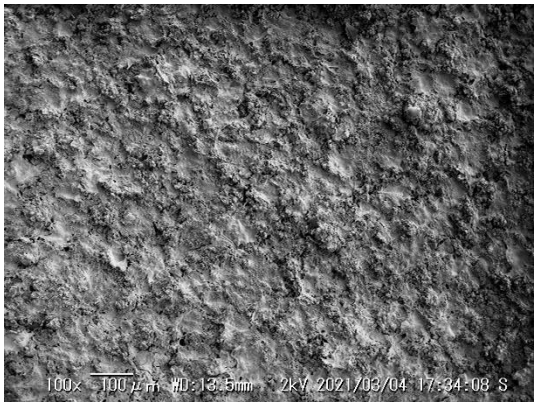

(35) AC2_1 100×

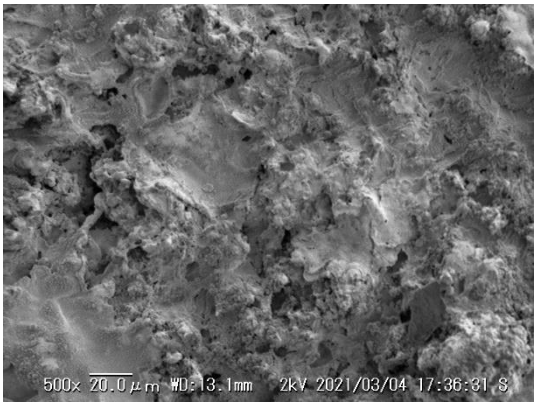

(36) C2_1 500×

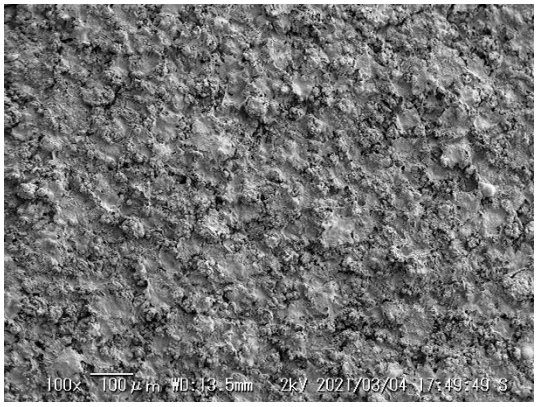

(37) AC2_3 100×

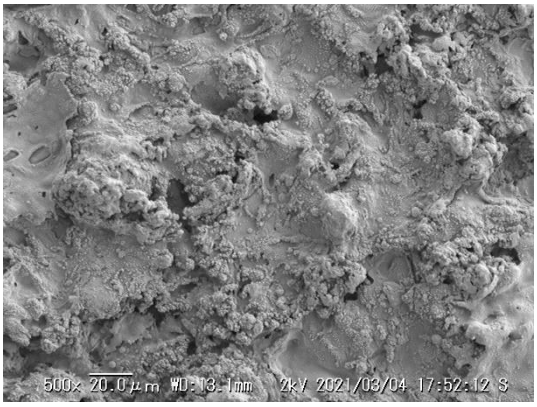

(38) AC2_3 500×

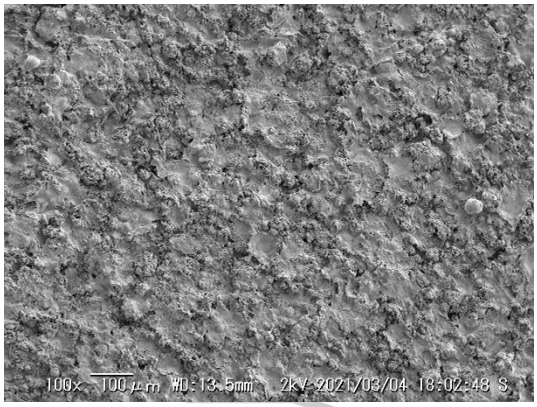

(39) AC3_1 100×

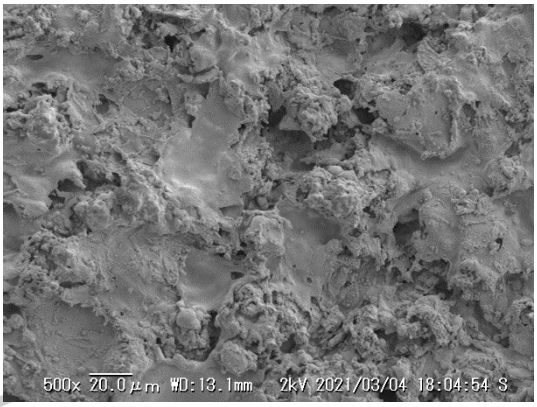

(40) AC3_1 500×

(41) AC3_3 100×

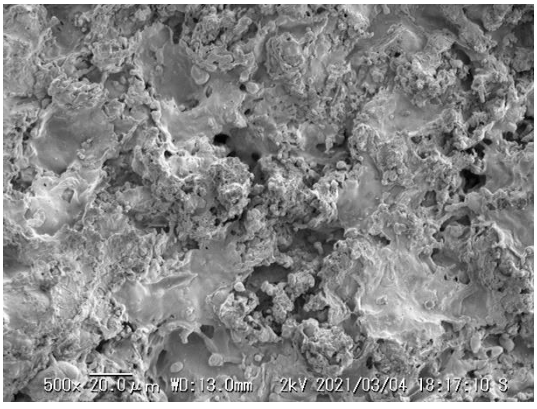

(42) AC3_3 500×

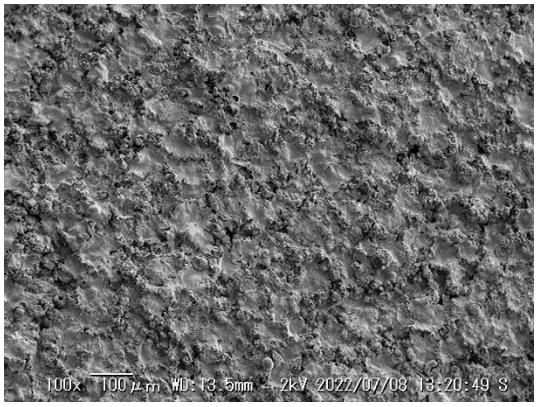

(43) AC4_1 100×

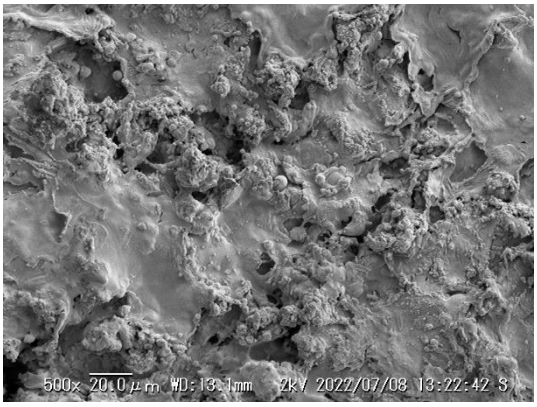

(44) AC4_1 500×

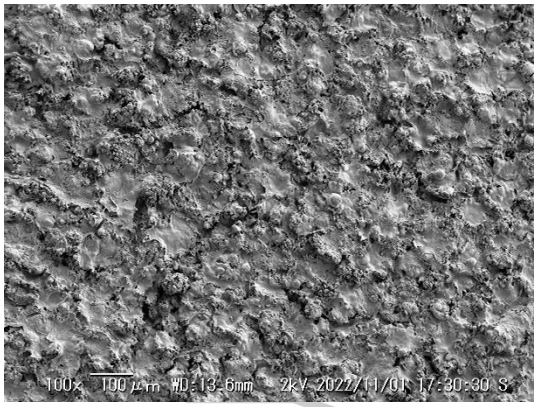

(45) AC4_2 100×

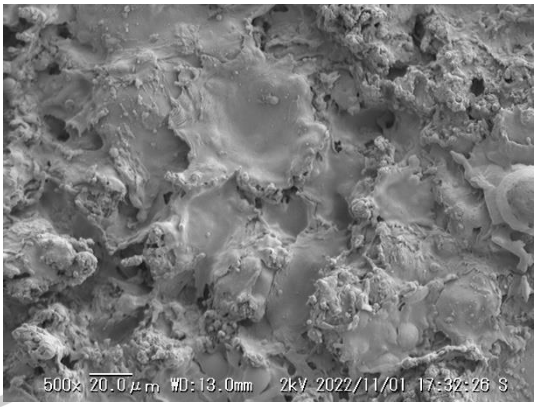

(46) AC4_2 500×

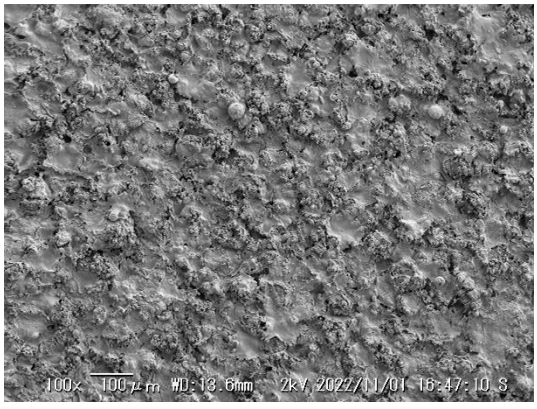

(47) AC5 100×

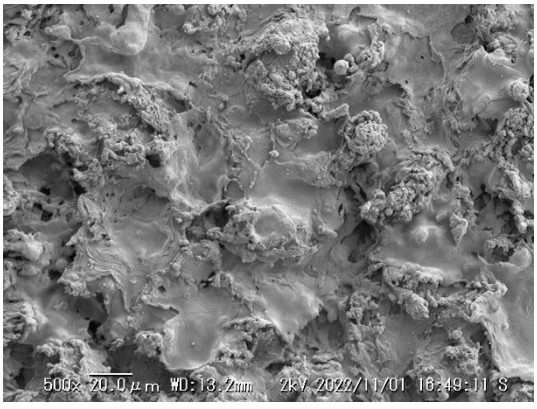

(48) AC5 500×

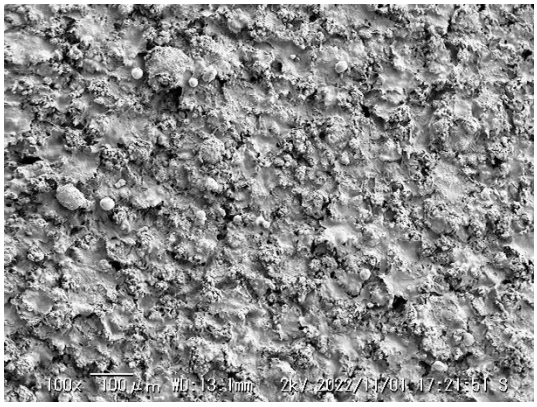

(49) AC6 100 ×

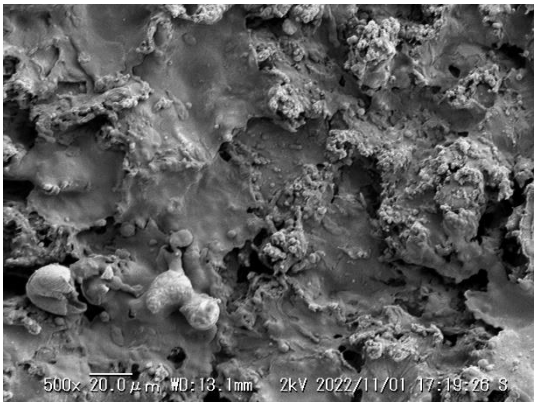

(50) AC6 500 ×

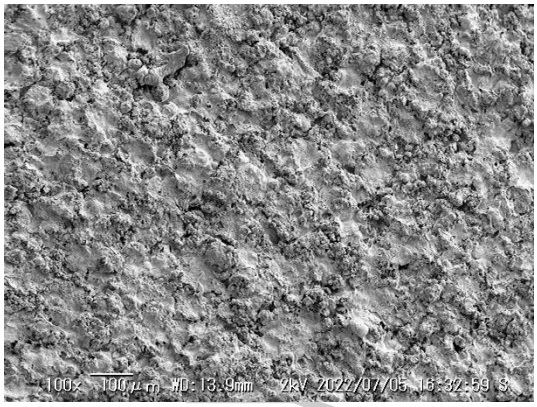

(51) BP-1 100 ×

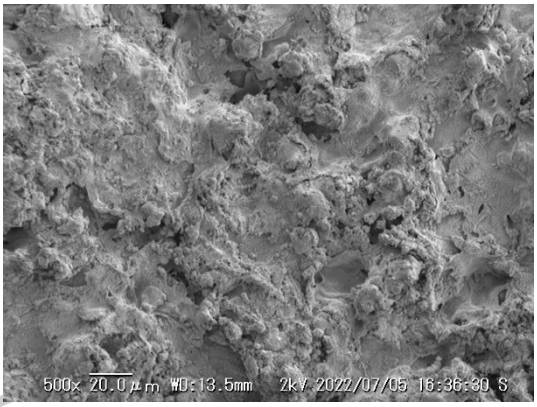

(52) BP-1 500 ×

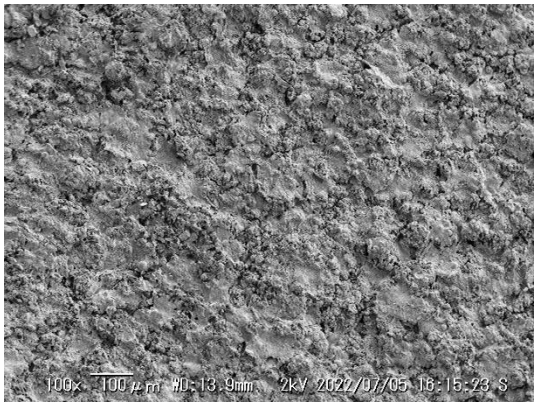

(53) BP-3 100 ×

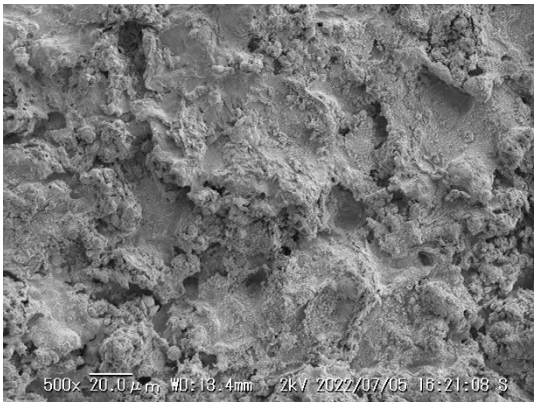

(54) BP-3 500 ×

Figure 5-3: SEM images of T.S.-coated samples

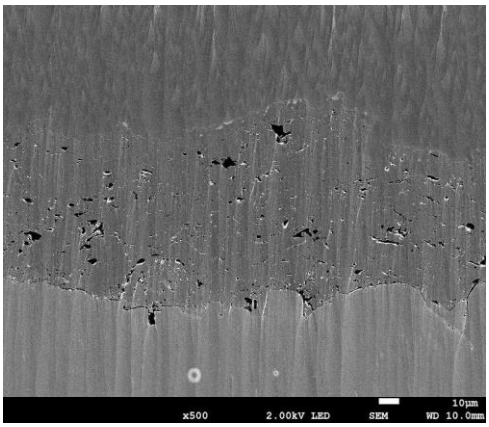

(a) Al_STD 500×

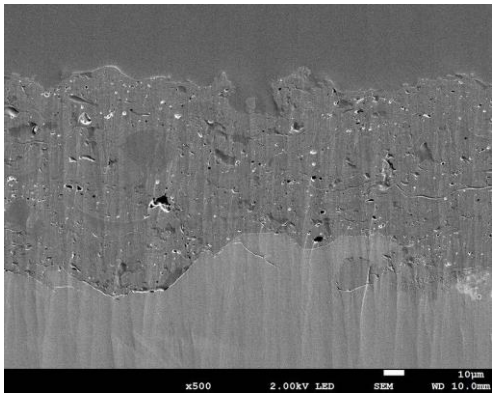

(b) AC1_3 500×

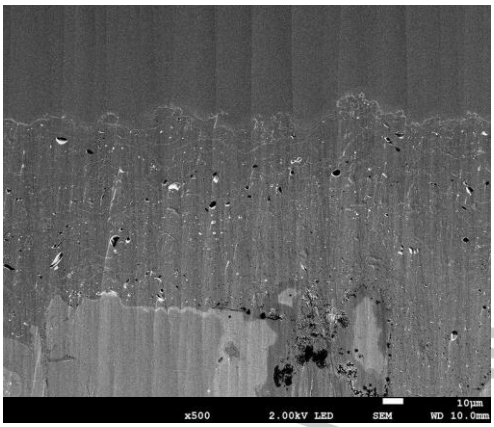

(c) AC2_3 500×

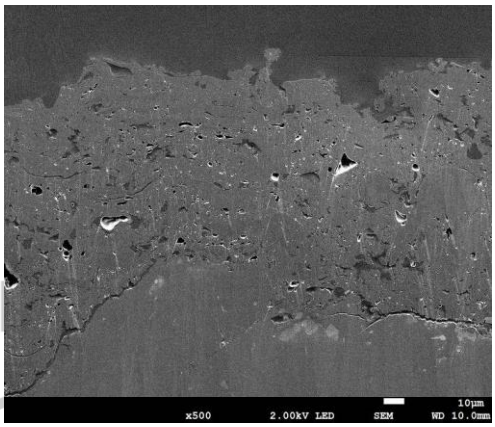

(d) AC3_1 500×

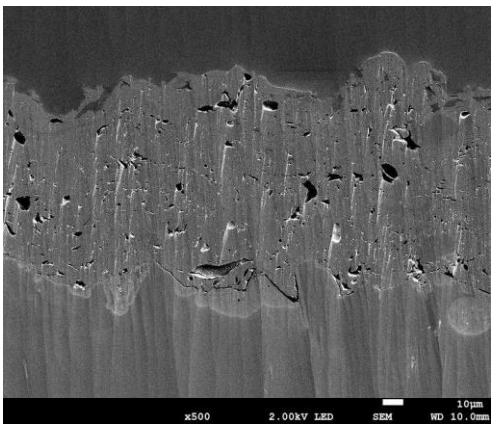

(e) AC4_1 500×

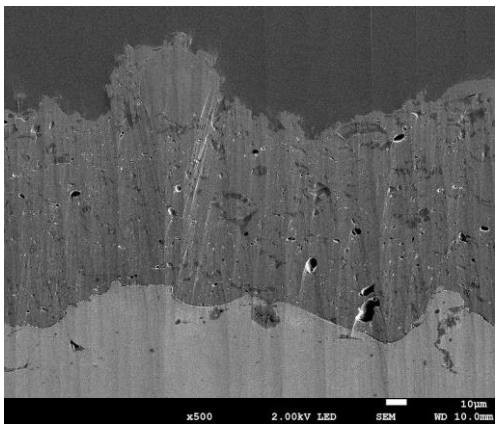

(f) BP-1 500×

Figure 5-4: SEM images of the cross-sections of T.S.-coated samples

Figure 5-4 shows SEM images of the cross-sections for several T.S.-coated samples. The profiles contained three layers (i.e., resin, T.S. coating, and aluminum substrate, from top to bottom). All thermal spray coatings feature a lamellar microstructure formed by the rapid solidification and stacking of impinging molten droplets. Formation of this lamellar microstructure is a stochastic process and associated with several variables (e.g., powder size, powder material, flame temperature, and particle velocity) [54]. In general, porosity is produced by entrapped air sacks and shrinkages during the solidification of plasma-sprayed coatings [55].

Figures 5-3 and 5-4 show multiple open pores, unfilled voids, and micro-cracks between molten powders in the thermal spray coatings. However, it is difficult to discern the differences between these samples from the SEM images.

5.1.5 XPS

Table 5-2 lists the common elements or compounds on copper oxide surfaces, as well as their corresponding binding energies [56]. The binding energy marked with an asterisk was taken from Ref. [57]. The Cu2p peaks of pure copper and its oxides are quite close; hence, it is difficult to distinguish them only via the main peak. However, if CuO is present on the surface, its strong satellite peaks at 943 and 962 eV are easy to find.

SOKENDAI

Table 5-3 lists the results for the T.S.-coated sample surfaces. XPS in this study was not a quantitative measurement; hence, only clearly observed compounds are listed. All T.S.-coated samples showed similar results; that is, before conditioning, various copper oxides were present on the surface at the same time, along with "basic copper carbonate" and some adventitious carbon; after conditioning, the CuO on the surface was reduced to Cu_2O and Cu, the basic copper carbonate almost disappeared, and the adventitious carbon was converted to graphite. Therefore, it can be deduced that the difference in SEY properties arises from the difference in surface structures (rather than surface composition).

The observed components were similar for almost every sample; hence, only the analysis procedure for sample AC1_3 is presented below. Figure 5-5 shows the XPS spectra of Cu2p, O1s, and C1s on the surface of Sample AC1_3 before and after conditioning. Before conditioning, strong satellite peaks at 943 and 962 eV (corresponding to CuO) could be found in the Cu2p spectrum, the peaks for basic copper carbonate were present in every spectrum, and the peak of adventitious carbon was found in the C1s spectrum.

After conditioning, the satellite peaks corresponding to CuO in the Cu2p spectrum disappeared completely, the peaks of basic copper carbonate were greatly reduced, and the peak of adventitious carbon disappeared, leaving only graphite peaks. It should be noted that because the thermal spray surface was rough, the position of the peak might deviate from the value in Table 5-3, and the width of the peak may become wider [40]. However, the compound represented by each peak can still be determined by cross-comparisons between the satellite peaks and the spectra of different elements.

Table 5-2: Elements or compounds often present on the surface of copper oxide, as well as their corresponding binding energies

Orbital	Elements	Binding energy [eV]	Note
Cu 2p 3/2	Cu	933 (932.6*)	
	CuO	933 (933.7*)	Strong satellite @ 943 & 962
	Cu_2O	933.5 (932.5*)	Weak satellite @ 945
	$CuCO_3 \cdot Cu(OH)_2$	934.7 (935.1*)	So-called "basic copper carbonate"
O 1s	Cu_xO	529–530	
	$CuCO_3$	531.5–532	
	$Cu(OH)_2$	533	
C 1s	sp2 Carbon (Graphite)	284	Adventitious carbon 284.8
	$CuCO_3$	288–289	HCO_3^-: 289–290

Table 5-3: Main components of T.S.-coated sample surfaces

Sample	Before conditioning			After conditioning		
	Cu 2p	O 1s	C1s	Cu 2p	O 1s	C1s
S_STD	-	-	-	Cu, Cu_2O	Cu_xO	Graphite, adv. C
S_GBB_LT	-	-	-	Cu, Cu_2O	Cu_xO	Graphite, adv. C
Al_STD	-	-	-	Cu, Cu_2O	Cu_xO	Graphite, adv. C
Al_LT1	-	-	-	Cu, Cu_2O	Cu_xO	Graphite, adv. C
Al_LT2	-	-	-	Cu, Cu_2O	Cu_xO	Graphite, adv. C
AC1_1	Cu, Cu_2O, CuO, $CuCO_3/Cu(OH)_2$	Cu_xO, $CuCO_3/Cu(OH)_2$	Adv. C, $CuCO_3$, HCO_3	Cu, Cu_2O	Cu_xO	Graphite, adv. C
AC1_3	Cu, Cu_2O, CuO, $CuCO_3/Cu(OH)_2$	Cu_xO, $CuCO_3/Cu(OH)_2$	Adv. C, $CuCO_3$	Cu, Cu_2O	Cu_xO	Graphite, adv. C

SOKENDAI

AC2_1	Cu, Cu_2O, CuO, $CuCO_3/Cu(OH)_2$	Cu_xO, $CuCO_3/Cu(OH)_2$	Adv. C, $CuCO_3$	Cu, Cu_2O	Cu_xO	Graphite, adv. C
AC2_3	Cu, Cu_2O, CuO, $CuCO_3/Cu(OH)_2$	Cu_xO, $CuCO_3/Cu(OH)_2$	Adv. C, $CuCO_3$	Cu, Cu_2O	Cu_xO	Graphite, adv. C
AC3_1	Cu, Cu_2O, CuO, $CuCO_3/Cu(OH)_2$	Cu_xO, $CuCO_3/Cu(OH)_2$	Adv. C, $CuCO_3$	Cu, Cu_2O	Cu_xO	Graphite, adv. C
AC4_1	Cu, Cu_2O	Cu_xO	Graphite, adv. C	Cu, Cu_2O	Cu_xO	Graphite, adv. C
BP-1	-	-	-	Cu, Cu_2O	Cu_xO	Graphite, adv. C
BP-3	Cu, Cu_2O	Cu_xO	Graphite, adv. C	-	-	-

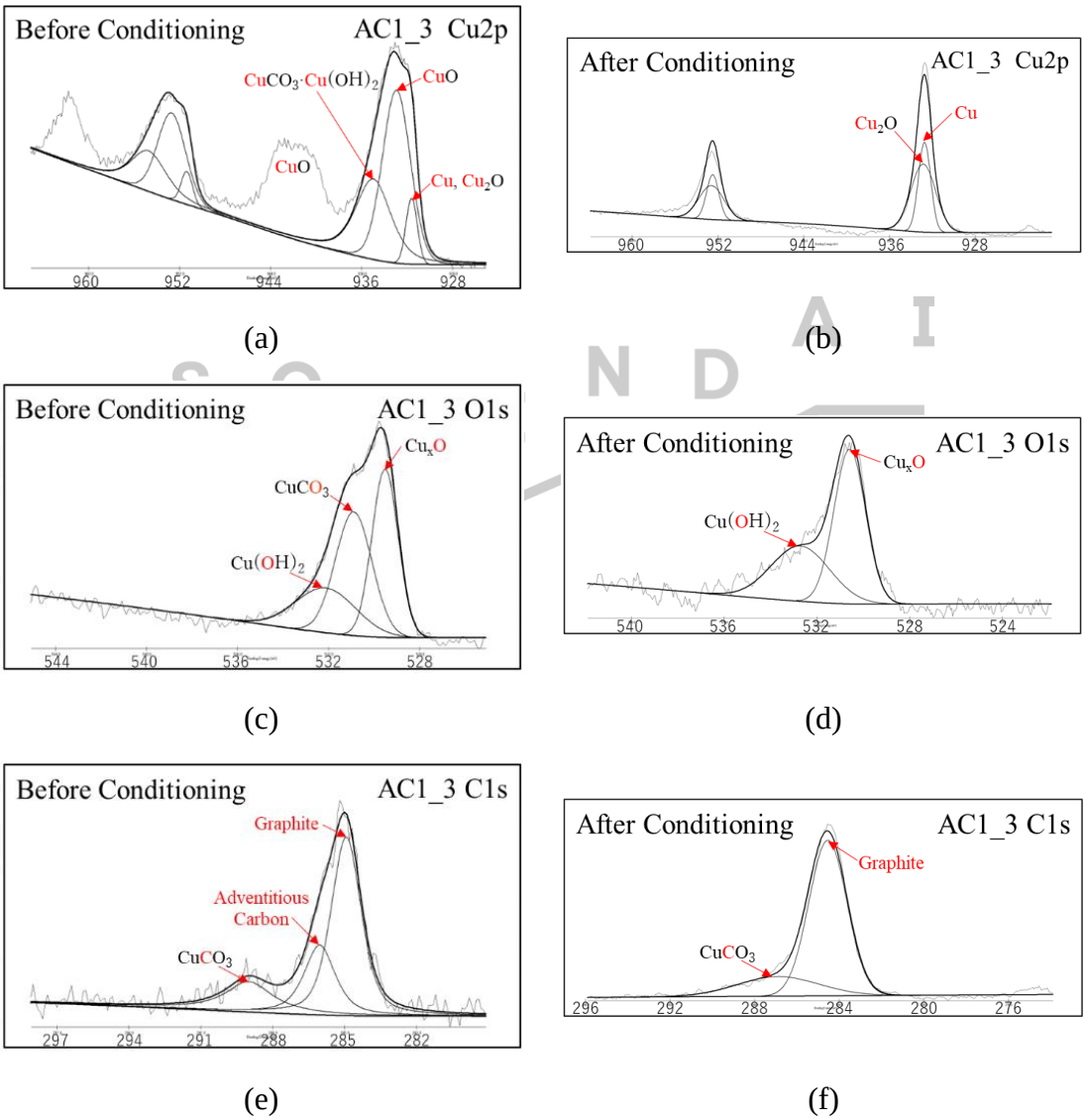

Figure 5-5: XPS spectra of Cu2p, O1s, and C1s on the surface of sample AC1_3 before and after conditioning

Figure 5-6 shows the depth profile of Sample AC4_1 after conditioning. The atomic percentage of copper increased and the atomic percentage of oxygen and carbon decreased with increasing depth. To a depth of 2 μm from the surface, the atomic percentage of copper increased sharply from 73.7% to 91.3%. Then, it reached a stable value of ~97% at a depth of 6 μm. This means that most of the copper oxide was concentrated above a surface depth of 2.0 μm. Of the 73.7% copper present in the outermost layer, 30.8% should be Cu_2O (twice as oxygen); the rest should be pure copper.

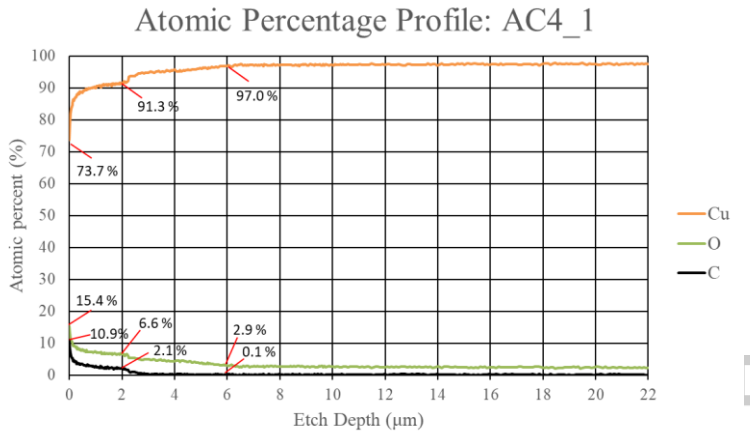

Figure 5-6: Depth profile of sample AC4_1 after conditioning

5.1.6 Dependence on Temperature During Spraying

This section discusses the relationship between the SEY properties and surface temperature during spraying for the AC series samples; this is one of the significant results of this study. To avoid unstable SEY profiles for samples located at the edge of the beam pipe (as mentioned in Section 5.1.1), only samples located in the center of the beam pipe were selected. Figure 5-7(a) shows the δ_{max} of the selected AC series samples as a function of the surface temperature during spraying. The results show that the δ_{max} had no clear correlation below a 300 °C surface temperature. However, Table 5-1 shows that their E_{max} values were different. δ is a function of E_p; hence, the energy of the electrons hitting the inner wall of the beam pipe is important. Therefore, PyECLOUD was used to estimate the average electron energy in the beam pipe of SuperKEKB. PyECLOUD is a 2D macro-particle code developed by CERN for the simulation of ECEs in particle accelerators [58]. The following parameters were inputted:

- Circular beam pipe radius = 45 mm
- Bin width = 1.5 mm (interval between mesh points in each dimension for the generation of uniform grid for the 5-D phase space used in microparticle regeneration)
- Photo-electron emission yield = 1.6×10^{-3} e^-/photon
- $\delta_{max} = 0.7$
- $E_{max} = 332$ eV
- Bunch spacing = 3.96 RF bucket spacing
  → Approximately corresponding to $n_b = 1272$
- $I_{bunch} = 0.5$ mA bunch^{-1} RF bucket^{-1}

The horizontal distribution integrated in the vertical direction of the electrons in the beam pipe was shown in Fig. 5-7(c); it resembled a cosine distribution (i.e., the distribution of electrons in the beam pipe was almost even). First, we used Eq. (3-22) to calculate the electron energy at each position in the beam pipe; then, using the distribution in Fig. 5-7(c), we obtained the weighted average energy of electrons in SuperKEKB, as ~300 eV.

Therefore, δ_{300} (δ at $E_p = 300$ eV) was plotted with respect to the surface temperature, as shown in Fig. 5-7(b). Thus, the surface temperature during spraying was positively correlated with δ_{300}. This implies that if the average electron energy in the beam pipe is assumed to be 300 eV, the lower surface temperature during spraying achieves a superior secondary electron suppression effect.

The high E_{max} of the thermal spray surfaces is explained as follows: As mentioned in Section 1.1.3.5, when electrons are normally incident on a rough surface, the angle of incidence—on a microscopic scale—is not zero degrees. From Eq. (2-10), when the incident angle is not zero degrees, both δ_{max} and E_{max} will increase. The increased secondary electrons will be captured by the structure of the rough surface; hence, the final δ_{max} will decrease but the corresponding E_{max} will still increase. However, from Eq. (2-10d), even if the incident angle of primary electrons is assumed to be the limit of 90°, the E_{max} of the flat copper surface will increase to a maximum of ~760 eV, still lower than the E_{max} of several thermal spray samples (see Table 5-1). Other factors appeared to affect E_{max}; these merit further investigation.

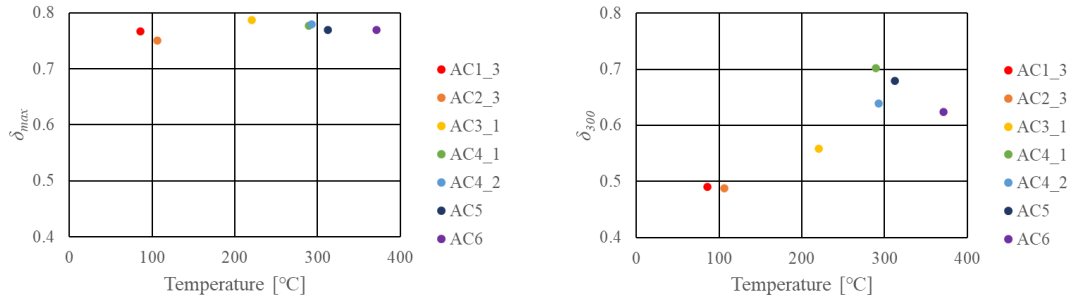

(a) (b)

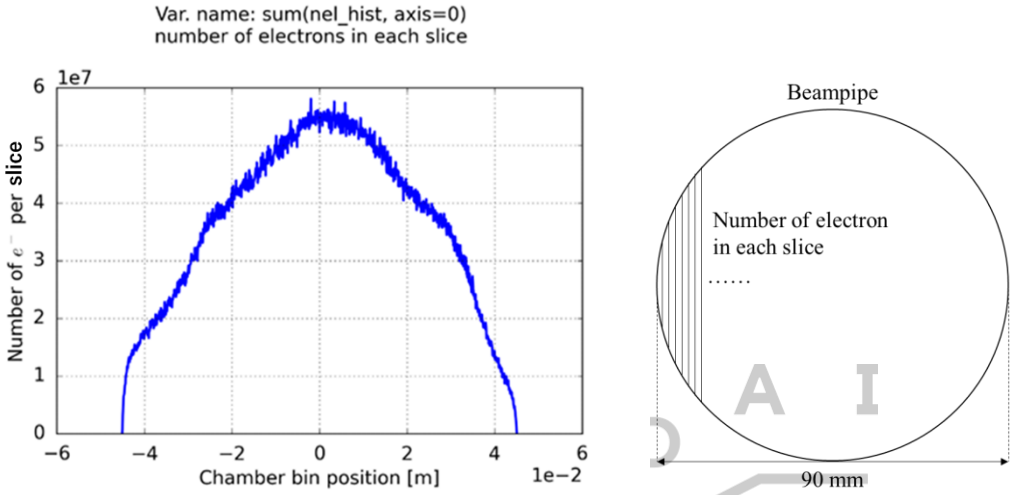

(c)

Figure 5-7: (a) δ_{max} of the selected AC series samples as a function of surface temperature during spraying; (b) δ_{300} of the selected AC series samples as a function of surface temperature during spraying; and (c) horizontal distribution integrated in the vertical direction of the electrons in the beam pipe for SuperKEKB, as obtained using PyCLOUD

5.2 Feasibility in Accelerators

5.2.1 Electron Density

5.2.1.1 Electron density without magnetic fields

Figure 5-8 shows the electron density with respect to the current linear density (i.e., bunch current/ RF bucket spacing) in the TiN, copper, T.S.-coated, TiN groove, and bare groove beam pipes of SuperKEKB LER, as collected during different operation periods (see Table 4-4). The bunch number refers to the number of positron clusters per one cycle of the ring, and the bunch current is simply the beam current divided by the bunch number. The bunch train length was fixed, and 4800 RF buckets could be filled in the bunches during one cycle; thus, one bunch spacing was approximately equal to 4800 divided by the bunch number. When the bunch number varied, the bunch spacing and bunch current were prone to change. The current linear density of the x-axis allows us to compare the electron densities of different bunch numbers; its value is equal to the total beam current divided by 4800. The data for these time periods were chosen because they had a higher current linear density and therefore facilitated a better comparison of the differences between beam pipes.

SOKENDAI

The first period ran from 11th Mar. 2021 to 5th Jul. 2021. As shown in Fig. 5-8(a–d), the main test beam pipe in the first period was made of copper (Monitor 2). Then, the main test beam pipe was replaced with the beam pipe with a T.S. coating (Monitor 2) for the second period. Figure 5-8(c–d) shows the electron density collected between 21st Feb. 2022 and 22nd Jun. 2022. The large jitter in the electron density at low bunch currents occurred because it lay outside of the applicable range of the electron density formula given in Ref. [41] (see Section 3.2.1).

The electron density in the T.S.-coated beam pipe was of the same order as those for TiN, copper, and the TiN groove beam pipe. The electron densities were of the order of 10^{11} m^{-3} up to the ~0.25 mA bunch^{-1} RF bucket^{-1} and were all considerably smaller than that of the uncoated aluminum groove beam pipe. This result shows that the T.S.-coated beam pipe had a good suppression effect upon the electron cloud, even under the influence of the uncoated aluminum mesh screen.

In Fig. 5-8(e–g), the “bump” of the curves could be observed around a current linear density of 0.25 mA bunch^{-1} RF bucket^{-1}. The bump position was determined according to

the timing of the acceleration of electrons via successive bunches and altered by the bunch fill patterns. The shapes and positions were found to depend not only upon δ_{max} but also upon the initial energy of the emitted secondary electrons and the radii of the beam pipes [59]. For the simulations in Ref. [5], the significant bump could only be observed when δ_{max} was lower than 1.2.

5.2.1.2 Electron density in vertical magnetic field B_y

Figure 5-9 shows the normalized current ratios $I_{e\_T.S.\ coating}/I_{e\_TiN}$ and $I_{e\_TiN\_groove}/I_{e\_TiN}$ as a function of the solenoid coil current under different beam conditions (i.e., different bunch numbers and maximum values of total beam current). I_e indicates the current received by the anode of the electron monitor. The coil current was only listed up to 1.5 A (which corresponded to 12 Gauss) because when the coil current exceeded 1.5 A, the signal became very small, even lower than the background value of Monitor 2 (~10^{-8} A); as a result, the standard deviation of the current ratio became too large.

The results of the current ratio $I_{e\_TiN\_groove}/I_{e\_TiN}$ were consistent with the results in Fig. 3-10, indicating a downward trend. We took TiN as a comparison standard to observe the T.S. coating: it also showed a downward trend. As stated in Section 3.2.1.3, these downward trends imply that the T.S. coating and TiN groove surface can suppress the EC more than the TiN coating in accelerators.

SOKENDAI

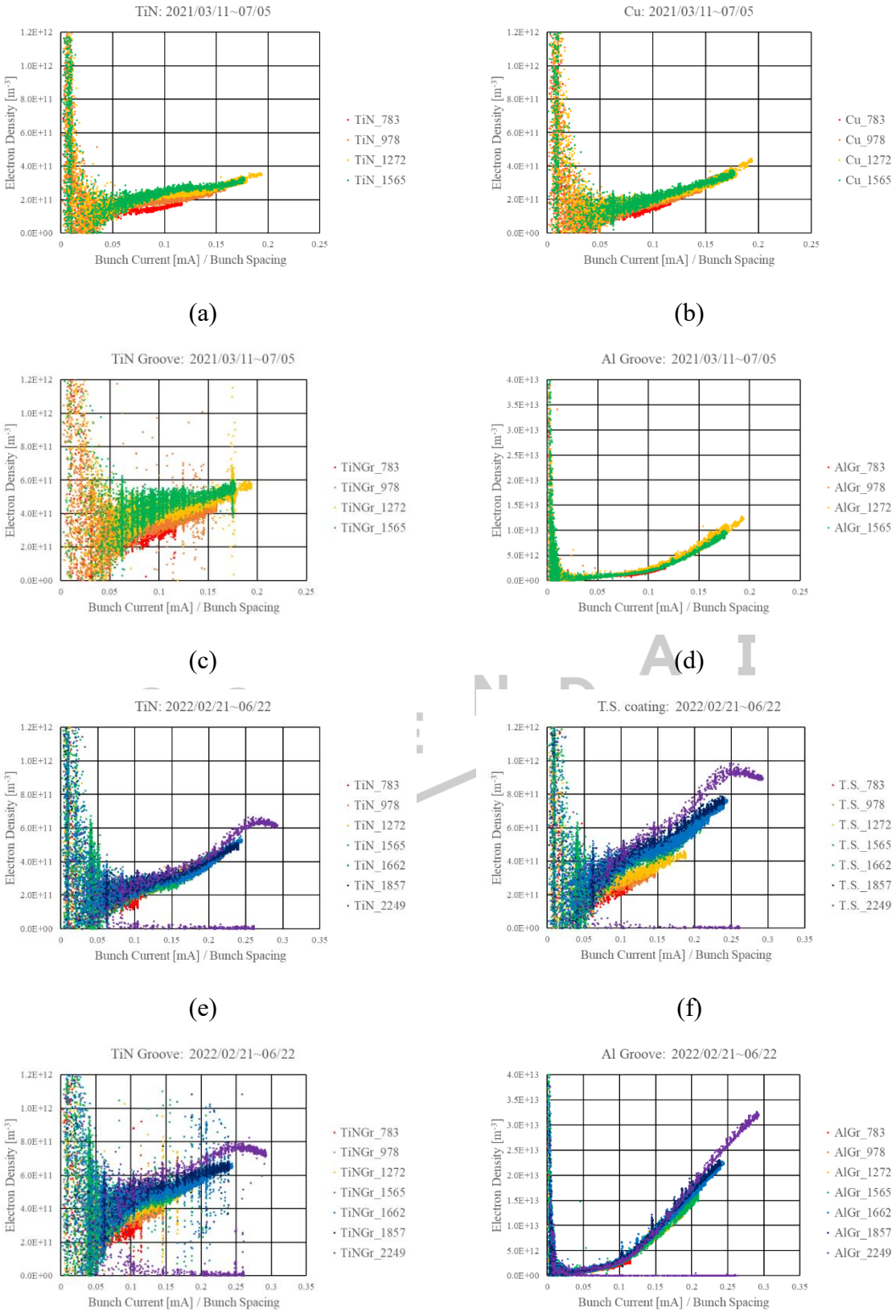

Figure 5-8: Electron densities in the TiN, copper, T.S.-coated, TiN groove, and bare groove beam pipes as a function of the current linear density in different periods. Note that the scale of the vertical axis in (h) differs from the others

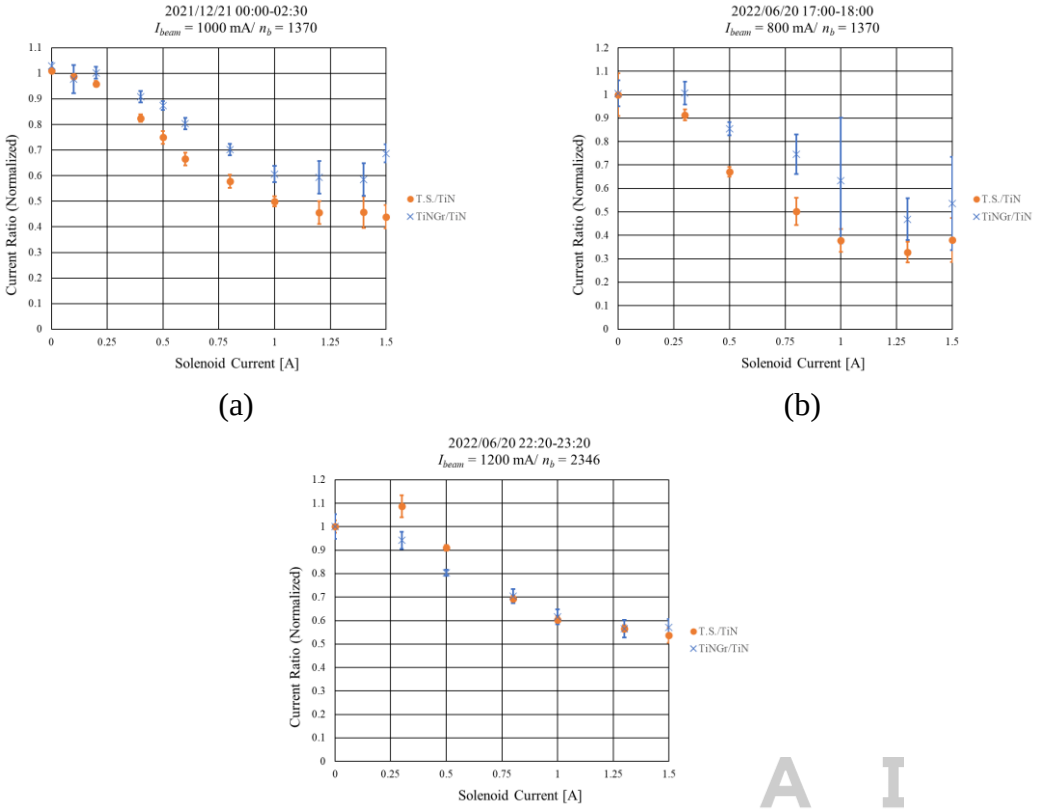

Figure 5-9: Normalized current ratios $I_{e\_T.S.\ coating}/I_{e\_TiN}$ and $I_{e\_TiN\_groove}/I_{e\_TiN}$ as a function of the solenoid coil current under different beam conditions

5.2.2 Outgassing Rate

Figure 5-10(a–d) show the outgassing (outgassing rate × surface area) of the Al substrate, Al_STD, Al_LT1, and Al-LT2, as well as the background values from the chamber for 100 h after baking at 160 ℃ for 24 h.

Until 10 h after baking, the outgassing from the chamber and sample were approximately of the same order of magnitude, so the measured value was reliable; however, after 10 hours, the outgassing from the T.S. sample gradually decreased to less than 20% of the total outgassing; as a result, the accuracy became lower, and jittering of the curve could be observed. Figure 5-10(e) shows the outgassing rate of the Al substrate, Al_STD, Al_LT1, and Al-LT2 for 100 h after baking at 160 ℃ for 24 h. The outgassing rates of the T.S.-coated samples were lower than that of the aluminum substrate. However, owing to the relatively high background values in the measurements, it can only be conservatively stated that the outgassing rates of the T.S.-coated samples were close to that of aluminum and fell below 1×10^{-9} Pa·m/s after 100 h.

Compared to copper, the electro-polished OFC had an outgassing rate of 2.90×10^{-11} Pa·m/s at 200 h after baking at 100 ℃ for 24 h [60]. Reference [61] indicates that the outgassing rate of the unpolished copper lining electroformed on the stainless steel vacuum duct after baking at 150 ℃ for 23 h was of the order of 10^{-8} Pa·m/s.

Although the outgassing rate of the T.S. coating exceeded that of OFC, it still satisfies the static desorption rate requirement of SuperKEKB, which is $< 10^{-8}$ Pa·m/s [10]. Furthermore, no abnormal pressure was detected on the two vacuum gauges closest to the T.S.-coated beam pipe.

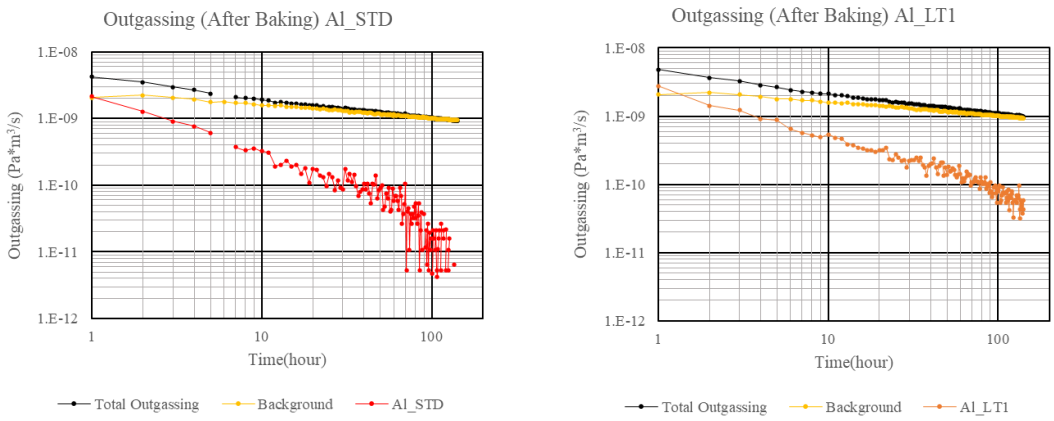

(a)

(b)

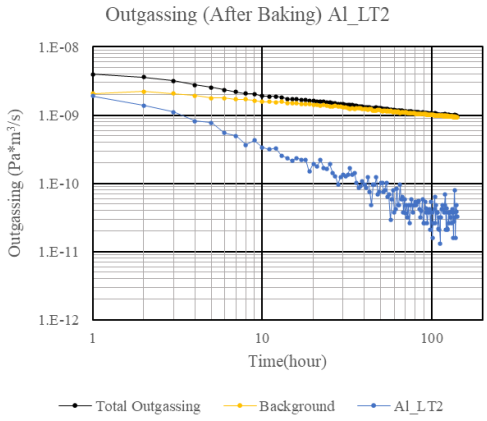

(c)

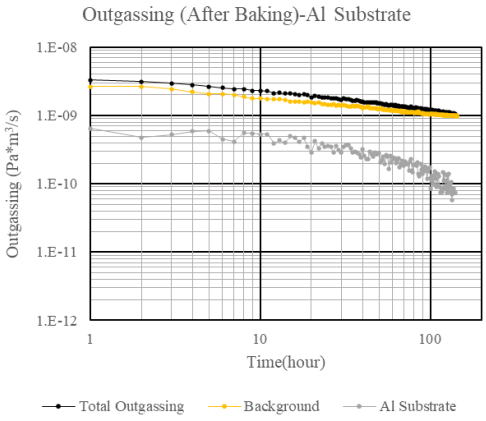

(d)

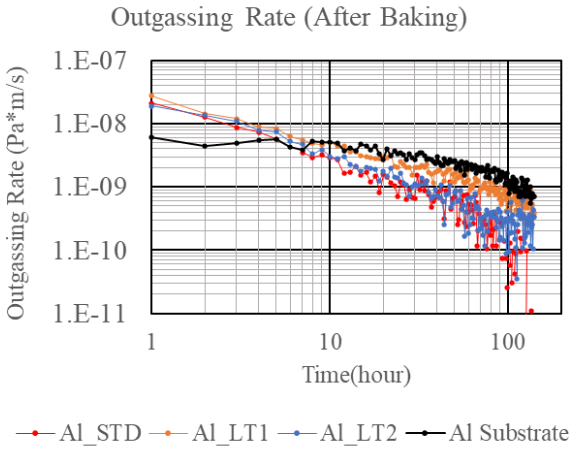

(e)

Figure 5-10: (a–d) Outgassing rate × Area and background of Al substrate, Al_STD, Al_LT1, and Al-LT2; (e) outgassing rate of Al substrate, Al_STD., Al_LT1, and Al-LT2 for 100 h after baking at 160 ℃ for 24 h

5.2.3 Dust Generation

The number of dust particles divided by the coating area [mm^2] for two T.S.-coated samples (as-received and cleaned with compressed air) and NEG strips are listed in Table 5-4. The plots in Fig. 5-11 were constructed from the data in Table 5-4.

SOKENDAI

All results were similar after three measurements, and numerous particles were still detected. It was also found that the cleaning of compressed air did not have much effect on the dust reduction. The NEG strips were installed in the antechamber of the SuperKEKB; hence, they did not directly “see” the beam and their dust requirements were not strict. However, the thermal spray coating was applied to the inner wall of the beam pipe, directly facing the beam; hence, the quantity of dust must be small enough to not affect the beam. The dust generation of T.S.-coated samples, as measured using this method, appeared to be high; however, there were no signs of problems produced by dust (e.g., pressure burst in the SuperKEKB). The high dust levels obtained via this method may be attributable to additional coating peeling attributable to ultrasonic vibrations; this is one reason why the compressed air does not reduce the dust count.

Regarding the composition of the dust, the dust from the T.S.-coated samples was mainly composed of Cu, O, Al, and C; meanwhile, that from the NEG strips was mainly composed of Zr, V, and small amounts of Fe, Al, C, and O, as expected.

Table 5-4: Dust count divided by the coating area [mm^2] of as-received and compressed-air-cleaned T.S.-coated samples and NEG strips

Sample	Particle Size [μm]	Trial 1	Trial 2	Trial 3	Trial 4	Trial 5
AC1 As-received	4~6	1057.5087	189.1301	152.5374	104.3713	66.9693
	6~14	125.4118	64.3499	28.6489	24.9824	18.1938
	14~21	6.1315	3.0502	0.6927	1.3914	1.0817
	21~38	2.0415	1.0938	0.2270	0.4876	0.3211
	38~70	0.0830	0.0491	0.0087	0.0180	0.0108
	70~	0.0035	0.0011	0.0004	0.0021	0.0000
AC1 After blowing	4~6	1230.2145	166.9827	159.6191	94.0627	78.7900
	6~14	241.1834	86.2959	76.7308	36.8765	26.2848
	14~21	12.7370	6.9785	4.2574	3.6042	2.2976
	21~38	5.3149	2.6509	1.2007	1.4969	0.8685
	38~70	0.2734	0.0907	0.0440	0.0523	0.0270
	70~	0.0138	0.0014	0.0011	0.0014	0.0011
NEG Strip	4~6	8389.4805	998.3462	130.7623	-	-
	6~14	1294.5216	261.9393	69.0638	-	-
	14~21	33.0761	7.4897	3.0998	-	-
	21~38	6.0442	1.3323	0.5051	-	-
	38~70	0.0000	0.0051	0.0057	-	-
	70~	0.0000	0.0000	0.0008	-	-

SOKENDAI

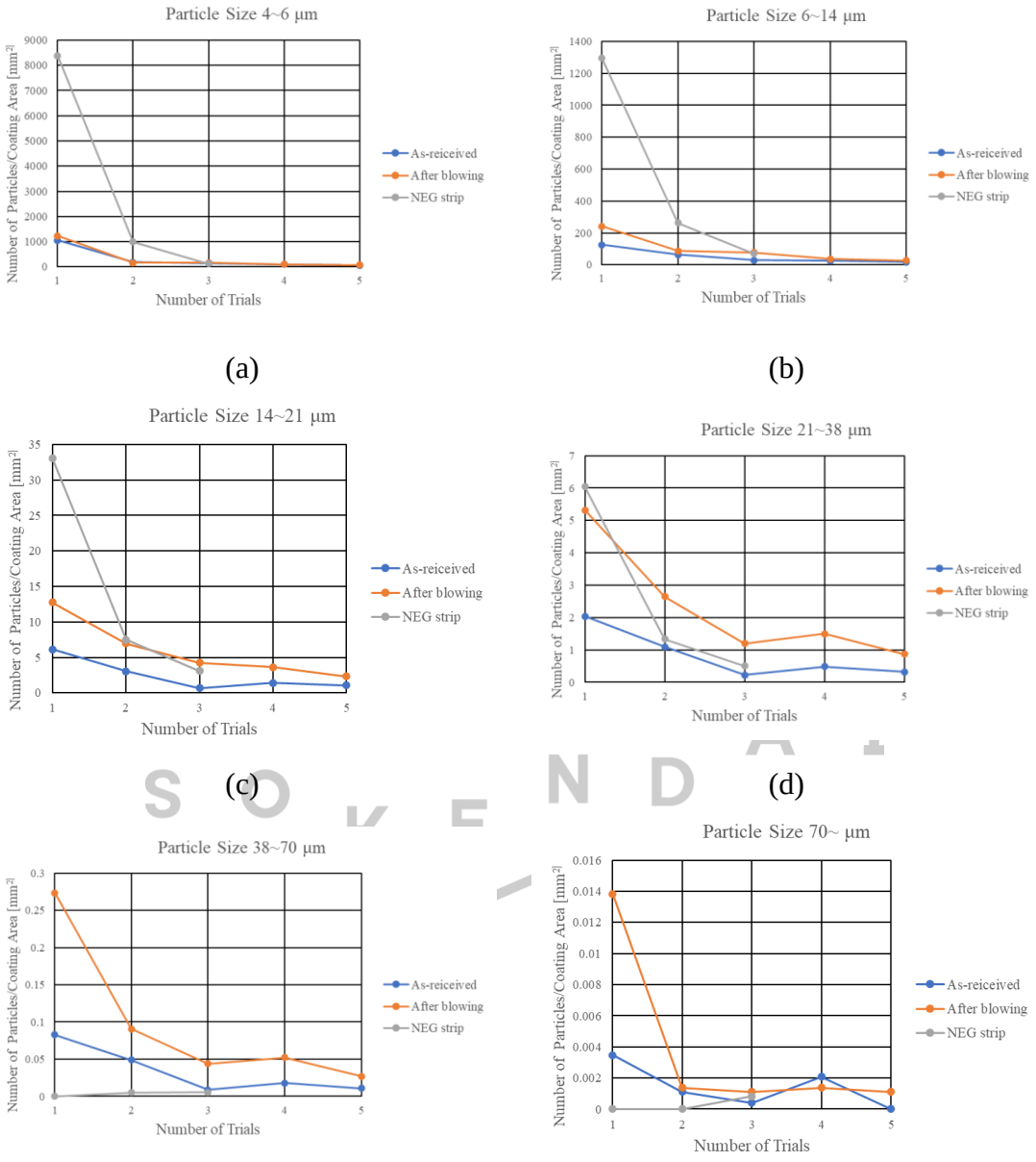

Figure 5-11: Dust count divided by coating areas [mm^2] of different sizes as a function of the number of trials

5.2.4 Surface Resistance

Table 5-5 summarizes the parameters used for Q factor calculation, the conductivity at 5.044 GHz, and the surface resistance of each sample. In addition, two metals [Ti and stainless steel (SUS304)] with similar conductivities to the T.S. coating are also listed [62, 63]. The order of electrical conductivity was SUS304 < T.S. coating ≤ Ti < Al < Cu. Compared with polished copper, the conductivity of the T.S. coating fell by more than

one order of magnitude; this can be attributed to the lamellar microstructure and semi-conducting cuprous oxide (Cu_2O).

However, the conductivity of the T.S. coating was still comparable to that of Ti and slightly higher than that of SUS304. Typically, the accelerator beam pipe using titanium or SUS304 is electroplated with a layer of copper as the inner coating, to reduce the impedance [64]. The impact of the impedance of T.S. coatings is discussed in the next chapter.

Table 5-5: Parameters for Q-factor calculation, conductivity at 5.044 GHz, and surface resistance for each sample

Sample	Γ_{wire1}	Γ_{wire2}	Q_L	Q_0 (calculated)	Temp. [℃]	Q_0 (@ 20 ℃)	σ@5.044 GHz [S/m]	$R_S = \sqrt{\frac{\pi\mu_0 f}{\sigma}}$ [Ω]
Polished Cu	0.9117	0.9247	30500	33102	24.3	32543	5.9E+07	1.8E-02
Machined Al	0.9210	0.9354	27630	29689	24.5	29168	3.3E+07	2.5E-02
GBB Al	0.9435	0.9506	19900	20982	24.7	20598	6.8E+06	5.4E-02
T.S. coating	0.9622	0.9683	13650	14133	24.5	13883	1.9E+06	1.0E-01
Ti [62]							2.4E+06	9.2E-02
SUS304 [63]							1.5E+06	1.2E-01

SOKENDAI

5.2.5 Adhesive Strength

According to *JIS H 8402*, if the rupture surface satisfies any of the following conditions, the measurement is valid:

a) Coating completely detached from Block A
b) Complete peeling between coatings

Figure 5-12 shows all samples after the adhesive strength measurements. For T.S. coated samples, all coatings on Block A were completely peeled off (Situation a). For electroplating copper samples, all coatings were divided into two (Situation b). Therefore, every result was valid. Table 5-6 lists the T values and their averages for each measurement of the two samples. The average T values were 27.17 MPa for the electroplated copper coating and 29.17 MPa for the T.S. coating, which were comparable. Therefore, it can be assumed that the adhesive strength of the T.S. coating can be applied in accelerators.

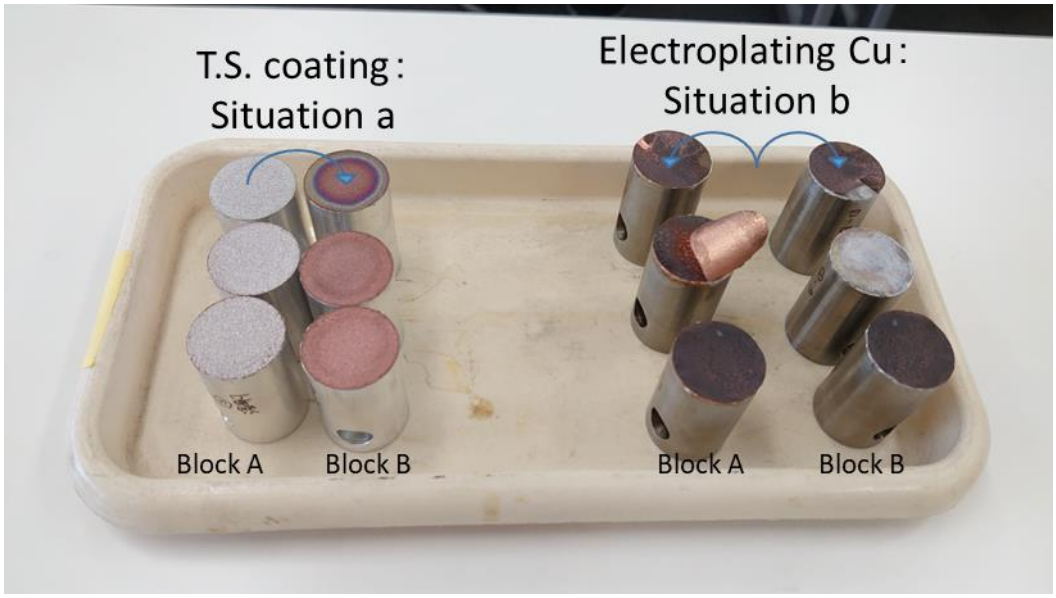

Figure 5-12: All samples after adhesive strength measurements

Table 5-6: *T* values and their averages for each measurement of all samples

Sample	T (MPa) Sample 1	Sample 2	Sample 3	Average
Electroplating Cu	19.66	34.98	26.86	27.17
T.S. coating	20.74	30.62	36.14	29.17

SOKENDAI

Chapter 6

Advanced Discussions

6.1 Dependence of SEY Properties on Surface Structure

From the XPS analysis in Section 5.1.5, the surface compositions of all thermal spray samples after conditioning were found to be similar; hence, the difference in SEY properties is expected to arise from the difference between surface structures.

6.1.1 Roughness Parameter Results

Table 6-1 shows the roughness parameters of the T.S.-coated samples at magnifications of 20×, 50×, and 150×. The parameters related to the longitudinal depth (i.e., *Sa*, *Sq*, and *Sz*) were of the same order of magnitude at different magnifications; however, the parameters (i.e., *Spd* and *Sdr*) related to the lateral width (i.e., sampling interval) varied considerably under different magnifications and could even differ by a factor of more than 10. This implies that the measurement method was insufficient; that is, the sampling interval was larger than the typical periodicity of the T.S. coating surface.

From the SEM image, it can be found that the thermal spray surface was a mixture of terrains of different scales. Therefore, under different magnifications, the microscope saw structures of different levels. This inference again supports the claim that it is difficult to quantify the roughness parameters of the thermal spray surface using existing microscope technologies.

SOKENDAI

Table 6-1: Roughness parameters of T.S.-coated samples at magnifications of 20×, 50×, and 150×

	Sa [μm]			*Sz* [μm]			*Sq* [μm]			*Spd* [mm^{-2}]			*Sdr*		
Magnification	20	50	150	20	50	150	20	50	150	20	50	150	20	50	150
S_STD	5.10	4.58	4.30	61.10	49.81	30.19	6.67	6.18	5.47	37239	201394	1427844	0.57	0.85	2.86
S_GBB_LT	12.35	10.91	10.45	95.81	83.21	53.23	15.34	13.61	12.89	55383	217149	1653575	1.93	3.74	17.66
Al_STD	5.55	4.70	2.51	48.95	49.48	20.52	7.00	6.19	3.176	21671	192581	1574393	0.57	1.12	1.18
Al_LT1	10.61	11.49	6.64	78.59	60.98	42.60	13.16	13.59	8.12	45978	206218	1351210	1.29	2.20	9.20
Al_LT2	11.69	10.74	7.33	95.04	76.85	62.28	14.48	13.54	9.44	47373	415371	1388014	1.91	8.39	34.83
OBP_H1	9.69	7.82	4.59	87.98	56.42	33.65	12.28	9,71	5.73	18039	200014	2096568	0.78	1.50	4.13
OBP_H2	7.61	6.34	5.60	62.58	48.33	37.12	9.76	7.96	7.16	14633	355996	2399862	0.70	2.62	8.38
OBP_H3	5.14	4.39	3.70	43.78	34.61	26.70	6.43	5.50	4.63	15729	434417	2713084	0.62	2.32	7.63
OBP_H4	7.38	5.49	4.72	48.75	41.53	31.20	8.96	6.80	5.72	13858	193851	1947275	0.86	1.35	6.89
OBP_H5	9.75	8.79	4.35	72.03	52.02	29.15	11.97	10.69	5.58	10505	210020	1929711	0.86	1.60	4.67
OBP_S1	5.93	4.89	3.53	59.46	41.65	29.18	7.48	6.22	4.34	12939	201755	2145045	0.68	1.29	2.77
OBP_S2	5.70	5.01	4.74	58.39	41.22	28.76	7.25	6.48	5.90	15137	186791	2180620	0.63	1.37	4.35
OBP_S3	6.09	4.79	3.10	53.46	42.58	24.00	7.81	5.99	3.89	11141	184877	2551277	0.64	1.24	2.28
OBP_S4	5.91	4.71	4.17	58.70	41.13	31.60	7.39	5.84	5.20	25863	182644	2255913	0.77	1.38	4.53
OBP_S5	7.54	5.84	3.29	52.89	45.85	28.13	9.31	7.04	4.14	25875	193706	1331172	0.69	1.29	2.59
AC1_1	6.45	5.06	2.48	63.63	42.30	21.47	8.06	6.45	3.13	22109	185396	2584909	0.62	1.17	2.94
AC1_2	5.90	4.94	3.95	53.24	47.00	28.86	7.51	6.59	5.03	24470	191572	2076382	0.57	1.11	5.78
AC1_4	6.97	4.79	3.84	61.06	38.75	24.91	8.69	6.13	4.64	28549	184963	1779173	0.70	1.13	4.76
AC1_5	6.20	5.45	4.02	59.22	38.90	26.68	7.86	6.68	4.89	34347	180363	1494722	0.92	1.15	5.00
AC2_1	5.82	5.99	4.51	63.12	47.05	33.03	7.31	7.52	5.63	22278	196607	2532557	0.61	1.32	9.04
AC2_2	6.53	6.47	7.28	63.36	57.50	38.38	8.21	8.44	8.50	21098	250777	2046715	0.63	1.71	13.11
AC2_4	6.50	5.04	4.25	63.03	36.69	25.06	8.18	6.14	5.09	25562	172902	2182278	0.66	1.23	3.65
AC2_5	6.68	6.53	4.45	66.67	53.19	27.14	8.45	8.08	5.27	23738	235505	1974214	0.63	1.77	6.46
AC3_2	6.87	5.91	3.88	61.93	57.15	26.17	8.69	7.64	4.70	29918	189193	1960014	0.80	1.55	8.29
AC3_3	6.11	5.13	3.21	71.90	44.19	26.79	7.88	6.55	4.04	24013	222511	1785679	0.72	0.96	2.57
AC4_2	6.72	6.08	4.18	64.72	46.39	27.70	8.47	7.60	5.08	12042	222980	2429074	0.82	1.35	4.82
AC5	7.40	6.32	4.86	63.29	55.74	36.38	9.28	8.13	6.08	10966	227312	2991248	0.99	1.65	5.53
AC6	6.69	6.18	6.35	53.28	45.48	34.28	8.36	7.53	7.60	17816	325680	2226066	0.80	2.50	10.31
BP-2	6.93	5.66	4.51	72.28	48.95	34.02	9.09	7.15	5.59	17658	216909	1737758	0.59	1.51	4.54
BP-3	7.34	5.61	4.23	66.69	46.95	36.07	9.22	7.09	5.22	16107	191126	2579101	0.75	1.31	13.64
BP-4	6.01	4.46	2.85	66.55	34.31	21.93	7.75	5.52	3.62	18826	165347	1940642	0.63	1.06	4.32

SOKENDAI

6.1.2 Dependence on Roughness Parameters

In the Master's report, VBA was used to simulate the rectangular, triangular, and trapezoidal grooves and protrusions; the following conclusions were obtained:

In the case of identical surface patterns:

1. The groove had the same SEY profile (δ vs. incident electron energy) as the protrusions with identical patterns (e.g., triangular and trapezoidal protrusions have different patterns) and size parameters (Sz, θ, width, etc.).
2. SEY did not vary with the scale of the surface structure.
3. δ_{max} was inversely proportional to Sdr (developed area ratio), and the proportional coefficient differed under different patterns.

In this study, the more accurate simulation program CST was used to re-examine these conclusions. CST Studio Suite is a computational electromagnetics tool developed by Dassault Systèmes Simulia. It has been applied in many fields, including industries (telecommunications, defense, automotive, aerospace, electronics, and medical equipment), accelerator physics, biological electromagnetics, nanotechnology, and metamaterials. The advantages of CST are that particle trajectories are more accurate, and the measured surface can be drawn using other 3D softwares, making it easier to input complex structures. The SEY model in CST is based on the Furman's model described in Chapter 2.

SOKENDAI

Based on the methods in the Master's report, the following surfaces were selected for inputting parameters to the CST:

1. Triangular groove/protrusion: Sz = 100, 200, 300 μm; θ = 60°, 75°, 80° [Fig. 6-1(a)]
2. Trapezoidal protrusion: Sz = 200, 300 μm; θ = 30°, 45°, 60°, 80° [Fig. 6-1(b)]

The surface SEY profile inputted here was that of pure copper, as listed in Table 2-1. Figure 6-1(c–d) shows typical examples of the triangular grooves and protrusions with identical profiles. The shape of the primary electron beam in the SEY simulation was a square with a side equal to an integer multiple of the groove period, to avoid errors.

Figure 6-1(e–f) shows the simulation results for CST and compares them with the VBA results in the Master's report. The CST results were essentially consistent with the previous results for VBA (as indicated in the figures); however, a slight difference

remained. The possible reasons for the deviation may be that the CST can produce a more accurate secondary electron emission point; alternatively, the fixed primary electron size in previous VBA simulations might lead to some errors. Nevertheless, the conclusions of this section matched those in the Master's report.

The next step is to identify the same trend in the measured values of thermal spray surfaces. In the Master's report, no clear correlation was observed between δ_{max} and *Sdr* for thermal spray surfaces. There were two possible reasons for this:

1. The surface pattern (e.g., “triangular” groove and “trapezoidal” groove are different surface patterns) of each thermal spray sample was different, so their results were not on the same line.
2. The roughness measurement was insufficiently accurate.

Reason 1 constitutes an inherent limitation attributable to the complex and difficult-to-control patterns of the thermal spray surface. However, we can try to improve the measurement accuracy of the roughness parameters. This can be attempted in two ways. The first is to construct some large-scaled machined-groove samples, to obtain the accurate roughness parameters. Hence, groove samples with three different angles (see Fig. 4-4) were made.

SOKENDAI

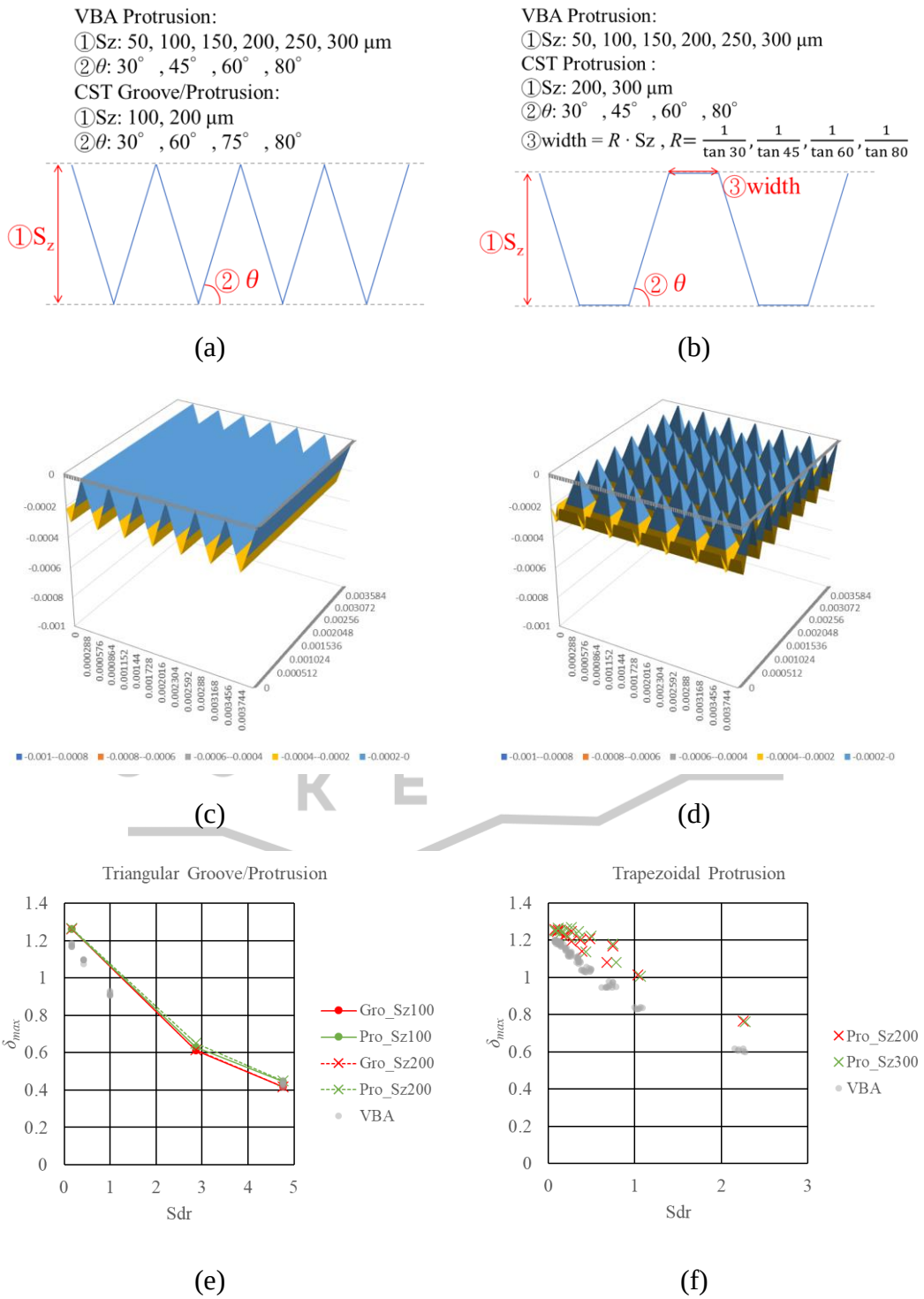

Figure 6-1: (a–b) Parameters of the (a) triangular and (b) trapezoidal grooves and protrusions; (c–d) examples of the triangular (c) grooves and (d) protrusions; (e) simulated δ_{max} for triangular grooves and protrusions as a function of *Sdr*; and (f) simulated δ_{max} for trapezoidal protrusions as a function of *Sdr*

At the same time, we inputted the same triangular groove surfaces into CST and compared the simulation results with the measured values. The plot in Fig. 6-2 shows the simulated and measured δ_{max} as a function of the angle θ, and the tables on the right-hand side show the groove period λ and *Sdr* corresponding to the simulated surfaces (calculated values) and real groove surfaces (designed values in Fig. 4-4). The results in the plot show that the experimental values were close to the simulated values, though they were a little closer to the simulated values for the blunter groove (R = 0.1 mm). From the dimensional design values of the real groove surfaces, although their R was marked as 0.05 mm, their values of λ were closer to the calculated values when R = 0.1 mm. However, in any case, the results in the plot of Fig. 6-2 were still similar.

This implies that if the *Sdr* for a surface is accurate, we can use the CST simulation to predict its SEY property; furthermore, the trend of δ_{max} being inversely proportional to *Sdr* can also be obtained.

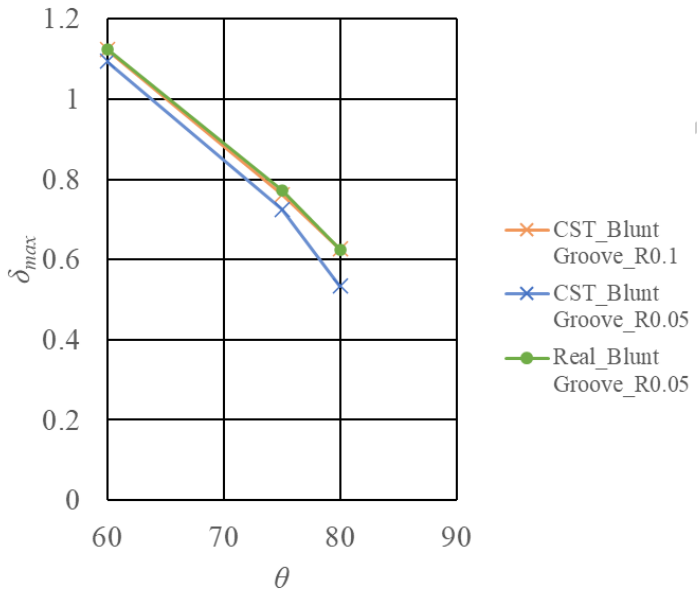

Calculated values of surfaces in the simulation (Sz = 1.88 mm)

α	θ	R	λ	*Sdr*
20	80	0.1	0.80	4.04
30	75		1.12	2.66
60	60		2.23	1.03
20	80	0.05	0.73	4.37
30	75		1.06	2.76
60	60		2.20	1.02

Designed values of real groove surfaces in Fig. 4-4

α	θ	R	λ
20	80	0.05	0.83
30	75		1.16
60	60		2.29

Figure 6-2: Simulated and experimental δ_{max} of blunt triangular grooves as a function of θ. The tables on the right-hand show the groove period λ and *Sdr* corresponding to the simulated surfaces (calculated values) and real groove surfaces (designed values in Fig. 4-4)

On the other hand, we used a laser microscope (with a higher precision than that in the Master's report) to measure the roughness parameters of the microscopic thermal spray surfaces. A rough surface with a microscopic and complex surface structure (e.g., a thermal spray surface) is impossible to copy; thus, it cannot be directly reproduced by simulations. Therefore, for thermal spray samples, we can only compare the measured δ_{max} and roughness parameters with the trends shown in Fig. 6-1 and 6-2.

6.1.3 δ_{max} vs. Sdr for Bead-shaped Surfaces

Here, we consider those samples exhibiting a markedly different surface from the other samples in the SEM images. As described in Section 4.1.1, the samples denoted LT represent the removal of H_2 from the plasma source, to reduce the plasma temperature and maintain the bead shape of the copper powder. Furthermore, Sample Al_LT2 reduced the electric arc current with respect to Al_LT1; hence, the power from the plasma was further reduced. We maintained the bead shape to increase the complexity of the surface and try to further reduce the SEY.

Figure 5-3(1–4) and (5–10) show that the LT series samples did form a bead-shaped surface; of these, Al_LT2 was the most obvious. The increase in granularity was also reflected in the roughness parameter *Sdr*.

SORENDAI

Table 6-2 summarizes the results in Table 6-1 for these samples. *Sdr* increased with granularity. Although the measured value of *Sdr* varied with magnification (as described before), the increasing trend of *Sdr* was the same at each magnification; hence, the increasing trend of *Sdr* was still reliable.

However, it can be observed in Table 6-2 that surfaces with higher *Sdr* did not achieve lower δ_{max}. The samples S_STD and Al_STD, which did not have bead-shaped surfaces, instead exhibited the lowest δ_{max}. Moreover, when the electric arc current was reduced to 300 A (which was the case for Sample Al_LT2), the coating thickness was only 22 μm, which means that the unmelted copper powder could not be well attached to the surface of the substrate.

Table 6-2: Comprehensive results for thermal spray samples with bead-shaped surfaces

Sample	Substrate	Coating thickness (μm)	δ_{max}	E_{max} (eV)	*Sdr* 20×	*Sdr* 50×	*Sdr* 150×	Note
S_STD [31]	Machined Cu	208	0.96	650	0.57	0.85	2.86	
S_GBB_LT [31]	GBB Cu	109	1.06	600	1.93	3.74	17.66	
Al_STD	GBB Al	84	0.88	750	0.57	1.12	1.18	Electric arc current: 500 A
Al_LT1	GBB Al	108	0.98	550	1.29	2.20	9.20	Electric arc current: 500A
Al_LT2	GBB Al	22	1.20	550	1.91	8.39	34.83	Electric arc current: 300A

6.1.4 δ_{max} vs. Sdr for All Thermal Spray Surfaces

Next, we plotted δ_{max} with respect to *Sdr* for all thermal spray samples in this study, as shown in Fig. 6-3(a), (c), and (e). The results were the same as in the Master's report; that is, it was hard to find any trends. Furthermore, we tried to use $Sa\sqrt{Spd}$ (which had a similar meaning to *Sdr*) as the horizontal axis (see Section 6.5 for detailed calculation), as shown in Fig. 6-3(b), (d), and (f). However, the results were unchanged.

In the reference for copper laser ablation surfaces, it was also found that the deepest groove surface did not achieve the lowest δ_{max} [65]. For technologies with high-temperature melting/evaporating materials (e.g., thermal spraying or laser ablation), the surface was too complex, and comprised a mix of terrains of different scales. First, compared to machined grooved surfaces, it was difficult to control the pattern; secondly, the roughness parameters varied with the magnification, as described in Section 5.3; thus, the roughness parameters of the thermal spray surfaces, as measured by existing microscopy technologies, were unreliable. However, if the measurement method for *Sdr* can be improved [e.g., by using reflectivity, etc. (further research is required)], then *Sdr* could still be used to predict δ_{max}, as described in Section 6.1.2. Even if the same correlation between δ_{max} and *Sdr* as in the simulation could not be found in the measurement, this does not change the fact that the δ_{max} of the T.S. coating on the beam pipe after conditioning was stable between 0.7 and 0.8, which was relatively low for existing low-SEY coatings.

SOKENDAI

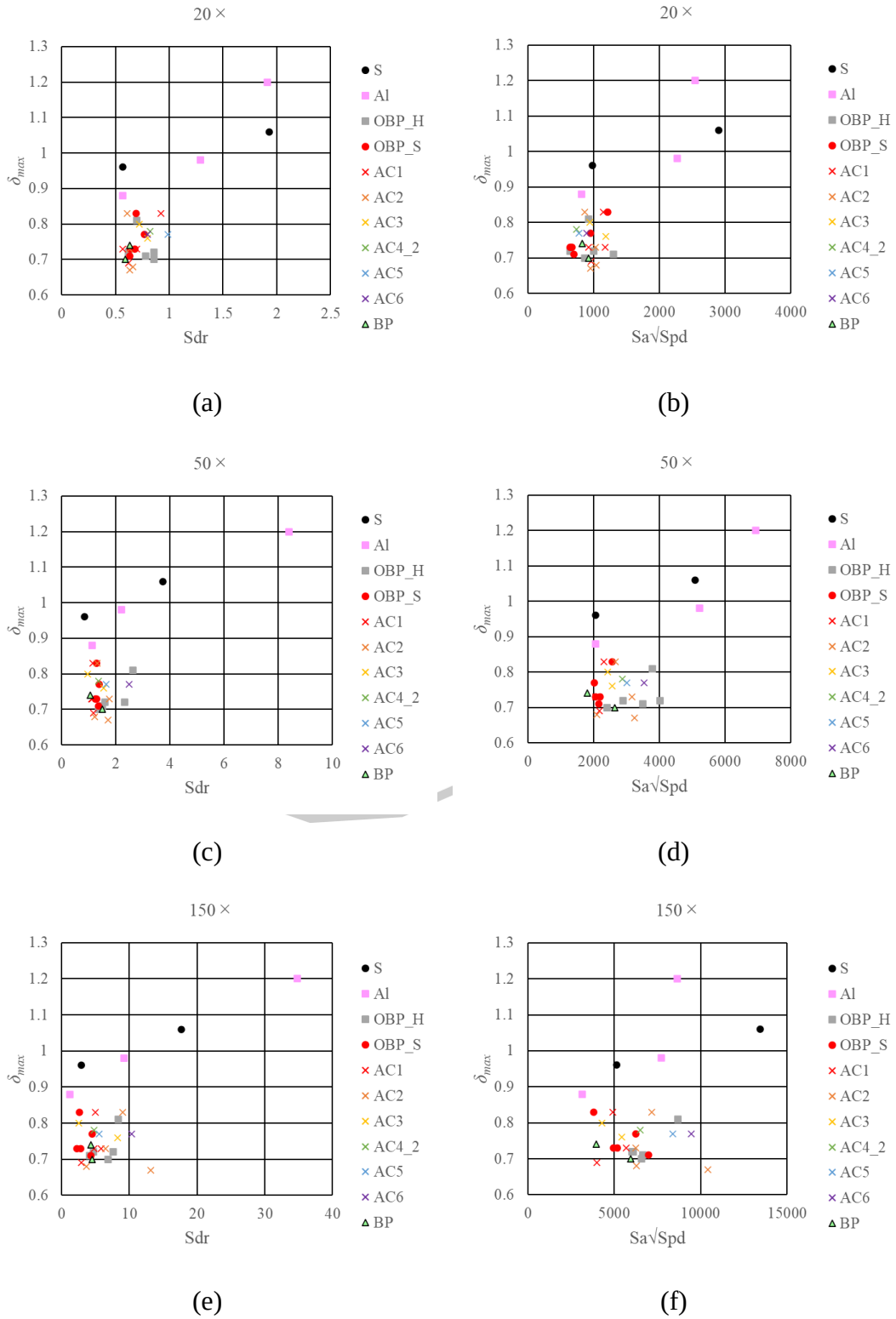

Figure 6-3: Experimental δ_{max} for all thermal spray samples as a function of *Sdr* or $Sa\sqrt{Spd}$ under different magnifications

6.2 Impact of Resistive-wall Impedance

The measured conductivity and surface resistance of the T.S. coating at a fixed frequency (5.044 GHz) are presented in Section 5.2.4 (Table 5-5). This section further discusses the effects of T.S. coatings in accelerators (i.e., the impedance as a function of frequency). The coating is attached to the beam pipe wall; hence, its impedance is referred to as resistive-wall (RW) impedance. The RW impedance can be separated into longitudinal and transverse components, where the longitudinal RW impedance relates to the heat load, and the transverse RW impedance relates to the coupled-bunch instability. This section mainly refers to Ref. [66] to discuss the longitudinal RW impedance of the T.S. coating and the corresponding heating power.

6.2.1 Heating without Coating

The longitudinal RW impedance of a flat or circular metal pipe with a pipe wall thicker than the skin depth δ is approximately given by

$$Z_l(\omega) = \frac{\omega Z_0 \delta(\omega) L}{4\pi bc}\{sgn(\omega) - i\}, \qquad \text{(Eq. 6-1)}$$

$$\delta(\omega) = \left(\frac{2}{\sigma_c \mu_0 |\omega|}\right)^{1/2}. \qquad \text{(Eq. 6-2)}$$

Here, ω, c, b, L, σ_c, μ_0, and Z_0 are the angular frequency, velocity of light, inner radius (for a circular pipe) or half gap (for a flat pipe), length, electric conductivity and permeability of the pipe, and characteristic impedance of a vacuum. The permittivity and permeability of the metal are assumed to equal those of the vacuum. The heating power of the RW pipe is given by

$$P_{RW} = k_{loss} {Q_b}^2 f_b = \frac{k_{loss} {I_{total}}^2}{f_b}, \qquad \text{(Eq. 6-3)}$$

where k_{loss}, I_{total}, Q_b, and f_b are the loss factor, total stored current, bunch charge, and bunch frequency (the number of bunches passing through a fixed point per second). For a Gaussian bunch with a bunch length of time σ_t, the loss factor is expressed as

$$k_{loss} = \frac{1}{\pi}\int_0^\infty Re\{Z_l^{eff}(\omega)\}d\omega, \qquad \text{(Eq. 6-4)}$$

$$Z_l^{eff}(\omega) \equiv Z_l(\omega) \cdot \exp\{-(\sigma_t \omega)^2\}. \qquad \text{(Eq. 6-5)}$$

Here, Z_l^{eff} is the longitudinal effective impedance, which includes the effect of the longitudinal bunch profile. The loss factor for the impedance of Eq. (6-1) was obtained using Eqs. (6-4) and (6-5) and given by

$$k_{loss} = \frac{Z_0}{8\pi^2 bc}\Gamma\left(\frac{3}{4}\right)\left(\frac{2}{\sigma_c \mu_0}\right)^{1/2} {\sigma_t}^{-3/2}, \qquad \text{(Eq. 6-6)}$$

where Γ is the gamma function. For example, the heating power per unit length is calculated for the circular Al pipe with an inner radius of b = 45 mm:

$$\frac{P_{RW}}{L} = 43.07 \text{ [W/m] (Al pipe).} \quad \text{(Eq. 6-7)}$$

The designed parameters for SuperKEKB LER were used in the calculation of Eq. (6-7) [1]. The electric conductivity of aluminum was 3.78×10^7 Ω^{-1}m^{-1} and the bunch length σ_t was assumed to be 20 ps (i.e., 6 mm). The total stored current I_{total} and the bunch frequency f_b were 3.6 A and 249 MHz, and the bunch number k_b was 2500.

6.2.2 Heating with T.S. Coating

The longitudinal RW impedance of a two-layer circular metal pipe can be used to evaluate the effects of T.S. coatings on the RW heating of a vacuum pipe; it can be expressed analytically as [66]

$$Z_\ell(\omega) = \frac{-iL}{2\pi\epsilon_0 bc\left\{\left(\frac{\omega}{\lambda_1 c}+\frac{\lambda_1 c}{\omega}\right)\alpha_{l2}-\frac{b\omega}{2c}\right\}}, \quad \text{(Eq. 6-8)}$$

$$\alpha_{l2} = \frac{J_1(\lambda_1 b)+\kappa N_1(\lambda_1 b)}{J_0(\lambda_1 b)+\kappa N_0(\lambda_1 b)},$$

$$\lambda_{1,2} = \frac{i+sgn(\omega)}{\delta_{1,2}}, \quad \delta_{1,2} = \left(\frac{2}{\sigma_{1,2}\mu_0|\omega|}\right)^{1/2},$$

$$\kappa = \frac{\left(\frac{\omega}{\lambda_1 c}+\frac{\lambda_1 c}{\omega}\right)H_0^{(1)}(\lambda_2(b+d))J_1(\lambda_1(b+d)) - \left(\frac{\omega}{\lambda_2 c}+\frac{\lambda_2 c}{\omega}\right)H_1^{(1)}(\lambda_2(b+d))J_0(\lambda_1(b+d))}{\left(\frac{\omega}{\lambda_2 c}+\frac{\lambda_2 c}{\omega}\right)H_1^{(1)}(\lambda_2(b+d))N_0(\lambda_1(b+d)) - \left(\frac{\omega}{\lambda_1 c}+\frac{\lambda_1 c}{\omega}\right)H_0^{(1)}(\lambda_2(b+d))N_1(\lambda_1(b+d))}.$$

Here, b, L, d, $\sigma_{1,2}$, and $\delta_{1,2}$ are the inner radius and length of the pipe, the thickness of the inner layer, and the electric conductivities and the skin depths of the inner and outer layers, respectively. The thickness of the outer layer was assumed to be infinite or thicker than the skin depth. J_0, J_1, N_0, N_1, $H_0^{(1)}$, and $H_1^{(1)}$ are 0th-order and 1st-order Bessel functions of the 1st and 2nd kinds and 0th-order and 1st-order Hankel functions of the 1st kind, respectively. In this study, the inner and outer layers corresponded to the T.S. coating and Al pipe.

Figure 6-4 shows the real part of the longitudinal effective impedance of T.S.-coated Al pipes (of different coating thicknesses) and bare Al pipe, as calculated from Eqs, (6-1), (6-5), and (6-8). The DC electric conductivity of the T.S. coating was assumed to be 1.9×10^6 Ω^{-1}m^{-1}, and the bunch length was 20 ps (i.e., 6 mm).

These results show that the longitudinal impedance of the 100 μm-thick T.S.-coated Al pipes deviated by ~1 MHz from that of the pure Al pipe (d = 0 μm) and approached

that of the pure T.S. pipe ($d \to \infty$) at ~10 MHz. To render the effect of the T.S. coating's longitudinal impedance negligible in SuperKEKB LER, the coating thickness must be reduced below 10 μm.

The size of the copper powder used for spraying was ~50 μm, and the coating thickness for one scan was ~10 μm; this does not completely cover the substrate surface. If the powder size is further reduced, the fluidity may deteriorate, and it may be difficult to load the powder into the spray gun. Therefore, we recommend reducing the surface oxide layer generated during spraying (e.g., vacuum spraying) and also the coating thickness by as much as possible, whilst ensuring complete coverage of the surface.

Table 6-3 shows the calculated heating power per unit length for all curves in Fig. 6-4. For the current T.S. coating, the heating power was ~192 W/m. The average power line density generated via SR, as calculated from the design parameters of SuperKEKB LER, was ~600 W/m, and the peak power line density was ~2300 W/m [67]. Note that the surface irradiated by SR was cooled by water located just behind it. On the other hand, the power contributed by the RW impedance was dissipated across the entire beam channel without cooling water. Therefore, although the heat load produced by the T.S. coating was lower than that produced by SR, it was still considerable. In future, a thermometer should be attached to the T.S.-coated beam pipe, to observe the temperature during beam operations.

SOKENDAI

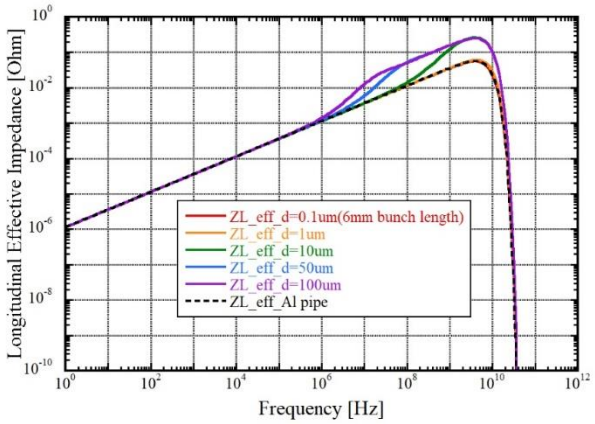

Figure 6-4: Longitudinal effective impedance per unit length of T.S.-coated Al pipes (d = 0, 0.1, 1, 10, 50, and 100 μm) for b = 45 mm and bunch σ_t = 20 ps

Table 6-3: Calculated heating power per unit length for all curves in Fig. 6-4

T.S. coating thickness	k_{loss}	P_{RW}/L [W/m]
d = 0.1 μm	9.97E+08	43.11
d = 1 μm	9.98E+08	48.61
d = 10 μm	1.13E+09	191.37
d = 50 μm	4.45E+09	192.35
d = 100 μm	4.45E+09	192.35
Al pipe	9.97E+08	43.07

6.3 Measured Electron Densities

The δ_{max} of the T.S. coatings and TiN grooves should be lower than that of TiN; however, numerically, they exhibit slightly higher electron densities. For T.S.-coated beam pipes, the most likely reason is that, as mentioned earlier, the aluminum mesh screen in front of the electron monitor is uncoated, and its high δ_{max} may result in an overall increase in the measured signal.

It is worth noting that the electron density increased approximately in proportion to the bunch number, especially for the T.S.-coated and TiN groove beam pipes. The possible reasons are discussed below using PyECLOUD simulations.

The measured electron densities were analyzed using PyECLOUD (described in Section 5.1.6). The main variable parameters were δ_{max}, I_{bunch}, and bunch spacing in the RF bucket (hereinafter referred to as "*RF*"). Note that in the simulations, the radius of the observed cylinder r was a constant. However, as shown in Eq. (3-30), the r used to calculate the electron density (n_e) in the experiment was inversely proportional to n_b for a fixed I_{beam}.

Each monitor has its own characteristics (e.g., structure, cabling, current monitor, power supply, etc.). In fact, the backgrounds (i.e., the electron signal without the beam) differ for each monitor. The positional relationship between the mesh screen of the monitor port, the holes of the monitor, and the beam orbit position, are not exactly identical for each season and test beam pipe.

6.3.1 Estimation of δ_{max} using Simulation

First, we tried to estimate the actual SEY of the inner wall for the T.S.-coated beam pipe, using simulations. We set a bunch spacing of 3.96 *RF* (which approximately

corresponds to n_b = 1272) and drew two data points for different δ_{max} values within the same linear current density (I_d) range as Fig. 5-8(f); the results are shown in Fig. 6-5. Then, the simulation results were compared with the yellow dots in Fig. 5-8(f).

It can be observed that the n_e values did not increase rapidly with respect to I_d when $\delta_{max} \leq 1.0$ (where the effect of photoelectrons was dominant). Furthermore, the exact estimation of δ_{max} was challenging considering the measurement uncertainty of our monitors in the low n_e region. However, the slopes of measured and simulated n_e can still be compared within a reliable region. The slope of the measured n_e in Fig. 5-8(f) was ~1.8×10^{12} (yellow); meanwhile, the slopes in Fig. 6-5 were ~9.4×10^{11}, 1.3×10^{12}, 2.1×10^{12}, and 4.8×10^{12} for δ_{max} = 0.5, 0.7, 0.9, and 1.1, respectively. Thus, it can be inferred that the δ_{max} of the T.S. coating should be between 0.7 and 0.9.

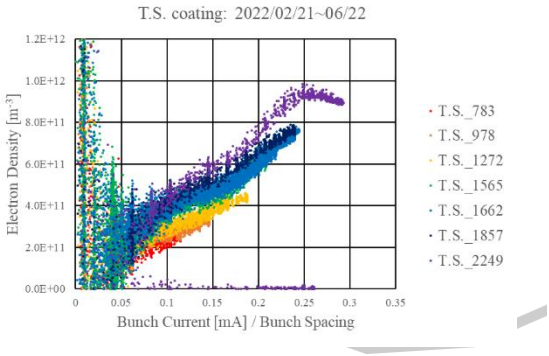

Figure 5-8(f): Electron densities in the T.S.-coated beam pipe as a function of the current linear density

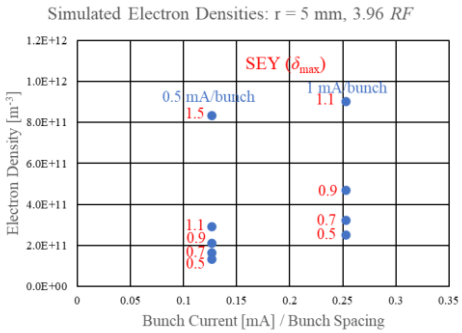

Figure 6-5: Simulated electron densities of different δ_{max} as a function of linear current density I_d

6.3.2 Possible Reasons for Higher Measured Values at Higher Bunch Numbers

We used simulations to explain the phenomena mentioned in Section 5.2.1.1; that is, the electron density in the T.S.-coated and TiN groove beam pipes increased with the bunch number.

6.3.2.1 Difference in the radii used for the estimation

As mentioned above, for the present electron monitor, we assume that I_{beam} is fixed (i.e., I_d is fixed); as a result, the radius r used for the n_e calculation is inversely proportional to n_b.

Figure 6-6 shows the simulated n_e for different δ_{max} values as a function of r under a

fixed I_d. The simulation results indicate that a decrease in r produced an increase in n_e under a fixed I_d. In Fig. 5-7(c), the distribution of electrons in the beam pipe approximates an even distribution. However, Fig. 6-6 indicates that the electron density near the beam is slightly higher. Therefore, when n_b increases, r decreases; this may eventually lead to an increase in the calculated n_e.

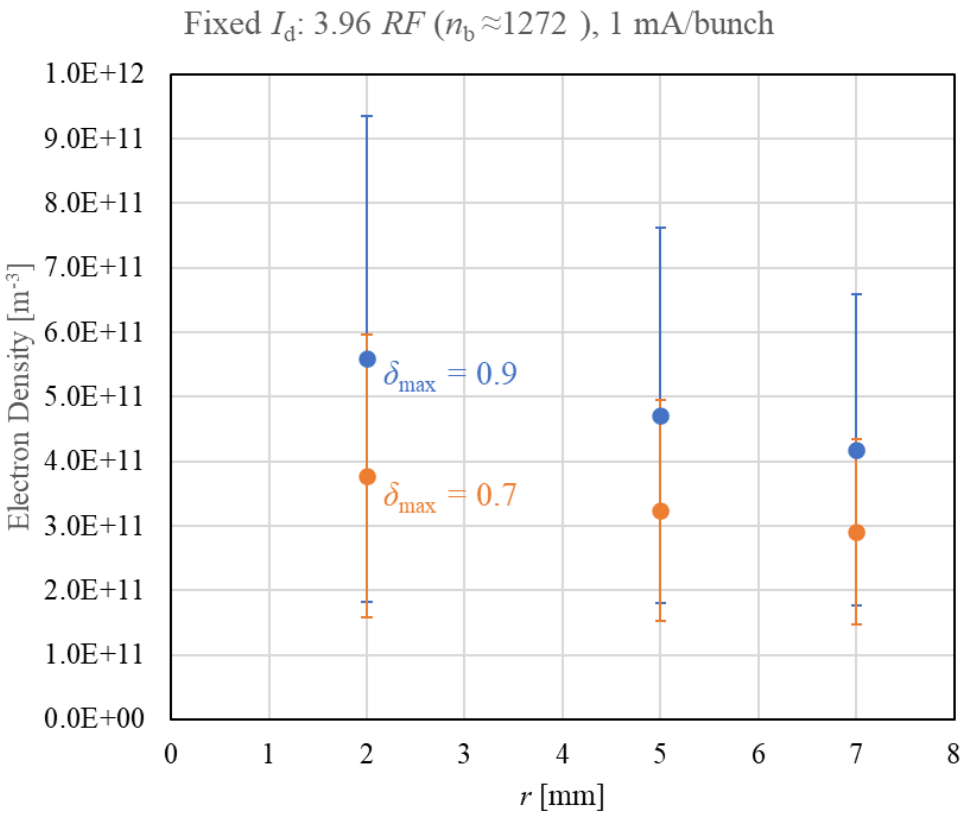

Figure 6-6: Simulated n_e of different δ_{max} as a function of r under a fixed I_d

6.3.2.2 Dependence of measured electron density on bunch current

According to the simulation results, the increase in n_e with respect to n_b most likely indicates that the δ_{max} of the inner wall is small; furthermore, the lower the value of δ_{max}, the more notable this trend is. To explain this inference, the impact of I_{bunch} and RF on n_e should be introduced.

In our simulation for SuperKEKB, when other parameters were fixed, a high I_{bunch} or low RF typically resulted in a high n_e. When I_{bunch} is higher, each bunch can generate more SEs. When a bunch leaves, n_e falls until the next bunch arrives. Therefore, when RF is shorter (i.e., the time interval between SE generation events is shorter), the final equilibrium n_e will be higher.

When $I_d = I_{bunch}/RF$ is fixed (i.e., a vertical line in Fig. 5-8), I_{bunch} becomes proportional to RF, and the two factors exert opposite effects on n_e; hence, the impacts of I_{bunch} and RF upon n_e determine the trend of n_e. When $\delta_{max} > 1$, the number of SEs generated by each bunch is high; thus, the impact of I_{bunch} on n_e will be exceed that of RF. When $\delta_{max} < 1$, the number of SEs generated by each bunch becomes lower, so the influence of RF upon n_e will increase.

Figure 6-7 shows the simulated n_e as a function of δ_{max} for different RF values when I_d was fixed at 0.126 mA bunch^{-1} RF^{-1}. When δ_{max} was high, I_{bunch} had a larger influence upon n_e, so the increased I_{bunch} (i.e., higher RF or lower n_b) produced a larger n_e. When δ_{max} was low, the influence of RF on n_e became greater, so the lower RF (i.e., higher n_b) achieved a higher n_e. This demonstrates the inference made at the beginning of this section. Moreover, the r in the simulation was a fixed value; however, $r \propto 1/n_b \propto RF$ in the electron density measurement. According to Section 6.4.2.1, a smaller r (i.e., smaller RF) results in a higher n_e, so the difference in n_e for $\delta_{max} < 1$ (see Fig. 6-7) will become larger.

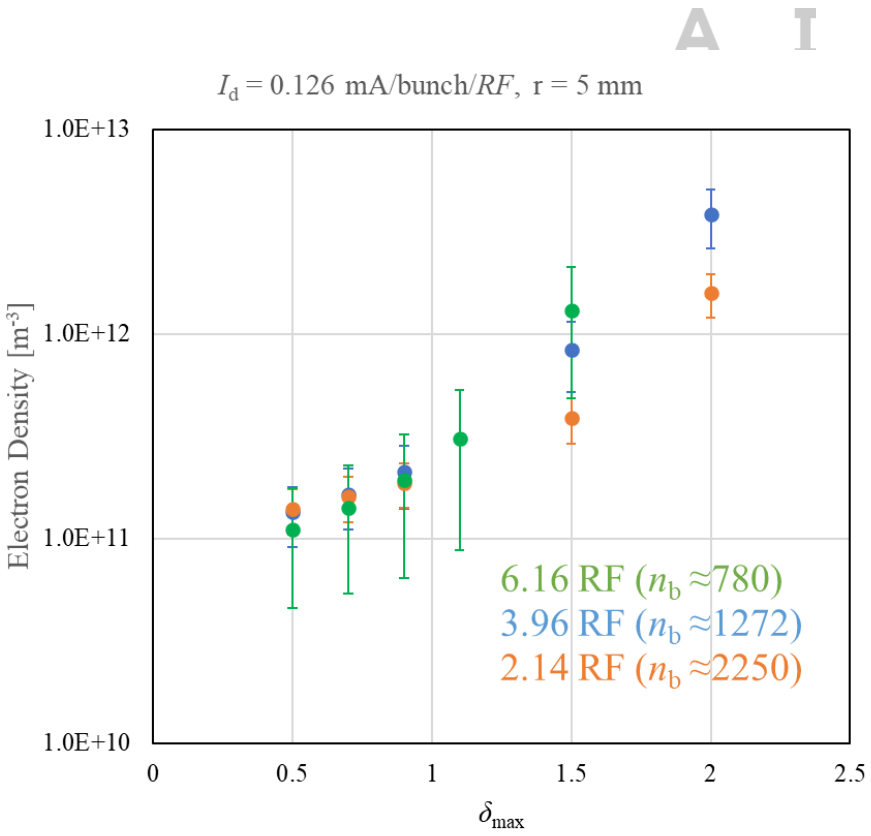

Figure 6-7: Simulated n_e as a function of δ_{max} for different RFs when I_d is fixed at 0.126 mA bunch^{-1} RF^{-1}

6.3.2.3 Noise from electron monitors

One hypothesis is that, for some unknown reason, only Monitors 2 and 3 produced noise, and this noise was proportional to the frequency. This possibility can be confirmed by swapping monitors or beam pipe positions in the near future.

6.3.3 Effect of the Uncoated Al Mesh Screen

Figure 5-9(b) shows the experimental result for B_y at a lower I_d. We found that even when the T.S.-coated beam pipe had an uncoated aluminum screen, the SEY of the T.S.-coated beam pipe's inner wall remained lower than those of the TiN beam pipe and TiN groove beam pipe. However, when I_d increased [as shown in Fig. 5-9(c)], the current ratio of the T.S. coating increased to match that of the TiN groove.

Figure 6-8 shows the simulated n_e as a function of δ_{max} for different I_d values when the bunch spacing was fixed at 3.96 *RF*. From the simulation results, we found that when I_d increased (i.e., a higher I_{bunch}), the n_e of the higher δ_{max} increased more. Therefore, the high δ_{max} of the uncoated aluminum screen contributed more to n_e at a higher I_d.

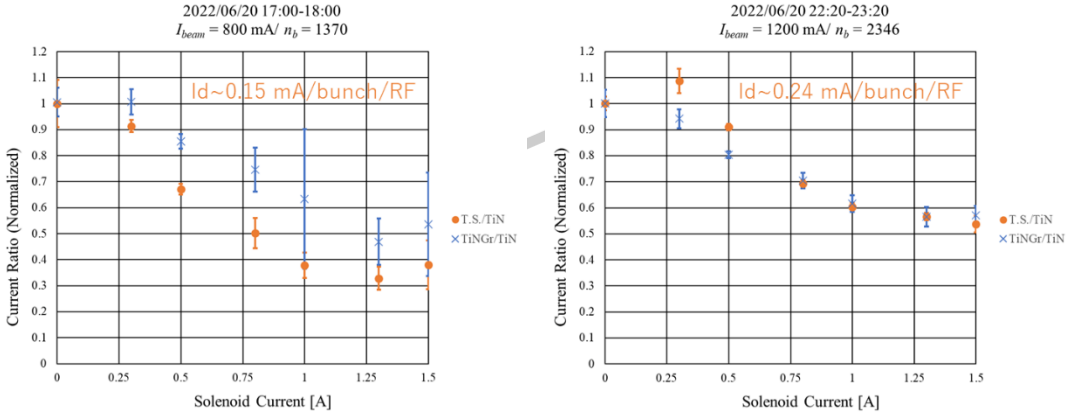

(b) (c)

Figure 5-9: Normalized current ratios $I_{e\_T.S.\ coating}/I_{e\_TiN}$ and $I_{e\_TiN\_groove}/I_{e\_TiN}$ as a function of the solenoid coil current under different beam conditions

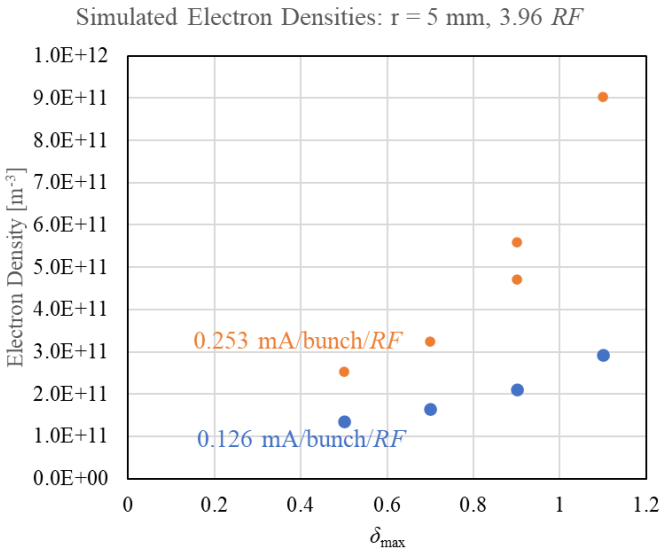

Figure 6-8: Simulated n_e as a function of δ_{max} for different I_d values when the bunch spacing was fixed at 3.96 *RF*

6.4 Appendix: Relation between *Sdr* and $Sa\sqrt{Spd}$

SOKENDAI

Figure 6-9 shows the case for rectangular protrusions. We assume that the *Sa* and *Spd* are known, and the straight surface area inside the dashed blue box is *A*. In the simplest case [i.e., the valley width d_1 is equal to the peak width d_2], the side length of the dashed blue box (= the period of the protrusions) is $1/\sqrt{Spd}$. From the above conditions, *Sdr* can be expressed as

$$\begin{aligned} Sdr &= \frac{Actual\ surface\ area - A}{A} \\ &= \frac{\left\{\left(\frac{1}{Spd} + \frac{1}{2\sqrt{Spd}} \times 2Sa \times 4\right) \times Spd \times A - A\right\}}{A} \\ &= 4 \times Sa \times \sqrt{Spd} \propto Sa\sqrt{Spd}. \end{aligned} \qquad \text{(Eq. 6-9)}$$

It can be found that the *Sdr* of the rectangular protrusions is proportional to $Sa\sqrt{Spd}$.

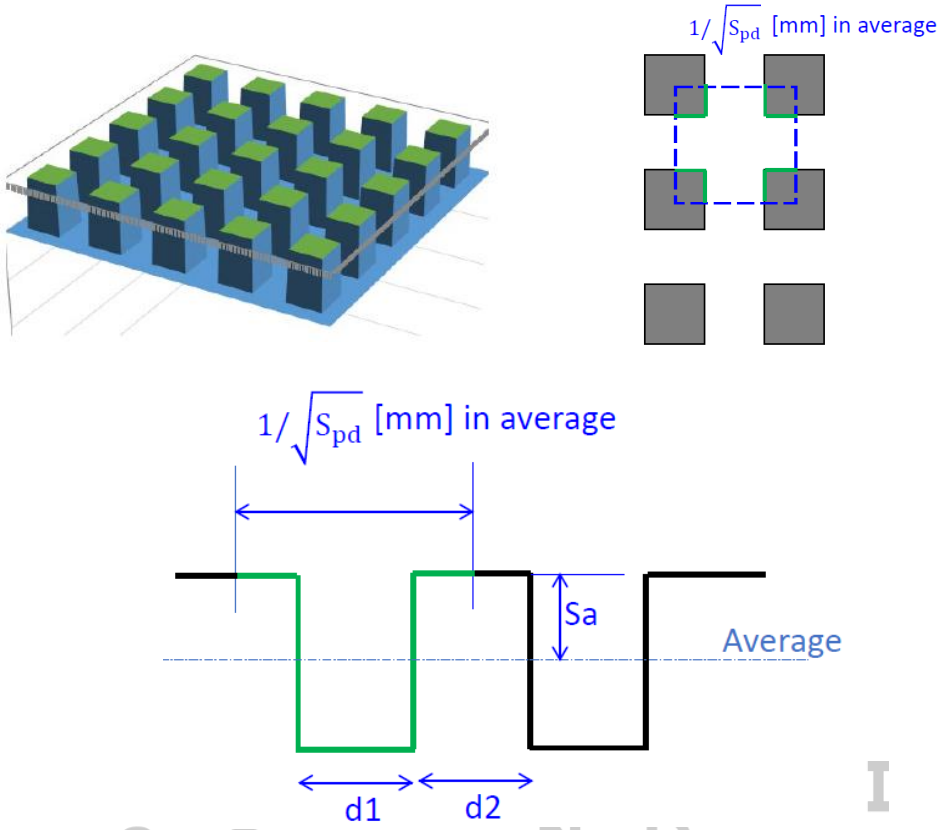

Figure 6-9: Schematic of rectangular protrusions and the parameters used to derive the relationship between *Sdr* and $Sa\sqrt{Spd}$

Figure 6-10 shows the case for triangular protrusions. Similar to before, we assume that in the simplest case ($d_1 = d_2$), the *Sdr* can be expressed as

$$
\begin{aligned}
Sdr &= \frac{Actual\ surface\ area - A}{A} \\
&= \frac{\left\{\left(\frac{1}{2}\frac{1}{\sqrt{Spd}}\sqrt{{d_1}^2 + (4Sa)^2} \times \frac{1}{2} \times 8\right) \times Spd \times A - A\right\}}{A} \\
&= \sqrt{\left(\frac{1}{2\sqrt{Spd}}\right)^2 + (4Sa)^2} \times 2\sqrt{Spd} - 1 \\
&= \sqrt{1 + \left(8Sa\sqrt{Spd}\right)^2} - 1. \qquad \text{(Eq. 6-10)}
\end{aligned}
$$

If $8Sa\sqrt{Spd} \gg 1$, then $Sdr \approx 8Sa\sqrt{Spd} \propto Sa\sqrt{Spd}$. If not, the dependence is complex. In any case, a larger *Sdr* means a larger $Sa\sqrt{Spd}$ and vice versa.

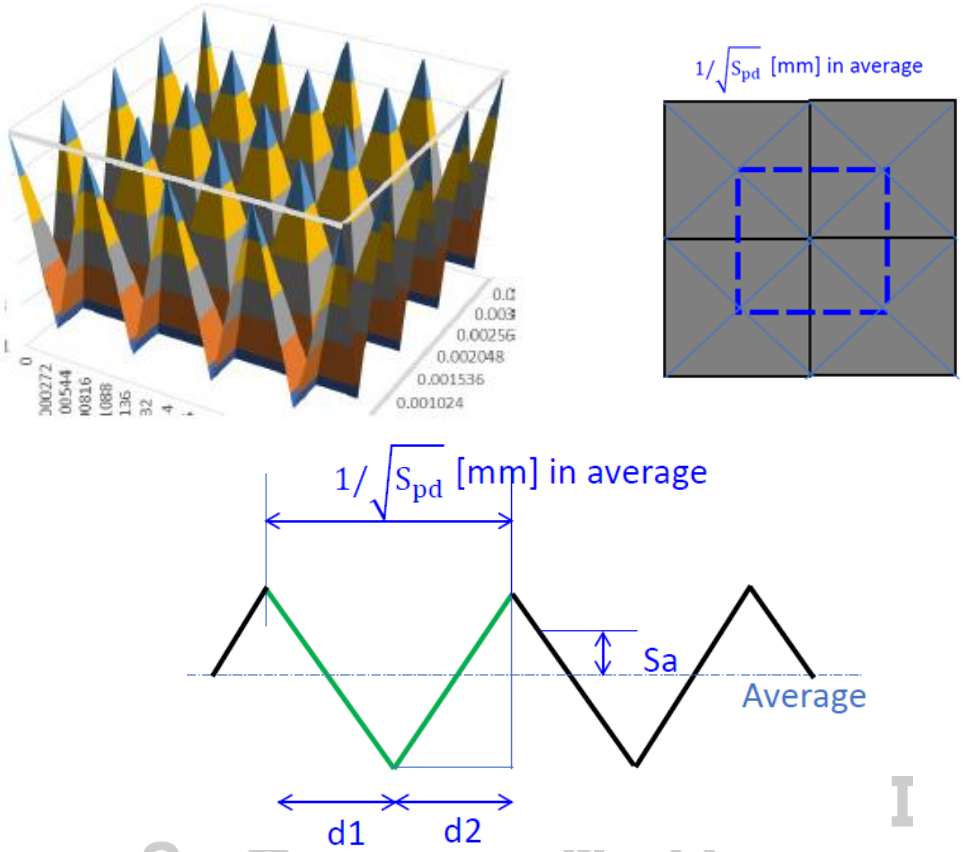

Figure 6-10: Schematic of triangular protrusions and the parameters used to derive the relationship between *Sdr* and $Sa\sqrt{Spd}$

For the case of trapezoidal protrusions, the structure can be viewed as a combination of rectangular and triangular protrusions. Therefore, the *Sdr* can be expressed as a combination of Eqs. (6-9) and (6-10):

$$Sdr = x\{4Sa\sqrt{Spd}\} + (1-x)\left\{\sqrt{1+\left(8Sa\sqrt{Spd}\right)^2} - 1\right\}, 0 \le x \le 1. \quad \text{(Eq. 6-11)}$$

Here, x is the ratio of rectangular and triangular grooves (x = 1 denotes a rectangular groove).

Figure 6-11 shows the relationship between *Sdr* and $Sa\sqrt{Spd}$, according to Eqs. (6-9)–(6-11). It can be observed that, with the exception of the low *Sdr* region, *Sdr* and $Sa\sqrt{Spd}$ were almost linearly related, and the surfaces of different patterns exhibited different proportional coefficients. Therefore, $Sa\sqrt{Spd}$ can be applied as an alternative parameter for *Sdr*.

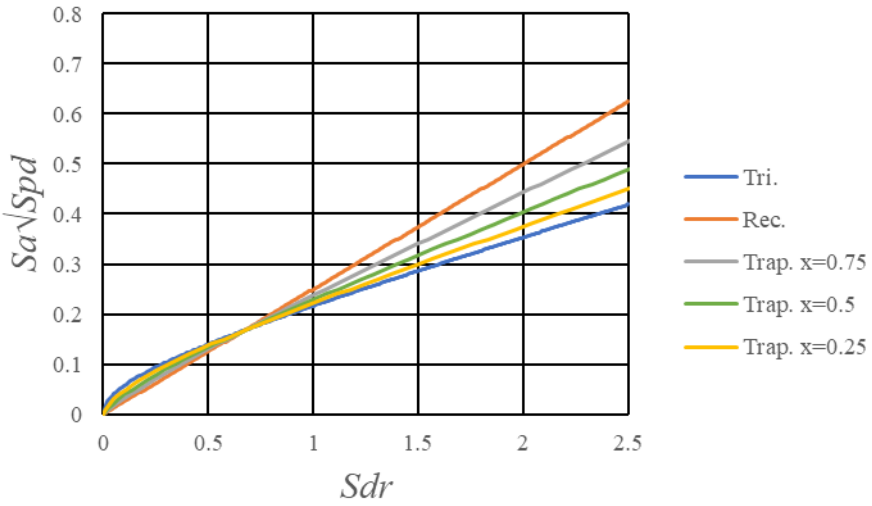

Figure 6-11: *Sdr* as a function of $Sa\sqrt{Spd}$, according to Eqs. (6-9)–(6-11)

SOKENDAI

Chapter 7

Conclusions and Future Work

7.1 Conclusions

This study focused on copper T.S. coatings as a candidate countermeasure for suppressing the ECE in future accelerators. The T.S. coating was comprehensively studied, improved, and evaluated for accelerator applications. Finally, a T.S.-coated aluminum beam pipe was fabricated and installed in SuperKEKB LER, to test its ability to reduce ECs.

SOKENDAI

The T.S. coating had a low SEY (i.e., its δ_{max} could be as low as ~0.7), and its E_{max} exceeded that of a flat copper surface. The surface temperature during spraying had little effect upon δ_{max} but influenced E_{max}. The average electron energy in the accelerator was generally of the order of several hundreds of eVs; hence, a T.S. coating with a lower surface temperature during spraying (~100 ℃) is beneficial for reducing the EC, for which the E_{max} typically exceeds 2000 eV.

The outgassing rate and adhesive strength of the T.S. coating were acceptable. However, the amount of dust and impedance were considerable. If these coatings are widely used in high-energy accelerators, heat load and beam instability issues may arise.

The electron density in the T.S.-coated beam pipe installed in SuperKEKB LER was comparable to those of TiN and TiN groove beam pipes, even when an uncoated aluminum screen was used.

To conclude, our comprehensive evaluation of the T.S. coating indicates that the T.S. coating can be considered a candidate technology for reducing the ECE; however, room for improvement remains. This study offers new and useful information for

researchers seeking to develop low-SEY coatings for beam pipes.

7.2 Summary of Advanced Study

The surface compositions of the T.S. coatings formed under various spray conditions were similar after conditioning (i.e., primarily Cu_2O); thus, the surface structure has a critical influence upon the SEY properties. For surfaces where *Sdr* can be accurately measured, both the simulation and measurement results indicate that δ_{max} is inversely proportional to *Sdr*. However, it is difficult to accurately measure the *Sdr* of a small-scale surface (like that of the T.S. coating) using existing microscopy techniques. If the measurement method for *Sdr* can be improved, then the *Sdr* measured for a T.S. coating can be used to predict its δ_{max}.

It was observed that the electron densities in all beam pipes increased roughly in proportion with the bunch number (n_b) under a fixed linear current density (I_d), especially in the T.S.-coated and TiN groove beam pipes. Simulation results suggest that the inner wall of these two beam pipes had lower δ_{max} values. The measurement results for the electron densities in the presence of a vertical magnetic field B_y also indicate that their δ_{max} values were lower than that of TiN. However, the measured values in these two beam pipes were slightly higher than that in the TiN beam pipe. This may be attributable to the differences in the monitors' characteristics or locations, which reflects the limitations of the currently used monitors at low electron densities.

SOKENDAI

7.3 Future Work

1. The first improvement target is thermal spraying of the uncoated aluminum mesh screen.
2. As mentioned in Section 5.1, the thermal spray samples at the edge of the beam pipe were prone to exhibit different E_{max} or δ_{max} values from other samples in the same group. Thus, the scanning angle of the robotic arm that controlled the spray gun still has room for improvement.
3. Furthermore, research and development into methods of easily applying the T.S. coating to accelerator beam pipes (without cutting) is required for mass production.
4. In terms of reducing the T.S. coating's resistance, we recommend reducing the oxide layer and coating thickness as feasible options. On the other hand, it is also important to monitor the temperature of the existing T.S.-coated beam pipe.
5. To clarify the relationship between the SEY properties and surface roughness, we

require other methods (besides microscopy) for evaluating roughness, such as the application of reflectivity.

6. The effects of high-E_{max} SEY profiles upon electron cloud formation should be further investigated.
7. The differences between monitors should be verified by varying the positions of the monitors or beam pipes.
8. Furthermore, the development of a new electron monitor should be considered. A higher sensitivity and time resolution for EC measurements will benefit our understanding of EC formation.

SOKENDAI

8. References

[1] Y. Ohnishi *et al.*, “Accelerator design at SuperKEKB”, *Prog. Theor. Exp. Phys.*, vol. 2013, p. 03A011, Mar. 2013.

[2] G. Rumolo and G. Iadarola, “Electron cloud”, in *Proc. CAS-CERN Accelerator School: Intensity Limitations in Particle Beams*, Geneva, Switzerland, Nov. 2-11, 2015, pp. 411-430.

[3] F. Zimmermann, H. Fukuma, and K. Ohmi, “More electron cloud studies for KEKB: Long-term evolution, solenoid patterns, and fast blowup”, CERN Report No. CERN-SL-Note-2000-061 AP, Dec. 2000.

[4] H. Fukuma *et al*., “Observation of vertical beam blow-up in KEKB low energy ring”, in *Proc. EPAC2000*, Vienna, Austria, Jun. 2000, pp. 1122-1124.

[5] Y. Suetsugu *et al*., “Mitigating the electron cloud effect in the SuperKEKB positron ring”, *Phys. Rev. Accel. Beams*, vol. 22, p. 023201, Feb. 2019.

[6] F. Zimmermann, “Electron Cloud Effects in accelerators”, in *Proc. ECLOUD’18*, La Biodola, Isola d'Elba, Italy, Jun. 2018, pp. 1-12.

[7] J. A. Crittenden *et al.*, “Investigation into electron cloud effects in the International Linear Collider positron damping ring”, in *Proc. IPAC’12*, New Orleans, USA, May. 2012, paper TUPPR063, pp. 1963-1965.

[8] W. Fischer *et al*., “Electron cloud observations and cures in the Relativistic Heavy Ion Collider”, *Phys. Rev. ST Accel. Beams*, vol. 11, p. 041002, Apr. 2008.

[9] A. Drago *et al*., “Mitigation and control of instabilities in DAFNE positron ring”, *in Proc. BIW'2012*, Newport News, VA, Apr. 2012, paper TUPG001.

[10] Y. Suetsugu *et al*., “Design and construction of the SuperKEKB vacuum system”, *J. Vac. Sci. Technol. A*, vol. 307, p. 301602, Mar. 2012.

[11] Y. Suetsugu *et al*., “Beam tests of a clearing electrode for electron cloud mitigation at KEKB positron ring”, in *Proc. IPAC’10*, Kyoto, Japan, May. 23-28, 2010, paper WEOAMH01, pp. 2369-2371.

[12] K. Oide, Observations and cures of electron-cloud effects at the KEKB low energy ring, in Proceedings of the Chamonix XI, Chamonix, Switzerland, 2001, CERN Report No. CERN-SL-2001-003, 2001.

[13] H. Fukuma *et al.*, “Status of solenoid system to suppress the electron cloud effects at the KEKB”, in *AIP Conf. Proc. 642*, Batavia, IL, USA, Apr. 2002, pp. 357-359.

[14] Y. Cai, M. Pivi, and M. A. Furman, “Buildup of electron cloud in the PEP-II particle accelerator in the presence of a solenoid field and with different bunch pattern”, *Phys. Rev. ST Accel. Beams*, vol. 7, p. 024402, Sep. 2004.

[15] Y. Funakoshi *et al.*, “Recent progress at KEKB”, in *Proc. EPAC’06*, Edinburgh, Scotland, Jun. 2006, pp. 610-612.

[16] H. Fukuma *et al.*, “The effect of the solenoid field in quadrupole magnets on the

SOKENDAI

electron cloud instability in the KEKB LER", in *Proc. EPAC'06*, Edinburgh, Scotland, Jun. 2006, pp. 2901-2902.

[17] R. Cimino *et al.*, "Electron energy dependence of scrubbing efficiency to mitigate e-cloud formation in accelerators", in *EPAC'08*, Genoa, Italy, Jun. 2008, paper TUPP027, pp.1592-1594.

[18] K. Ohmi and M. Furman, "Beam Dynamics Newsletter No. 33", ICFA, Apr. 2004.

[19] Proceedings ECLOUD'02, Geneva, 15-18 April, 2002, Published As CERN Yellow Report CERN-2002-001; Proceedings of the 31st ICFA Advanced Beam Dynamics Workshop on Electron-Cloud Effects ECLOUD'04, Napa, CA, 2004, edited by M. Furman, S. Henderson, F. Zimmermann, CERN Yellow Report No CERN-2005-001

[20] H. Seiler," Secondary electron emission in the scanning electron microscope", *J. Appl. Phys.*, vol. 54, no. 11, p. R1, Jul. 1983.

[21] V. Baglin *et al.*, "The secondary electron yield of technical materials and its variation with surface treatments", in *Proc. EPAC2000*, Vienna, Austria, Jun. 2000, pp. 217-221.

[22] K.N. Leung, *et al.*, "TiN coating of accelerator beamline chambers", in *Proc. PAC'97*, Vancouver, Canada, May 1997, pp. 3737-3739.

[23] A. Tatami *et al.*, "Graphite thin films for accelerator applications", in *Proc. PASJ'17*, Sapporo, Japan, Aug. 2017, paper THOL04, pp. 159-161.

[24] G. Dollinger *et al.*, "New plant for fabricating carbon stripper foils by laser plasma ablation deposition", *Nucl. Instr. Meth. Phys. Res.*, sec. A 328, pp. 168-172, 1993.

[25] P. Costa Pinto *et al.*, "Thin film coatings for suppressing electron multipacting in particle accelerators", in *Proc. IPAC'11*, New York, USA, Sep. 2011, paper THOBS6, pp. 2096-2098.

[26] Y. Suetsugu *et al.*, "Experimental studies on grooved surfaces to suppress secondary electron emission", in *Proc. IPAC'10*, Kyoto, Japan, May 2010, paper TUPD043, pp. 2021-2023.

[27] I. Bojko *et al.*, "Influence of air exposures and thermal treatments on the secondary electron yield of copper", *J. Vac. Sci. Technol*, vol. 18, p. 972, 2000.

[28] R. Valizadeh *et al.*, "Low secondary electron yield engineered surface for electron cloud mitigation", *Appl. Phys. Lett.*, vol. 105, p. 231605, Nov. 2014.

[29] R. Valizadeh *et al.*," Low secondary electron yield of laser treated surfaces of copper, aluminium and stainless steel", in *Proc. IPAC'16*, Busan, Korea, May 2016 TUOCB02, pp.1089-1092.

[30] L. Pawlowski, *The Science and Engineering of Thermal Spray Coatings*, 2nd ed., Chichester, England: Wiley, 2008.

[31] M. Yao, "Study on secondary electron yield from thermal-sprayed metal surfaces", Master thesis, Accel. Sci. Dept., SOKENDAI, Tsukuba, Japan, 2019.

SOKENDAI

[32] R. G. Lye and A. J. Dekker, “Theory of Secondary Emission,” *Phys. Rev.*, vol. 107, pp. 977-981, May 1957.

[33] S. A. Schwarz, “Application of a semi-empirical sputtering model to secondary electron emission”, *J. Appl. Phys.*, vol. 68, pp. 2382-2391, May 1990.

[34] J. Rodney and M. Vaugham, “A new formula for secondary Emission Yield”, *IEEE Trans. Elec. Dev.*, vol. 36, no. 9, pp. 1963-1967, Sep. 1989.

[35] M. A. Furman and M. T. F. Pivi, “Probabilistic model for the simulation of secondary electron emission,” *Phys. Rev. ST Accel. Beams*, vol. 5, p.124404, Dec. 2002.

[36] H. Bruining, Physics and Applications of Secondary Electron Emission (Pergamon Press, McGraw-Hill Book Co., New York, 1954).

[37] P. A. Redhead, J. P. Hobson, and E.V. Kornelsen, The Physical Basis of Ultrahigh Vacuum (Chapman and Hall, London, 1968), Chap. 4 (reprinted by the AIP in 1993 as part of the American Vacuum Society Classics series).

[38] Keyence, https://www.keyence.eu/products/microscope/laser-microscope/vk-x100_x200/models/vk-x1100/

[39] Keyence, https://www.keyence.com/ss/products/microscope/roughness/surface/parameters.jsp

[40] P.L.J Gunter, O.L.J Gijzeman, and J.W Niemantsverdriet, “Surface roughness effects in quantitative XPS: magic angle for determining overlayer thickness”, *Applied Surface Science*, vol. 115, pp. 342-346, Aug. 1997.

[41] K. Kanazawa *et al.*, “Measurement of the electron cloud density around the beam,” in *Proc. PAC’05*, Knoxville, USA, May 16–20, 2005, pp. 1054–1056

[42] Zimmermann, “Electron Cloud at the KEKB Low-Energy Ring: Simulations of Central Cloud Density, Bunch Filling Patterns, Magnetic Fields, and Lost Electrons”, CERN Report No. CERN-SL-Note-2000-017 AP, Jun. 2000.

[43] Y. Suetsugu *et al.,* “Electron Cloud Effects in the SuperKEKB positron ring”, *J. PASJ*, vol. 16, pp. 175-184, Oct. 2019.

[44] K. Terada, T. Okano, and Y. Tuzi, “Conductance modulation method for the measurement of the pumping speed and outgassing rate of pumps in ultrahigh vacuum”, *J. Vac. Sci. Technol. A*, vol. 7, pp. 2397-2402, Jan. 1989.

[45] Paul J. Petersan and Steven M. Anlage, “Measurement of resonant frequency and quality factor of microwave resonators: Comparison of methods”, *J. Appl. Phys.*, vol. 84, p. 3392, Sep. 1998.

[46] A. Wu Chao, “Operation of Superconducting Linacs”, *Handbook of Accelerator Physics and Engineering*, Toh Tuck Link, Singapore: World Scientific, 2013, p.

SOKENDAI

326.
[47] Harold Pender and William A. Del Mar, “Standards of the A.I.E.E.” in *Handbook for electrical engineers; a reference book for practicing engineers and students*, NY, USA: Wiley, 1922, p. 2094.
[48] Raymond A. Serway, *Principles of Physics*, Fort Worth, Texas; London: Saunders College Pub., 1998, p. 602.
[49] CST Particle Studio, https://www.cst.com
[50] H. Padamsee, J. Knobloch and T. Hayes, *RF Superconductivity for Accelerators*, NY, USA: Wiley, 1998, pp. 45, 78-79.
[51] JIS H 8402: Test Methods of Tensile Adhesive Strength for Thermal-Sprayed Coatings
[52] G. Honjo, “Electron diffraction Studies on oxide films formed on metals and alloys Part 1. Oxidation of pure copper”, *J. Phys. Soc. Jpn.*, vol. 4, pp. 330-333, Apr. 1949.
[53] K. Shibata *et al*, “TiN coating and pre-baking of beam ducts for SuperKEKB”, in *Proc. PASJ2013*, Japan, Aug. 3-5, 2013, paper SUP097, pp. 1168-1172.
[54] Andrew Siao Ming Ang1 and Christopher C. Berndt, “A review of testing methods for thermal spray coatings”, *Int. Mater. Rev.*, vol 59, pp. 179-223, 2014
[55] J.G. Odhiambo *et al.*, “Porosity and Its Significance in Plasma-Sprayed Coatings”, *Coatings*, vol. 9, p. 460,2019.
[56] https://www.thermofisher.com/jp/ja/home/materials-science/learning-center/periodic-table.html
[57] I. Platzman *et al.*, “Oxidation of Polycrystalline Copper Thin Films at Ambient Conditions”, *J. Phys. Chem. C*, vol. 112, pp. 1101-1108, 2008.
[58] G. Iadarola and G. Rumolo, “PyECLOUD and build-up simulations at CERN”, in *Proc. ECLOUD’12*, La Biodola, Isola d'Elba, Italy, Jun. 2012, pp. 189-194.
[59] Y. Suetsugu *et al*., “Recent studies on photoelectron and secondary electron yields of TiN and NEG coatings using the KEKB positron ring”, *Nucl. Instrum. Methods. Phys. Res. A*, vol. 578, pp. 470-479, Jun. 2007.
[60] Y. Koyatsu, H. Miki and F. Watanabe, “Measurements of outgassing rate from copper and copper alloy chambers”, *Vacuum*, vol. 47, pp. 709-711, Jun. 1996.
[61] T. Abe *et al.*, “Outgassing rate of highly pure copper electroplating applied to RF cavities”, in *Proc. EPAC’06*, Edinburgh, Scotland, Jun. 2006, pp. 1307-1309.
[62] M. Ohring, *Engineering Materials Science*, New York: Academic Press, 1995.
[63] G. Elert, Resistivity of steel, The Physics Factbook, http://hypertextbook.com/facts
[64] Y. Sato *et al*., “Material and surface processing in J-PARC vacuum system”, *Vacuum*, vol. 86, pp. 817-821, Feb. 2012.
[65] R. Valizadeh *et al.*, “Reduction of secondary electron yield for E-cloud mitigation

by laser ablation surface engineering", *Appl. Surf. Sci.*, vol. 404, pp. 370-379, May 2017.

[66] N. Nakamura, "Resistive-wall impedance effects for the new KEK Light Source", in *Proc. IPAC'17*, Copenhagen, Denmark, May 2017, paper WEPIK071, pp. 3095-3097.

[67] Y. Suetsugu, "High-Intensity Synchrotron Radiation Effects", Published by CERN in the Proceedings of the Joint International Accelerator School: Beam Loss and Accelerator Protection, Newport Beach, US, 5–14 November 2014, edited by R. Schmidt, CERN-2016-002 (CERN, Geneva, 2016)